ROTATIONAL AND VIBRATIONAL ENERGY TRANSFER IN METHANE

by

BERNARD RYAN FOY

A.B. Chemistry, Washington University (1982)

Submitted to the Department of Chemistry
in Partial Fulfillment of the Requirements for
the Degree of

DOCTOR OF PHILOSOPHY IN CHEMISTRY

at the

Massachusetts Institute of Technology

February 1988

© Massachusetts Institute of Technology   1988

Signature of Author _____ (Signature redacted _____
Department of Chemistry
November 23, 1987

Certified by _____ Signature redacted _____
Jeffrey I. Steinfeld
Thesis Supervisor

Accepted by _____ Signature redacted _____
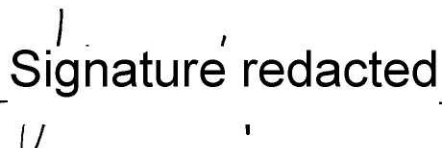Glenn A. Berchtold
Chairman, Departmental Committee on Graduate Students
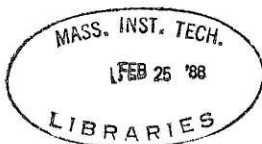
This doctoral thesis has been examined by a Committee of the Department of Chemistry as follows:

Professor Keith A. Nelson _____ Signature redacted _____

<div align="right">Chairman</div>

Professor Jeffrey I. Steinfeld Signature redacted _____

<div align="right">Thesis Supervisor</div>

Professor John S. Waugh _____ Signature redacted _____

2

ROTATIONAL AND VIBRATIONAL ENERGY TRANSFER IN METHANE

by

Bernard R. Foy

Submitted to the Department of Chemistry on November 23, 1987
in partial fulfillment of the requirements for the degree of
Doctor of Philosophy in Chemistry

Abstract

We describe state-resolved studies of rotational and vibrational energy transfer in the isotopically substituted methane molecule, $^{13}CD_4$. An infrared double resonance laser spectroscopic technique is used to prepare molecules in a selected rovibrational state, with the quantum numbers v, J, and C^n completely specified. Measurements of both the rate of total depopulation of the level by collisions and the rates of transfer into specific final rotational states (v, J, C^n) are measured by time-resolved transient absorption. The depopulation rates due to collisions between methane and the rare gases are on the order of the Lennard-Jones collision frequencies. Self-relaxation is slightly more efficient than the Lennard-Jones estimate. The rather small relaxation rates are characteristic of a short-range potential, or "strong-collision" regime, expected for a molecule without a dipole moment.

The state-to-state energy transfer measurements represent the most detailed studies of collisional behavior in spherical-top molecules yet performed. In self-collisions, we observe a dramatic selectivity of rotational energy transfer pathways with respect to the fine-structure rotational states C^n. Relaxation occurs through a surprisingly small subset of the energetically accessible pathways. Also suggested is a preference for population transfer to occur within the initial vibrational angular momentum sublevel of the ν_4 (F_2) vibrational state, which has three sublevels in consequence of Coriolis interaction. This preference can be formulated as a propensity for $\Delta(R - J) = 0$ transitions. The precise origins of these selectivities remain mysterious, but some potential causes are discussed. We deduce that large changes of J ($\Delta J \sim 5$) can occur in single collisions between methane molecules, based on a simple kinetic model of the data. This is also characteristic of short-range collisions in which it is likely that no single multipolar interaction dominates.

Collisional relaxation between the ν_4 and ν_2 bending vibrations is measured by direct absorption and proceeds more slowly than rotational relaxation, but as fast as transfer among the closely grouped stretching and bend-overtone levels, measured previously for CH_4. No evidence for rotationally specific V-V transfer is found. We discuss an exhaustive spectroscopic analysis of $^{13}CD_4$ that provides unambiguous spectral assignments for use in detecting vibrationally excited molecules ($v_4 = 1$) in specific rotational states.

Thesis Supervisor: Jeffrey I. Steinfeld
Title: Professor

Acknowledgements

The list of those responsible for my scientific upbringing is replete with colorful characters. Foremost among them is Jeff Steinfeld, to whom I am indebted for five years of patience, wisdom, guidance, Friday afternoon beer, and lobsters. Jeff is most adept at establishing a comfortable atmosphere in which to work. But I'll never forgive him for sending me off to France for a month. Gérard Pierre is responsible for the next 100 pages to the same extent as am I. Were it not for his interest in our bizarre choice of a molecule, state-to-state energy transfer in methane would still be a subject of the future. I thank him also for introductions to Kir and raclette, a visit to Château-Neuf, and Fig. 2-6. The second Frenchman whose influence can be perceived throughout these pages is Guy Millot, whose few months at M.I.T. did much to propel me toward my defense, and who elevated my understanding (from nothing to something) of those strange creatures that seem so foreign to this planet, the spherical-top molecules. Dr. Ramachandra Dasari and the G.R. Harrison Spectroscopy Laboratory loaned some essential pieces of equipment. The quotation in the Preface was taken from *Physical Chemistry* by W.J. Moore.

I am most fortunate to have started at M.I.T. with classmates of upstanding character and beer-drinking capacity. Steve Joyce and Jay Thoman have been invaluable not only in the latter respect but in experimental assistance. Steve, whose keen sense of humor could extinguish a thousand cigarettes, is hereby thanked for slaving over shop drawings for Sophie (the TEA laser who figures prominently in Chapter 4) for many thankless hours. Jay kept us busy with Christmas parties and Red Sox games, and I can't thank him enough for arranging for my first glimpse of a short-eared owl. Dan Raleigh's wit would benefit from a slightly more sarcastic edge. Thanks for the stove, Dan. Leah Williams *née* Ruby and Marianimal McGonigal also lent support by staying here as long as I did. I thank Chippa Gray and Porcupine Warner for softball, football, and for initiating the Rite of Darts.

I am grateful to Leo Laux for teaching me how to do DILDoR and to Dave Harradine for teaching me how not to do it. To Joe Simonson I hereby bequeath my three hundred old issues of *The New Yorker*, if he hasn't already read them. They and Eric Schweitzer, Neal Shinn, Bobbi Roop, and everyone else are thanked for restful camping trips, colored invariably by Benjamin Franklin's favorite bird. Spike B. Lee is thanked just for being Spike, and for teaching us all that highly refined art of profanity. 'Ead Gladstone supplied the wrenches when needed, and makes the best damn chiken wings that any Coloradan ever has. Irwin Winkler is capable of non-stop entertainment, which brightened our Friday afternoons for two years; his replacement, Mark "Hah

Lips" Phillips, encouraged us to explore new linguistic horizons. Pat Vaccaro contributed a tremendous amount of computer code to this work. I just wish we could figure out what time zone he seems to be working in. Bob DiGiacomo was always prepared for conversation, usually while making my next cell.

A number of foreigners contributed to this work, in addition to those already mentioned. Zhao Yao lasted through the difficult period of laser construction, and I wish him well when he finally gets back home. Scott Kable, smoother than James Bond, helped out on the material of Chapter 3, and contributed a lot of good advice. Mark Rainbird kept things lively during the final months, despite his extraordinarily naive political beliefs. Alan Knight, the itinerant Australian responsible for the latter two clowns, was inspirational through many scientific discussions.

I am thankful to John Langan for keeping our lunchtime conversations humorous. I'm happy that we had Xu Xin to raise our consciousness of ethnic diversity. I hope that the next in line for the experiment, Joanne Hetzler, won't curse my name too often upon discovery of the booby traps I have laid. Carol Van Zoeren is ready to take over as the new senior member, may her pen never cease to write. MikeandMarie Hale provided steady support, as did Chuck Cousteau Hamilton and Tex "Bruce" Johnson, who always drank all the coffee. Though my admiration for M.I.T. as an educational institution is not without bounds, I must acknowledge that it is responsible for my meeting Karen, whose spiritual support enabled me to complete this work in a finite period of time.

Finally, I am grateful to the one who got me started ten years ago, who convinced me that chemistry is not so boring after all, and to whom I dedicate this thesis: Mr. T.J. Schaeffer of McQuaid Jesuit High School.

Now forasmuch as the Elements, unless they be altered, cannot constitute mixt bodies; nor can they be altered unless they act and suffer one from another; nor can they act and suffer unless they touch one another, we must first speak a little concerning contact or mutual touching, Action, passion, and Reaction.

Daniel Sennert (1660)
(Thirteen Books of Natural Philosophy)

Table of Contents

Table of Contents (cont.)

8

List of Figures

List of Tables

Chapter One
Introduction

Chemists and physicists have long been interested in how collisions alter the internal states of atoms and molecules. For a chemist, the interest stems from the relationship between collisions that cause a change in state and collisions with the more serious consequence of a reaction; both are governed by the intermolecular potential energy function, which in general is known only poorly. Part of the motivation for studying molecular energy transfer (which might more aptly be called the study of collision-induced transitions) is the desire for a better knowledge of these potentials. A wide variety of experimental techniques have been devised to study an array of collisional phenomena in pursuit of this goal. Recent decades have brought a shift in emphasis to state-resolved studies because of the detailed nature of the behavior that they reveal, requiring increasingly sophisticated approaches for theoretical interpretation. Early techniques such as ultrasonic absorption and dispersion [HERZ59] were able to discriminate between vibrational and rotational degrees of freedom in collisional relaxation, but further state resolution required the use of narrow-bandwidth spectroscopic techniques. Laser-based techniques, in particular, have enabled us to examine both initial and final states of molecules suffering collisions, for molecules of widely different spectroscopic properties.

The vibrational and rotational relaxation of diatomic molecules has been a particularly fruitful topic of study, due in part to their convenient spectroscopic properties. Perhaps the most famous example is I_2, on which Franck and Wood obtained the first results as early as 1911 [FRAN11]. The work was extended in the 1960s to a high level of detail [STEIN65] and continues to the present day [VANZ87]. The well-studied alkali dimers Na_2 and Li_2 show an intricate pattern of relative probabilities for specific changes of rovibrational state [YARD80]. Recent experiments using elegant Raman techniques have determined the relaxation pathways of HD [CHAN86]. There are countless other examples. The collisional behavior of polyatomic molecules is known in less detail, due mainly to the high density of rotational and vibrational states. This makes it difficult to prepare the molecules selectively in identifiable energy levels and to detect selectively molecules in final states. Collisional relaxation can be very fast, in addition, since the energy level spacings are small; this requires the use of high sensitivity methods at low pressures.

These difficulties can sometimes be overcome by using one of a variety of clever experimental techniques, but each is usually applicable only to a restricted class of molecules.

Techniques also vary widely with regard to the degree of state resolution, and whether one or both of the initial and final states are specified. Since the density of rotational levels is often much higher than the density of vibrational levels, one can choose to study purely vibrational relaxation under conditions in which (it is assumed) rotational equilibration is so fast that the vibrational energy transfer rates are "rotationally averaged." This realization led to the widespread use of infrared fluorescence detection in vibrational energy transfer experiments on polyatomic molecules. Since infrared fluorescence is normally incapable of resolving the rotational structure of vibrational bands, it is well suited to the task. Studies making use of the technique are well documented in Yardley's book [YARD80]. The vibrational relaxation of small polyatomic molecules is now known quite well, at least for molecules with strong infrared transition moments (e.g., CO_2, CH_3F, CH_4).

We can obtain different kinds of information on the intermolecular potential by looking in finer detail at collisional relaxation. Rotational relaxation is one such avenue, a logical choice because it occurs with high probability per collision. The change of the rotational angular momentum of a molecule occurs through the exertion of a torque by the collision partner. This torque arises from the anisotropy of the intermolecular potential, so we expect that rotational relaxation should be a particularly sensitive probe of the degree of the anisotropy. Spectroscopic probes are convenient means of achieving rotational resolution. Visible fluorescence and microwave absorption, for example, have been used extensively to study state-resolved rotational energy transfer. Visible fluorescence is a highly sensitive detection technique and is especially versatile when produced by tunable lasers. But this is limited to the study of molecules that fluoresce with high yield, and whose fluorescence can be excited at convenient wavelengths. Microwave techniques, on the other hand, are applicable to all polar polyatomic molecules; microwave double resonance experiments have been especially valuable in elucidating rotationally specific relaxation pathways of molecules such as NH_3, H_2CO, HCN, and OCS. The drawback of this approach is that it is not applicable to non-polar molecules, including the whole class of spherical tops. Also, in many cases the experiment is not time-resolved, so it is difficult to obtain rate constants for state-specific pathways on absolute terms.

Rotational Energy Transfer in Spherical Tops

There is a paucity of data, both quantitative and qualitative, on rotational energy transfer in the spherical-top molecules (of tetrahedral (T_d) or octahedral (O_h) symmetry). Neither microwave nor laser-induced fluorescence (LIF) techniques are useful in this case, so that one must rely on the infrared region of the spectrum, in which high-resolution tunable lasers have been historically

difficult to come by. It is unfortunate that so little is known about the spherical tops, since these molecules hold the promise of yielding another level of insight into molecular interactions: the short-range anisotropic forces. Experiments on the small polar polyatomic molecules have demonstrated that the long-range dipole-dipole interaction dominates their rotational relaxation behavior, masking the effects of the short-range forces. Rotational relaxation cross sections for polar molecules are normally five to ten times greater than the Lennard-Jones cross sections, the benchmark figures determined from measurements of transport properties. Since the spherical tops (like CH_4 and SF_6) are by symmetry non-polar, we expect their relaxation cross sections to be smaller than for polar molecules of similar mass. Bulk measurements of relaxation rates (e.g., by ultrasonic dispersion) have shown that this is indeed the case. Hence, methane molecules approach quite closely in collisions, obtaining intimate views of each other as they pass. These collisions may manifest a good deal more about the details of the potential surface than the simple anisotropies like dipolar charge distributions in polar molecules.

The limited information about rotational relaxation in spherical tops that is available indicates that there is interesting behavior to be unearthed, provided that one has sufficiently incisive tools with which to search for it. Line-broadening studies reveal that collision-broadening parameters of rovibrational transitions in methane are dependent on the rotational quantum labels J and C^n, the latter being the fine-structure designation (explained in Chapter 2). Methane molecules have three nuclear spin modifications, distinguished in the rovibrational spectrum by symmetry species A, E, and F. Studies show that the collisional linewidths for a given J value are ranked in the order $\Gamma_E < \Gamma_A \leq \Gamma_F$ [FOX84]. Linewidths for distinct transitions within each symmetry category also show variations [BALL86]. We must bear in mind that collision-broadening parameters are related to the sum of state-to-state rate constants for all pathways from the specified state: the technique offers only partial state resolution. The unusual pattern of the line-broadening parameters, however, intimates that there may be an intricate underlying pattern of state-to-state pathways. The goal of the work described in this thesis is to elucidate the intricate pattern by making measurements in which the final states produced by the collision are resolved.

In view of the difficulty or impossibility of using some spectroscopic techniques to study rotational energy transfer, one might attempt to use non-spectroscopic methods. One alternative that has been realized in recent years is state-resolved scattering by crossed molecular beams. Buck and colleagues have accomplished this by scattering a beam of rare-gas atoms off of a beam of methane molecules; time-of-flight analysis of the scattered atoms shows translational energy losses that correspond to collisional excitation of the methane molecule to specific rotational states

[BUCK85]. The initial-state specificity here is accomplished by cooling of the methane molecules in the beam to their lowest rotational states. (The three nuclear spin species relax into different lowest-energy states with $J = 0, 1$, and 2). The beauty of the technique is that the data are affected only by single-collision events, and that the small number of excitation pathways that are probable allows comparison with very detailed theoretical modelling. The difficulty with the beam-scattering measurements is the rather low resolution of rotational excitation energies provided by the time-of-flight analysis. Scattered peaks corresponding to different values of $(J_f - J_i)$ are just barely resolved, and in fact, the results must be deconvoluted to obtain the state-specific data. The experiments are performed at collision energies much higher than encountered in thermal velocity distributions, so the results may be most sensitive to the repulsive part of the potential. In addition, the data are collected in the form of differential scattering intensities rather than the total cross sections available from static-cell experiments.

Infrared Double Resonance (IRDR)

The experimental technique that we used to perform the state-to-state rovibrational energy transfer experiments described in this thesis is illustrated in Fig. 1-1. A pulsed laser populates a specific rotational level in an excited vibrational state. The collisional redistribution of that population is monitored as a function of time by absorption of a c.w. probe laser that can be tuned to examine selected neighboring rotational and vibrational levels. This technique has been used previously in our laboratory to study rotational relaxation in CDF_3 [HARR84] and SF_6 [DUBS82]. Other laboratories have used similar IRDR methods to study collisional relaxation in molecules such as NH_3 [DANA87, VEEK85], HF [HAUG84], and CO_2 [KREU87].

IRDR experiments on SF_6 that used a continuously tunable probe laser offered perhaps the first view of state-to-state rotational relaxation in a spherical-top molecule [DUBS82]. Similar measurements were made by using stimulated Raman gain as a detection method [ESH82]. These experiments, however, encountered extreme spectral congestion that made the observation of rotational relaxation very difficult. The density of rotational levels in SF_6 is very high, owing to its small rotational constant, $B = 0.09$ cm^{-1}. This makes state-specific excitation very difficult and allows rotational relaxation to be very fast. Consequently, the work allowed only qualitative conclusions about the relaxation pathways.

14
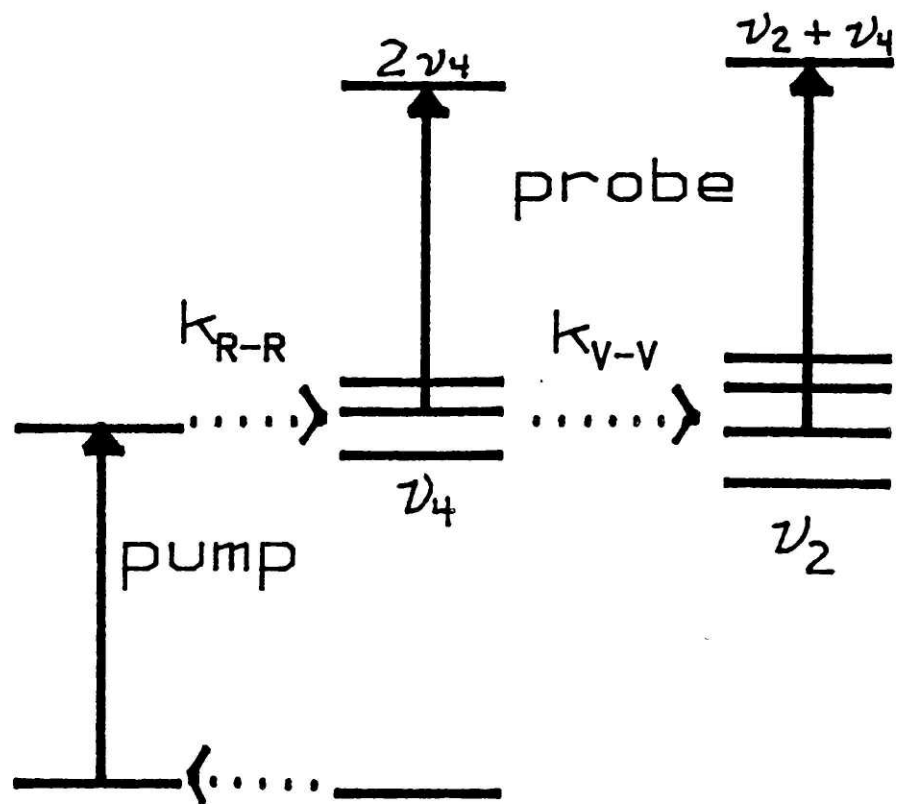
Figure 1-1: Infrared Double Resonance on Methane

The subject of this work. the methane molecule. possesses more desirable qualities peculiar to the lighter spherical tops. The well-separated spectral features enable us to pump and probe single fine-structure rotational levels. Thus, we can examine state-to-state relaxation pathways at a higher level of detail than has been attained before. Since we use a CO_2 laser as the pulsed pump source, our choice of molecular transitions to be pumped is constrained to those in close coincidence with the discrete CO_2 laser lines, which fall in the region 930-1090 cm^{-1}. This rules out the use of CH_4, since its lowest vibrational frequencies are higher than this, but we found a few coincidences for the isotopically substituted species $^{13}CD_4$. Since it is not a major atmospheric constituent, $^{13}CD_4$ has happily found use as a tracer for wind currents in the upper atmosphere, where it undoubtedly undergoes rotational relaxation [COW76].

Relaxation Pathways in Methane

Symmetric-top and spherical-top molecules can have vibrational normal modes that are twofold or threefold degenerate. As Herzberg explains in detail [HERZ45], some of these vibrations carry vibrational angular momentum that arises from Coriolis coupling among the degenerate set of modes when the molecule rotates. The rotational levels of these vibrations are characterized by different states of coupling with the vibrational angular momentum. Hence, rotational energy transfer among these levels can involve changes of both the rotational and vibrational angular momenta. (Technically, as Herzberg explains, we say that states of a given total angular momentum J differ in the magnitude of the "purely rotational" angular momentum vector R, in the spherical top.) In the IRDR experiment on methane, we excite molecules to the ν_4 vibration, which does carry vibrational angular momentum, as we will discuss at length in Chapter 2. Thus, we can study *the role of vibrational angular momentum in rotational energy transfer*, a subject on which there is little experimental data.

In addition to purely rotational (R-R) energy transfer, there is a vibrational energy transfer channel that we expect to be important as well. This is transfer from the initial vibrational state ν_4 to the neighboring bending level ν_2, as shown in Fig. 1-1. Here, we monitor the populations of specific rotational levels of ν_2, just as in the case of rotational relaxation within ν_4. Previous attempts to measure the $\nu_4 \to \nu_2$ energy transfer rate in $^{12}CH_4$ and $^{12}CD_4$ have used methods that are not rotationally specific. The advantages of monitoring the V-V relaxation as a *rovibrational* process, by specifying initial and final rotational quantum numbers as well as the vibrational labels, has become clear since a series of experiments by Orr and colleagues [ORR84]. They studied the collisional transfer $\nu_6 \to \nu_4$ in D_2CO by an infrared-ultraviolet double resonance technique, and

found that the V-V transfer proceeds through rotational pathways that are remarkably selective. The results were interpreted in terms of Coriolis coupling between the vibrational modes, indicating that under certain conditions, intramolecular Coriolis coupling enhances the V-V rate for certain channels of selected J and K_a. Such behavior is obscured when the rotational states are not resolved by the experiment.

Previous Scattering Data on Methane

As methane is something of a prototypical polyatomic molecule, it has been the subject of numerous investigations of collisional behavior. Projectiles of every sort have been directed at it, including electrons, neutrons and positrons, in addition to a long list of atomic and molecular species. (Methane has itself assumed the role of the projectile, hurled in the direction of a nickel surface in ultra-high vacuum [LEE87].) Virtually all of the methods available for measuring the bulk relaxation phenomena have been applied to methane: ultrasonic absorption [KIST74], photoacoustic measurements [AVRA81,PERR82,KARB85], nuclear spin relaxation [JOHN61,BLOOM67], thermal lensing [SIEB74], light scattering [MEIN86], and others. Differential scattering in molecular beam experiments has been measured for methane in collision with itself [BOUG85,REID85] and the rare gases [BUCK85]. Collision-induced absorption spectra are known for methane [BORY87]. All of these measurements can be combined to yield valuable data on the interaction potential, especially on the *isotropic* part; they may not be sensitive to the precise contribution of the anisotropic part of the potential.

It would appear, then, that methane is an excellent candidate for state-resolved measurements of rotationally inelastic collision probabilities. The information gained from these studies would complement the information provided by the bulk relaxation measurements in its sensitivity to anisotropic interactions. But perhaps the greatest virtue of experiments in which the final states are resolved is their abilitiy to detect selectivities for particular changes of quantum state [OKA73]. The selectivities can often be expressed in the compact form of propensity rules for changes in various quantum numbers. Thus, we can learn about some of the fundamental details of the collision without first having to perform a complex scattering calculation, during which we may lose some of the physical insight into the interaction. On the other hand, propensity rules for collisional energy transfer that have been seen experimentally provide a simple way to test the detailed theories. The interplay between experiment and theory has been and will continue to be a valuable means of illuminating the dynamics of the collision.

Chapter Two
The Rovibrational Energy Levels of $^{13}CD_4$

"...the nature of the spherical top hamiltonian remains obscure to the majority of spectroscopists."

—A.G. Robiette, 1976

2.1 Introduction

In this chapter, we shall outline the spectroscopic treatment of the rotation-vibration energy levels that are important for the energy transfer experiments discussed in the succeeding chapters. A spectroscopic analysis of the energy levels is important for two reasons. The obvious reason is that it allows us to identify spectral features so that we can monitor the populations of single energy levels with well-defined quantum numbers. But perhaps more importantly, it enables us to understand the precise nature of the rotation-vibration states, and therefore gives us a tremendous amount of insight into the collisional dynamics of the molecule.

The simple identification of spectral features is of course requisite for any study of state-resolved collisional energy transfer, and illustrates the well-known lesson that spectroscopy must precede a meaningful study of collisional energy transfer. In the case of methane (and its isotopic variants), we are fortunate that an exhaustive, unambiguous, and accurate spectroscopic analysis is made possible by the structural simplicity of the molecule and by the ability to separate spectral features with modern laser and Fourier transform techniques. We are free to fix the probe laser to any spectral feature and measure the population evolution of a level with specific rotational quantum numbers. There are no strong features in the spectrum that cannot be identified, so every important pathway for transfer can in principle be identified.

As we shall see, collisional energy transfer in methane is highly selective toward rovibrational states, and in order to understand the basis of this selectivity, we will be forced to rely on the spectroscopic description of these states. Apart from being certain of the exact quantum numbers and quantum labels of the states, we can make use of the approximate quantum numbers as well, since they provide useful descriptions of the states even if not strictly correct. To be more specific, the spectroscopic analysis provides us with quantum numbers J and C^n for levels of the $^{13}CD_4$ dyad, and the approximate quantum numbers v_i and R. The preferred collisional relaxation pathways can then be rationalized in terms of preferred changes of v_i, J, R, C^n, and perhaps other labels. We shall see that the spectroscopic analysis offers us an intimate description of individual

(and individualistic) states, a cast of characters with colorful and sometimes surprising roles to play.

The rotation-vibration spectroscopy of $^{13}CD_4$ is of course very similar to that of CH_4 and the other isotopic variants. In discussing the levels of $^{13}CD_4$, then, analogies to CH_4 will prove to be of great help since the naturally abundant species has been studied in great detail over the years. Even when the analogies are not perfectly valid, they still can be illuminating.

Our discussion in this chapter will be structured to accomplish two objectives. First, we will review the "traditional" treatment of the spherical-top Hamiltonian in order to gain an understanding of the rovibrational energy levels that relies heavily on physical intuition. Then we will outline the particular spectroscopic approach used in the analysis of the $^{13}CD_4$ spectra. This modern approach yields little direct physical insight (to this author, at least), but it enables us to analyze the spectra with an unsurpassed degree of accuracy.

2.2 A Descriptive View of the Energy Levels of Methane

Methane is one of the most-studied molecules in polyatomic spectroscopy because of its small size and high symmetry. The high symmetry does not imply simplicity in its energy-level structure, as one might naively predict. It possesses four normal modes of vibration, three of which are degenerate; these are pictured in Fig. 2-1. An energy-level diagram of the vibrations of the $^{13}CD_4$ species is shown in Fig. 2-2. It can be seen here that, as in all of the methane species $^{12}CH_4$, $^{13}CH_4$, $^{12}CD_4$, and $^{13}CD_4$, the vibrational levels tend to fall in groups. The bending modes ν_2 and ν_4 in $^{13}CD_4$ lie near 1000 cm^{-1}. Near 2000 cm^{-1}, we find a second group comprised of the stretches ν_1 and ν_3, and the bending overtones and combinations $2\nu_2$, $\nu_2+\nu_4$, and $2\nu_4$. Because of this approximate grouping, a widespread terminology has developed wherein ν_2 and ν_4 are called the vibrational "dyad," and the five levels near 2000 cm^{-1} are called the "pentad." These convenient terms will find frequent use throughout this thesis. There is an octad of vibrational levels near 3000 cm^{-1} consisting of $\nu_1+\nu_2$, $\nu_1+\nu_4$, $3\nu_2$, $2\nu_2+\nu_4$, $\nu_2+2\nu_4$, $\nu_3+\nu_2$, $\nu_3+\nu_4$, and $3\nu_4$. Higher "polyads" occur at intervals of ~1000 cm^{-1} on the energy scale.

19
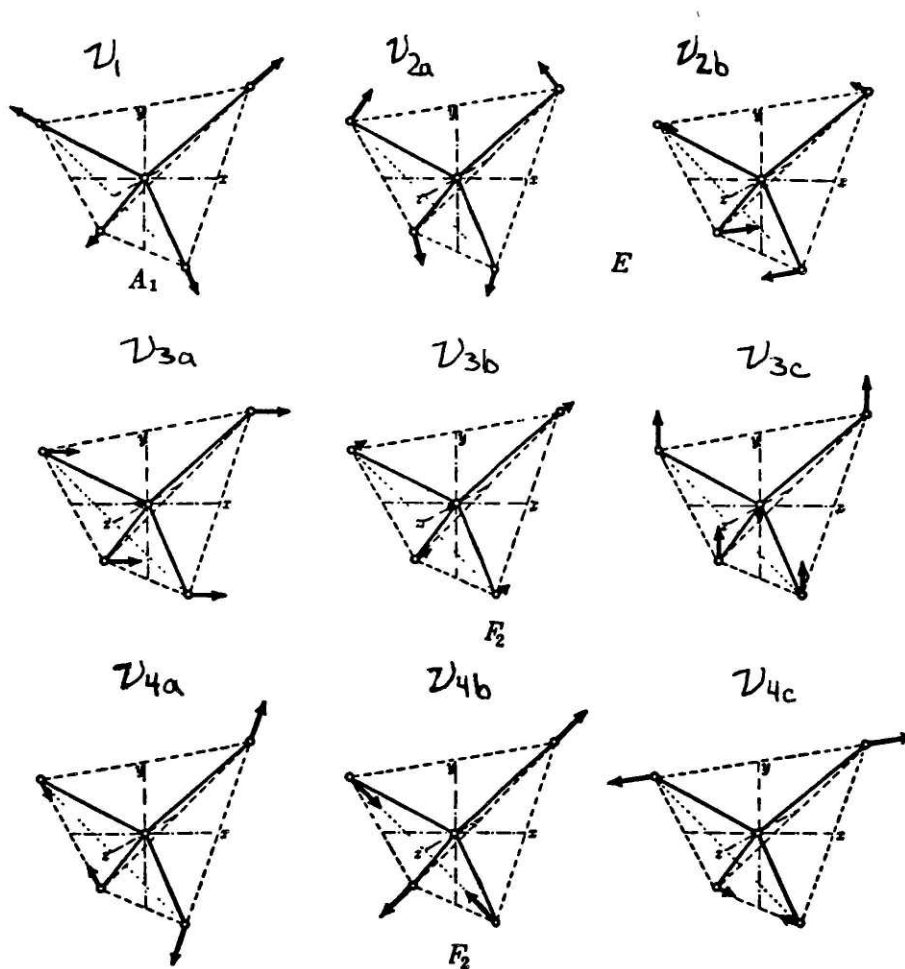
Figure 2-1: Normal Modes of a Tetrahedral XY₄ Molecule
Taken from Ref. [HERZ45].

Vibrational levels of $^{13}CD_4$
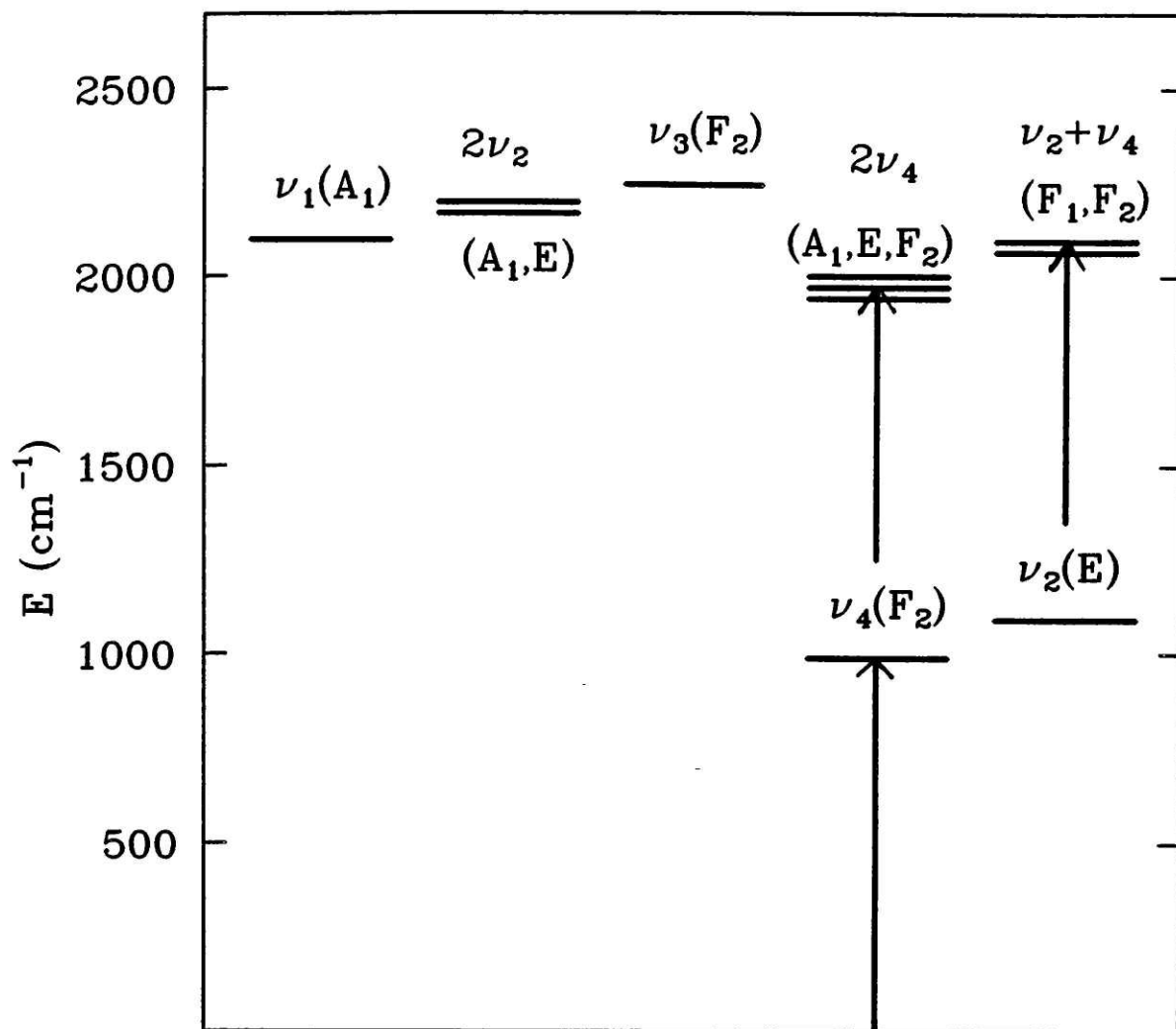
Figure 2-2: Vibrational Levels of $^{13}CD_4$

Anharmonic splittings of overtones not drawn to scale.

Arrows indicate the infrared-allowed $\Delta v_4 = 1$ transitions used in IRDR.

Extensive rotation-vibration interactions and purely vibrational ("anharmonic") interactions lead to a mixing of the normal mode vibrations even at low J. In the dyad (ν_2 and ν_4), it is well known that these interactions must be taken into account explicitly in order to arrive at a satisfactory rovibrational analysis. In the pentad region (stretches and bending overtones), these off-diagonal interactions must be included in the analysis for one to begin even to assign most of the spectroscopic transitions. Interactions between polyads, however, may be safely ignored due to the large energy differences (~ 1000 cm^{-1}). The only recent approaches that have been successful therefore use an effective Hamiltonian to describe a given polyad (ground vibrational state, dyad, pentad, etc.), and the normal mode vibrational levels within a polyad are treated collectively as a single vibrational unit [PPCP82,LOLCK81]. This polyad approach has been demonstrated to result in satisfactory spectroscopic analyses for the rotation-vibration levels of the CH_4 dyad and pentad, whereas the "isolated band" analyses of, for example, ν_1 of CH_4 allowed assignments only for low J values [OWY78]. Before proceeding to a detailed discussion of the polyad Hamiltonian, however, let us review the more elementary treatments of the ground vibrational state and the fundamental levels of the bending vibrations.

2.2.1 Rotational Levels of the Ground Vibrational State

The rotational level structure of a spherical-top molecule is described succinctly in Herzberg's books [HERZ45,HERZ66]. A more advanced treatment may be found in a more recent book by Papousek and Aliev [PAPOU82]. I will repeat a few essential details here for the sake of completeness and to establish the notation. Spherical tops have only one distinct moment of inertia, and therefore one angular momentum quantum number, J (the total angular momentum). Since in first order all of the levels corresponding to the projection quantum number K have the same energy, a level J has a degeneracy $2J+1$ (in addition to the M_J degeneracy of the same amount). Centrifugal distortion of the rotating molecule, however, causes both a shift of the level J and a splitting into components. This removes partially the $(2J+1)$-fold degeneracy. The centrifugally-split components are labelled by the symmetry species of the rotational wavefunctions, one of the characters A_1, A_2, E, F_1, F_2 of the T_d group to which the molecule belongs. (The number of components is determined by simple group-theoretical methods, as detailed by Herzberg [HERZ66]. It is roughly equal to J.) For some J values, there is more than one component of a given species; these are distinguished by a numerical counter, added on as a superscript, as in A_1^0, A_1^1, A_1^2,.... It is customary to refer to this notation generically as C^n, where $C \in \{A_1, A_2, E, F_1, F_2\}$ and $n = 0, 1, 2,....$

22

The complicated way in which a J level is split into tetrahedral components (or "fine-structure" components) has received a great deal of attention in the literature [PAPOU82]. The pattern of tetrahedral levels resulting from any rotation-vibration interaction is governed by high-order tensor operators in the Hamiltonian, and it appears at first glance to be a somewhat haphazard pattern. It is very interesting, however, that certain tetrahedral components experience similar shifts, so that "clusters" of nearly degenerate levels can be perceived within the haphazard pattern. These clusters have been interpreted by Dorney and Watson [DORN72] and by Harter and Patterson [HART84] in terms of classical and quantum-mechanical models for centrifugal distortion of the molecule that are striking in their reliance on physical intuition. The clusters are present in two types: eightfold-degenerate and sixfold-degenerate clusters. The eightfold-degenerate clusters take the form A_1-F_1-F_2-A_2 and F_1-E-F_2, and the sixfold clusters A_1-F_1-E (or A_2-F_2-E) and F_1-F_2. Centrifugal distortion caused by rotation about C_3 axes in methane gives rise to eightfold-degenerate clusters, since there are eight equivalent C_3 axes in the molecule. (There are four spatially distinct axes, but each has two directions of rotation.) Likewise, the sixfold-degenerate clusters are associated with the six equivalent S_4 axes in the molecule. Although the detailed theory of Harter and Patterson does not apply to the levels of $^{13}CD_4$ except for very high J ($J \simeq 20$), the intriguing clusters of levels are evident in the energy-level patterns. Their presence should be considered in any discussion of collisional energy transfer behavior.

2.2.2 Rotational Levels of the ν_4 Vibration

The spectroscopy of the ν_4 vibration of methane has been known in great detail since the theoretical groundwork was laid by Teller [TELL34] and Jahn [JAHN38] in the 1930s, and it is described in Herzberg's books [HERZ45,HERZ66]. The ν_4 vibration is a triply-degenerate bend (vibrational species F_2), the lower in energy of the two bends. The ν_2 bend is doubly degenerate (species E). The ν_4 vibration is infrared active, while ν_2, being a more symmetrical bending motion and therefore inducing no dipole moment, is inactive (in low order). The ν_4 vibration is subject to first-order Coriolis interaction, which completely removes the threefold degeneracy for non-zero J, and gives rise to a vibrational angular momentum l_4. For $v_4 = 1$, l_4 has only the value $l_4 = 1$.

The vibrational angular momentum is coupled to the rotational angular momentum; this is represented by a term in the Hamiltonian that can be written as $-2B\zeta \mathbf{J} \cdot \mathbf{l}_4$, where $\mathbf{J}$ is the total angular momentum operator and the Coriolis constant ζ is the magnitude of the vibrational angular momentum in the ν_4 state (in units of $h/2\pi$) [PAPOU82]. (For $^{13}CD_4$, $\zeta_4 \simeq 0.36$.) B is the

familiar rotational constant. We may define $R = J-1$ [HECHT60] so that R is the "purely rotational" angular momentum vector. Then, by quantum-mechanical vector addition, $R = J+1$, J, and $J-1$, and a state $|\nu_4, J\rangle$ is split into three states $|\nu_4, J, R\rangle$, removing the vibrational degeneracy of ν_4. The resulting energy levels are (in the absence of other effects):

$$E(J, R=J+1) = BJ(J+1) + 2B\zeta J$$
$$E(J, R=J) = BJ(J+1) - 2B\zeta$$
$$E(J, R=J-1) = BJ(J+1) - 2B\zeta(J+1)$$

The three Coriolis sublevels are designated F^+, F^0, and F^- as $(R - J) = +1, 0, -1$, respectively [HERZ45].

Thus, the rotational levels of ν_4 have two important angular momentum quantum numbers, J and R. R is associated with the overall rotation of the nuclear framework, whereas J includes in addition the angular momentum arising from the vibrational motion. Physically, this vibrational motion is different from that indicated by the normal mode coordinates in Fig. 2-1. As a result of Coriolis interaction, we must take linear combinations of the three components of ν_4 in Fig. 2-1 so that the resulting three oscillations no longer mix in consequence of the Coriolis force, which operates when the molecule is simultaneously vibrating and rotating. The new normal mode oscillations, equivalent solutions to the purely vibrational problem, entail movement of the outer atoms of the molecule in elliptical orbits perpendicular to the bond axes. This is described in detail by Herzberg. It is interesting to note that the $J=0$ level of ν_4 occurs in the F^+ Coriolis sublevel, so that $R=1$. The molecule rotates in the $J=0$ state! Of course, this rotation occurs so as to cancel the angular momentum of the vibrational motion.

In addition to the rotational quantum numbers J and R in ν_4, we have the usual tetrahedral components C^n. These are split by centrifugal distortion, as in the ground vibrational state, and also by rotation-vibration interactions. In ν_4, however, these splittings are much larger than in the ground state. The splitting pattern is now extremely complicated since it is influenced by a number of factors. The work of H.A. Jahn in 1938 demonstrated that the most important of these factors is the interaction of the levels of ν_4 with those of the neighboring vibration ν_2. This feature of the energy level spectrum of $^{13}CD_4$ will prove to be extremely important to its collisional behavior, so we will devote a brief discussion to this topic.

24

2.2.3 Coriolis Interaction Between ν_4 and ν_2

The ν_4 vibrational mode of methane interacts quite strongly with the ν_2 vibration via the Coriolis force. This type of Coriolis interaction, between disparate normal modes, should be distinguished from the type we discussed previously, which occurs among the three F_2 vibrations of a degenerate set. The $\nu_4-\nu_2$ interaction is termed "second-order Coriolis interaction" by Herzberg to reflect this distinction [HERZ45]. This is a classic case of Coriolis interaction between vibrations and was given early treatment by Jahn [JAHN38]. In all of the methane isotopomers, the $\nu_4-\nu_2$ energy separation is fairly small ($\sim$200 cm^{-1} in CH$_4$, $\sim$100 cm^{-1} in ^{13}CD$_4$); in each case the perturbation is pervasive throughout the set of states J = 1 to 20 despite the absence of a curve crossing. It is principally for this reason that a satisfactory analysis of the ν_4 levels can be achieved only by a simultaneous analysis of the dyad levels, ν_2 and ν_4, taking into account explicitly all of the important interaction terms in the Hamiltonian.

The strong Coriolis interaction between ν_2 and ν_4 has a number of important consequences. The ν_2 vibration becomes weakly allowed in infrared absorption. In both ν_4 and ν_2, J levels are split by a significant amount into their tetrahedral components; the levels of ν_2, the higher frequency vibration, are pushed up in energy, and the levels of ν_4 are pushed down. (For J$\sim$10 in ^{13}CD$_4$, the perturbation is as much as 10 cm^{-1}.) But one of the most notable consequences of the Coriolis interaction is that for a given J and R in ν_4, the different tetrahedral sublevels C^n experience different perturbations. (The Coriolis interaction matrix elements have a dependence on C^n.) Thus, for J=R=11 in ν_4 of ^{13}CD$_4$, there are nine tetrahedral sublevels. The perturbation of these due to Coriolis mixing with ν_2 ranges from -0.5 to -10 cm^{-1}; likewise, the admixture of ν_2 in these levels ranges from 1% to 9%. The varying amounts of perturbation by ν_2 lead to the result that the nine levels with J=R=11 in ν_4 "fan out" in the complicated manner shown in Fig. 2-3.

Figure 2-3: J=11 Levels of the $^{13}CD_4$ Dyad

Shown in the left column are the "deperturbed" energy levels of ν_2 and ν_4, in the absence of the ν_2/ν_4 Coriolis interaction. The ν_4 levels are split into R = 10, 11, and 12. The interaction between the vibrations leads to the energy levels in the center column, where the tetrahedral sublevels C^n are displayed. The right-hand side of the diagram shows the amount of Coriolis mixing in each eigenstate; the length of the bar for each level corresponds to the percentage of vibrational character from the other vibrational state. The energy level separations are drawn to scale, except that the separation between ν_2 and ν_4 levels, indicated by the dashed line, is much greater than shown (it is ~ 84 cm^{-1}).

Dyad J=11 level structure and mixing

ν_2

ν_4

0% 10%

Energy

R=12

R=11

R=10

10 cm^{-1}
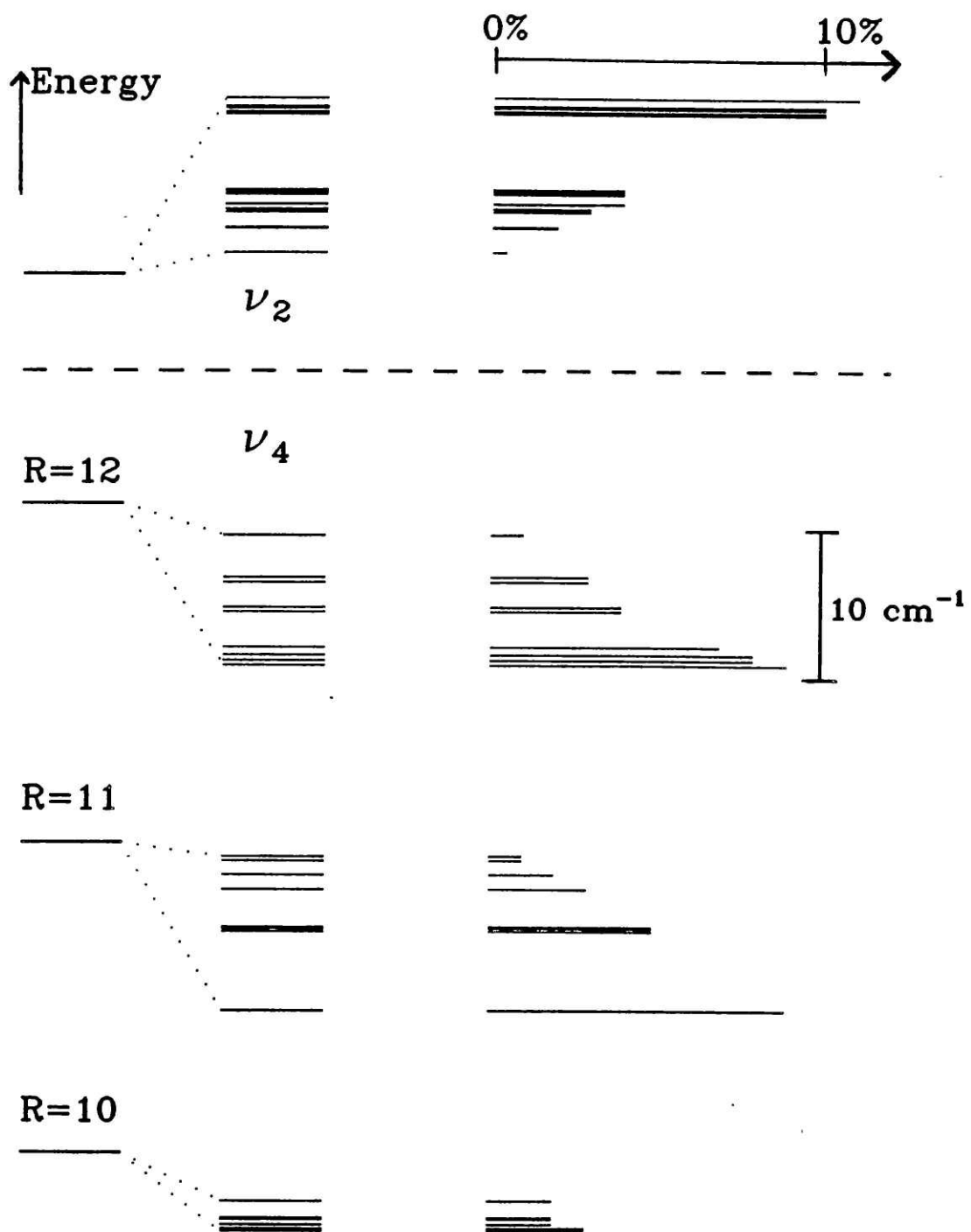
Another consequence of the interaction with ν_2 is that in the ν_4 vibration, the quantum number R is slightly spoiled. The rovibrational eigenstates must be written as linear combinations of basis functions of different R values. R mixing actually occurs through the combined effects of first- and second-order Coriolis and centrifugal interactions, and higher-order terms in the Hamiltonian involving the quantity $\mathbf{J} \cdot \mathbf{l}_4$ [PAPOU82]. We might consider the phenomenon to be a consequence of the difficulty of separating rotational from vibrational motion, made all the more complex by the mixing of two vibrations (and the consequent introduction of another vibrational angular momentum quantity, $\mathbf{l}_{24}$). The contribution of "purely rotational" energy (associated with the R quantum number) to the total energy of a state $|\nu_4, J, R\rangle$ is no longer easily discerned. This important fact must be remembered when one attempts to interpret collisional energy transfer behavior among these rovibrational eigenstates.

In the dyad vibrational levels of methane, there are only two good quantum labels: J and the rovibrational symmetry species C. (Levels of different C cannot be mixed by interactions in the spherical-top Hamiltonian, which must satisfy certain symmetry restrictions [PAPOU82].) We should point out, though, that in $^{13}CD_4$, R remains a fairly good quantum number for moderate J values. It is possible to work out systematically the contributions of different R states to a given eigenstate. This will be discussed in Chapter 5, where we will see that J = 11 levels have at most a 4% contribution from a foreign R state.

As we discussed above, the different tetrahedral sublevels within a $|\nu_4, J, R\rangle$ state experience different perturbations by the rotational levels of ν_2. The resulting energy-level pattern is a complex one, but there is order within the apparent disarray. One can see in Fig. 2-3 that some of the levels appear to be clustered together, just as in the case of centrifugal distortion in the ground vibrational state. The same eightfold-degenerate and sixfold-degenerate clusters are very much in evidence in the pattern. Apparently, there are certain groups of tetrahedral sublevels that suffer similar perturbations by ν_2. Physically, this occurs presumably because the magnitude of the (second-order) Coriolis force exerted on a methane molecule in the ν_4 state depends strongly on the orientation of the total angular momentum vector in the molecule-fixed frame. Orientations of the vector $\mathbf{J}$ that are equivalent (i.e., related through a symmetry operation of the molecule) are associated with similar Coriolis perturbations.

We should point out, however, that not all of the tetrahedral sublevels belong to clusters. This is especially true at low J, where only a few levels actually do belong to clusters. The reasons for this behavior in circumstances in which centrifugal splitting is the dominant interaction present

28

have been explained thoroughly by Harter and Patterson [HART84]. In cases where rotation-vibration interactions are the main force behind tetrahedral splitting, however, the cluster dynamics are not fully understood. This of course is the situation for the ν_4 level of $^{13}CD_4$.

2.3 Spectroscopic Considerations for the Pentad

The experimental scheme for studying collisional energy transfer in the dyad of $^{13}CD_4$ (see Fig. 2-2) consists of pumping selected transitions in the ν_4 fundamental ($\nu_4 \leftarrow 0$) and probing transitions of the hotband ($2\nu_4 \leftarrow \nu_4$). Hotband transitions of the type ($\nu_2 + \nu_4 \leftarrow \nu_2$) are also needed to study energy transfer from ν_4 to ν_2. Thus, we need a full rotational analysis for the levels ν_2, ν_4, $2\nu_4$, and $\nu_2 + \nu_4$ for the range of J values important in the room temperature Boltzmann distribution, J = 0 to 20. Let us consider what this requires.

Herzberg describes the overall appearance of the ν_4 spectrum, and it consists of simple P, Q, and R branches at low resolution (~ 1 cm^{-1}) [HERZ45]. At Doppler-limited resolution, a given R(J) transition is broken up into its tetrahedral components, fully resolved (there are $\sim J$ components). The P and Q branches of ν_4 overlap considerably, causing the tetrahedral components of lines of different J to be interspersed quite thoroughly, but they are still resolvable except for accidental overlaps. Coriolis interaction with ν_2 is strong, so that tetrahedral components are separated more widely than are lines of different J, making assignment an involved process.

In order to understand the $2\nu_4 \leftarrow \nu_4$ hotband transition, we need to analyze the $2\nu_4$ level through the weak overtone band $2\nu_4 \leftarrow 0$. The $2\nu_4$ level is sixfold degenerate in first order, since it has species $A_1 + E + F_2$ [HERZ45]. It is subject to the same first-order Coriolis interaction that we discussed for the ν_4 fundamental level. In addition, it is besieged by a number of rotation-vibration perturbations by the neighboring levels of the pentad: Coriolis interactions with $\nu_2 + \nu_4$ ($F_1 + F_2$) and with $2\nu_2$ ($A_1 + E$), Fermi interactions with ν_1 (A_1) and with ν_3 (F_2), and resonances with $\nu_2 + \nu_4$ and $2\nu_2$ of the Darling-Dennison variety [LOLCK81]. All of these effects combine to produce an extremely complicated pattern of tetrahedral splittings for a given J_R level. The resulting spectrum ($2\nu_4 \leftarrow 0$) is exceedingly complex and very difficult to analyze with an effective Hamiltonian that treats $2\nu_4$ as an isolated state [PIERRE77,PIERRE80].

The degree of complexity was perhaps first appreciated in 1960, when Plyler *et al.* at the National Bureau of Standards recorded the infrared spectrum of CH_4 in the region 2470 to 3200

29

cm^{-1}, encompassing all of the bands of the CH_4 pentad [PLYLER60]. While the strong ν_3 transitions were readily assigned, there remained a mass of weak lines not belonging to any recognizable pattern, attributed to $2\nu_4$ and $\nu_2 + \nu_4$. Only after 20 years of work by a number of spectroscopists could the thousands of lines be confidently identified with rovibrational names, and a list of physically reasonable spectroscopic constants was finally deduced [LOLCK82,PPCP82]. From all of this work emerged the realization that an accurate and complete analysis of the pentad vibrational states could be achieved only through a comprehensive treatment of all five states together in one large Hamiltonian matrix. The accuracy of the analysis is of key importance since the high density of rovibrational lines can lead to incorrect assignments if the calculated frequencies are not close to reality. Let us turn now to the specific approach used for the study of the levels of $^{13}CD_4$.

2.3.1 The Champion-Pierre Approach to the Polyad Hamiltonian

In 1977, a general formalism was advanced by Jean-Paul Champion to determine all possible rotation-vibration operators in the Hamiltonian of tetrahedral XY_4 molecules, to any order of approximation and for any vibrational level [CHAMP77]. Champion and Gérard Pierre, in Dijon, France, developed explicit expressions based on the formalism for operators associated with overtone and combination levels [CHAMP80]. Poussigue *et al.* then developed a full Hamiltonian for the simultaneous treatment of all of the pentad levels, including all possible interaction terms up to third order in rovibrational operators [PPCP82]. (Operator order is specified by the well-known Amat-Nielsen classification scheme [PAPOU82].) The Hamiltonian has been applied to the pentads of CH_4 [PPCP82] and $^{12}CD_4$ [LOLCK85].

In Champion's formalism, a rotation-vibration tensor operator T is constructed (in the usual way) by coupling rotational and vibrational operators R and V in the T_d group. This can be written in generalized form as:

$$T_{n_+ n_-}^{\Omega(K,n\Gamma)\Gamma_+\Gamma_-} = \left[R^{\Omega(K,n\Gamma)} \times (-1)^K V_{n_+ n_-}^{\Gamma_+\Gamma_-(\Gamma)} \right]^{(A_1)} \qquad (2.1)$$

where the tensor operator T is labelled as follows:

Ω = degree of rotational part of operator

K = tensor rank of rotational part

$n\Gamma$ = symmetry of rotational operator in T_d, with numerical index

Γ_+, Γ_- = symmetries of ladder operators comprising V

n_+, n_- = vibrational indices of ladder operators.

R and V are described in detail by Champion [CHAMP77.CHAMP78]. The spherical top Hamiltonian then takes the form:

$$H = \sum_{\Omega,K,n\Gamma} t_{n_+n_-}^{\Omega(K,n\Gamma)\Gamma_+\Gamma_-} \cdot T_{n_+n_-}^{\Omega(K,n\Gamma)\Gamma_+\Gamma_-} \qquad (2.2)$$

where t labels the spectroscopic parameter associated with the operator T. The advantage of the highly indexed and formalized tensorial notation is that, as Champion has shown, the matrix element of an arbitrary rovibrational operator between any two rovibrational states can be expressed in a single equation. Application of the Wigner-Eckart theorem yields:

$$\left\langle \Psi_{\Gamma v}'' \left| T_{n_+n_-}^{\Omega(K,n\Gamma)\Gamma_+\Gamma_-} \right| \Psi_{\Gamma v}' \right\rangle = e^{i\phi}(-1)^J(-1)^{\Gamma+C+C_\Gamma'+C_v''}[\Gamma]^{-\frac{1}{2}}$$

$$\times K\binom{K \quad J \quad J}{\Gamma \quad n'C_\Gamma'' \quad n''C_\Gamma''}\binom{C_v'' \quad C_\Gamma' \quad C}{C_\Gamma'' \quad C_v' \quad \Gamma}[-4J(J+1)/\sqrt{3}]^{(\Omega-K)/2}$$

$$\times \left[\frac{K!(2J+K+1)!}{(2K-1)!!(2J-K)!}\right]^{\frac{1}{2}} \left\langle \Psi_v'' \left\| {}^{(-1)^K}V_{n_+n_-}^{\Gamma_+\Gamma_-}(\Gamma) \right\| \Psi_v' \right\rangle$$

(2.3)

In this equation, Ψ_{rv} is generated as a product of rotational and vibrational wavefunctions, and carries the following indices:

$$\left[\Psi^{(J,nC_r)} \times \Psi_v^{(C_v)}\right]_\sigma^{(C)} = |J,nC_r;v,C_v;C\sigma\rangle$$

The terms in Eqn. (2.3) are fully explained in Refs. [CHAMP77,PPCP82], so I will not go into detail here. Values of the "isoscalar factor" K and of the "6-C" coefficients are listed in various references [PPCP82]. The quantity $<\Psi''||V||\Psi'>$ is a reduced matrix element of the vibrational operator. This equation can be programmed easily and used to evaluate all of the matrix elements occurring in the pentad matrix. It applies to the Hamiltonian in any order of approximation.

In every spectroscopic analysis, one is faced with a decision as to what terms to include in the Hamiltonian, under the usual constraint of keeping the matrix down to a manageable size. The philosophy espoused by the spectroscopists in Dijon and Paris is characterized by *theoretical consistency*, as expressed in the following important principle: *the part of the Hamiltonian off-diagonal in the vibrational quantum numbers is developed to the same order as the diagonal part* [PPCP82]. In other words, all rotation-vibration interaction terms allowed by symmetry are included explicitly in *H*, up to a certain order in rovibrational operators. This choice represents a

deviation from most approaches employed by spectroscopists in rotation-vibration analyses. (An alternative treatment of the methane pentad has been developed by Lolck and Robiette [LOLCK82].) The traditional approach has been to choose terms only on the basis of their expected contribution to the energy, and regardless of rovibrational order. Higher-order terms are neglected or included according to their empirical effects on the spectroscopic fit. The more systematic approach advocated by Champion and Pierre eliminates the arbitrary nature of the selection of terms.

The chief advantage of the systematic approach is its generality. All vibrational states of the molecule are treated in precisely the same way. When one desires to extrapolate the analysis to higher vibrational levels, as from the dyad to the pentad in methane, the spectroscopic parameters derived from the lower polyad may be transferred to the higher polyad without changes. One adds on new terms if they arise by the prescription of Eqn. (2.1), that is, if a new physical effect plays a role not applicable in the lower polyad.

The disadvantage of the approach is that the spectroscopic constants are symbolized with a bewildering array of superscripts and subscripts, as shown in Eqn. (2.2). This is because when one includes all terms allowed by symmetry, many of the terms bear no direct physical significance, so it no longer makes sense to rely on the traditional spectroscopic notation. It is possible to find the relationships between the constants $t^{\Omega(K,n\Gamma)}$ and the more traditional ν_0, B_v, $B\zeta$, D, H, etc. [PPCP82,CHAMP77], but this is very difficult for the higher-order constants, and has not yet been done in full. Thus, we lose a physical feeling for what many of the constants represent. Also, the tensorial formalism does not make use of the approximate quantum number R.

2.3.2 Spectroscopic Data for $^{13}CD_4$

Spectral data for the ground state, dyad, and pentad of $^{13}CD_4$ were gathered from a variety of sources. The most important of these are Fourier transform infrared (FTIR) spectra taken by A. Valentin and L. Henry at the Université Pierre et Marie Curie in Paris [PIERRE87,MILLOT86]. These spectra were obtained on a state-of-the-art FTIR apparatus that permits resolution of features at nearly the Doppler-broadened limit. Spectra were collected in two regions, from 920 to 1200 cm^{-1} for the dyad and from 1800 to 2300 cm^{-1} for the pentad. In the dyad region spectra were taken at two pressures, 0.5 Torr and 4 Torr; the higher pressure spectrum allowed the weak lines of the hotband spectrum (pentad←dyad) to be observed. Likewise, the pentad spectrum was done at three pressures, since the fundamental and overtone bands display a wide range of intensities. In

the dyad region, the lines display an instrumental width (FWHM) of about 90 MHz, and in the pentad region about 180 MHz. The accuracy of the measured line frequencies, relative to calibration lines, is 3-10 MHz.

Transitions from the ground vibrational state to the overtone levels in the pentad are only weakly allowed (the transition moment is $\mu \sim 0.005$ D [PASC87]). Transitions to the totally-symmetric stretching level $\nu_1(A_1)$ are even more strictly forbidden, however, since there is in first order no dipole moment induced by the motion. Likewise, the vibrational sublevels in the pentad of A_1 symmetry (one sublevel in $2\nu_2$ and one in $2\nu_4$) are strongly forbidden in absorption by a symmetry selection rule [HERZ45]. For data on the ν_1 vibration, we must turn to Raman spectroscopy. Stimulated Raman Spectroscopy, in particular, offers the high resolution required to distinguish rotational features in methane. Guy Millot and collaborators from the Laboratoire de Spectronomie in Dijon have obtained Stimulated Raman data for the levels $\nu_1(A_1)$, $2\nu_2(A_1)$, and $2\nu_4(A_1)$, and also $\nu_2+\nu_4(F_1+F_2)$, which interacts strongly with ν_1. Spectra were taken in the regions 1945-1951 cm^{-1}, 2075-2110 cm^{-1}, and 2182-2185 cm^{-1}, with resolution $\sim$60 MHz and precision $\sim$30 MHz [MILLOT87].

We observed a number of hotband transitions by IRDR, as will be discussed in Chapter 4. While the accuracy of our frequency measurements is rather limited ($\sim$60 MHz), the double resonance technique determines with certainty that a given transition observed by FTIR is a hotband transition, and not simply a weak "forbidden" transition of the fundamental. In addition, IRDR allows us to determine the symmetry type A, E, or F of a transition. In the FTIR spectrum, "forbidden" transitions of the fundamental and hotband transitions of all symmetry types are observed together with similar intensities. The IRDR observations are useful in narrowing the range of possibilities for the identity of a given line. The frequency measurement provided by FTIR can then be used in the fitting procedure.

Another source of valuable spectroscopic data for $^{13}CD_4$ is rotational spectroscopy. Although forbidden in a first order of approximation by the absence of a permanent dipole moment, pure-rotational transitions in methane are weakly allowed by the small centrifugally-induced dipole moment (10^{-5}-10^{-6} D) in rotational states of $J>0$ [WATSON71,FOX71,FOX72]. Microwave Fourier transform measurements have been performed in the region 8-18 GHz, and IR-laser—radiofrequency double resonance measurements in the region 0.9-11 GHz [KREIN87,KREIN83]. Transitions at these frequencies take place between the tetrahedral sublevels of a J state. The intrinsically high accuracy of these measurements permits the accurate determination of some of the higher-order tensorial constants associated with centrifugal distortion.

2.3.3 The Dyad Analysis

Previous analyses of the dyad of $^{13}CD_4$ were reported by Loëte [LOETE83] and McDowell [MCDOW85]. Neither was sufficient for our purposes, though. The Loëte analysis included only a small number of transitions in the ν_4 band, measured in a sample of CD_4 with the natural mixture of carbon isotopes. The McDowell analysis used a "low-resolution" (~ 0.04 cm^{-1}) spectrum, and Robiette's dyad Hamiltonian [ROBI81]. In order to obtain a reliable set of constants for the tensorial Hamiltonian, then, G. Pierre analyzed the dyad levels near 1000 cm^{-1}, using the large set of computer programs established at the Laboratoire de Spectronomie Moléculaire et Instrumentation Laser (SMIL) in Dijon. The Hamiltonian was developed to 6th order for the ground vibrational state, and to 5th order for the dyad, yielding 10 spectroscopic parameters associated with the ground state and 40 for the dyad. With a 5th-order treatment for the dyad, the parameters can be refined so as to reproduce the spectrum to within experimental accuracy. The spectrum is fitted up to dyad $J=25$. The derived spectroscopic parameters are shown in Table 2-1. In practice, 10 of the 40 dyad parameters are fixed to zero. This is necessary due to a subtle difficulty pointed out by Tyuterev *et al.*: in an effective Hamiltonian constructed by symmetry arguments alone, some parameters will in fact depend on each other [TYUT84,PEREV84]. This causes some parameters to take on ambiguous values, so that a "reduced" Hamiltonian must be used with fewer parameters. This is not a problem particular to the Champion-Pierre approach, but rather arises in any effective vibration-rotation Hamiltonian for a restricted group of vibrational levels that is obtained by contact transformation of the most general Hamiltonian.

The dyad energy levels deduced from the analysis are shown in Figs. 2-4 and 2-5. Figure 2-5 is a reduced energy-level diagram in which we plot on the ordinate the quantity

$$E_{total} - [t_0^{2(0,A1)}J(J+1) + t_0^{4(0,A1)}J^2(J+1)^2 + t_0^{6(0,A1)}J^3(J+1)^3].$$

In the traditional notation [PAPOU82], this is written

$$E_{total} - [B_0J(J+1) - D_0J^2(J+1)^2 + H_0J^3(J+1)^3].$$

The rigid-rotor contribution and the principal centrifugal distortion terms are subtracted off. One can see in this plot that the tetrahedral splittings of J_R levels are smaller than the separations between Coriolis sublevels F^+, F^0, F^-, except at high J, where the F^+ and F^0 components begin to converge. In Fig. 2-3, we plot the energy levels for $J=11$, and also indicate the degree of mixing with ν_2 for each individual C^n level. The tetrahedral components within a J_R level that are lowest in energy contain the largest amounts of ν_2; they have been "pushed away" from ν_2 by the greatest amount.

Table 2-1. Fitted spectroscopic parameters of the ground state and dyad.

$\Omega(K,n\Gamma)$	n_+	n_-	Value (st. dev.)	units	Other notation
			Ground state		
$2(0, A_1)$	0	0	2.6328902(12)	cm^{-1}	B_0
$4(0, A_1)$	0	0	-2.75864(85)	$10^{-5}\ cm^{-1}$	$-D_0$
$4(4, A_1)$	0	0	-7.45839(30)	$10^{-7}\ cm^{-1}$	$-\tfrac{1}{4}\sqrt{(15/2)}D_t$
$6(0, A_1)$	0	0	7.88(21)	$10^{-10}\ cm^{-1}$	H_0
$6(4, A_1)$	0	0	-1.9997(66)	$10^{-11}\ cm^{-1}$	$(3/16)\sqrt{(5/2)}H_{4t}$
$6(6, A_1)$	0	0	-6.544(17)	$10^{-12}\ cm^{-1}$	$-(1/64)\sqrt{(231/2)}H_{6t}$
$8(0, A_1)$	0	0	-2.3(16)	$10^{-15}\ cm^{-1}$	
$8(4, A_1)$	0	0	-4.72(35)	$10^{-16}\ cm^{-1}$	
$8(6, A_1)$	0	0	-3.23(16)	$10^{-16}\ cm^{-1}$	
$8(8, A_1)$	0	0	-2.55(9)	$10^{-17}\ cm^{-1}$	
			ν_2 **vibrational state**		
$0(0, A_1)$	2	2	1091.801238(22)	cm^{-1}	ν_2
$2(0, A_1)$	2	2	0.0	*	
$2(2, E)$	2	2	-9.74007(41)	$10^{-3}\ cm^{-1}$	
$3(3, A_2)$	2	2	3.2098(16)	$10^{-5}\ cm^{-1}$	
$4(0, A_1)$	2	2	-7.8258(98)	$10^{-7}\ cm^{-1}$	
$4(2, E)$	2	2	-8.968(91)	$10^{-8}\ cm^{-1}$	
$4(4, A_1)$	2	2	0.0	*	
$4(4, E)$	2	2	0.0	*	
$5(3, A_2)$	2	2	-4.51(22)	$10^{-10}\ cm^{-1}$	
			ν_2/ν_4 **interaction**		
$1(1, F_1)$	2	4	-5.203913(17)	cm^{-1}	
$2(2, F_2)$	2	4	-2.12914(10)	$10^{-2}\ cm^{-1}$	
$3(1, F_1)$	2	4	-1.01684(40)	$10^{-4}\ cm^{-1}$	
$3(3, F_1)$	2	4	-2.0456(20)	$10^{-5}\ cm^{-1}$	
$3(3, F_2)$	2	4	-1.0511(32)	$10^{-5}\ cm^{-1}$	
$4(2, F_2)$	2	4	-2.69(14)	$10^{-8}\ cm^{-1}$	
$4(4, F_1)$	2	4	-4.55(22)	$10^{-8}\ cm^{-1}$	
$4(4, F_2)$	2	4	-4.63(10)	$10^{-8}\ cm^{-1}$	
$5(1, F_1)$	2	4	-3.95(28)	$10^{-10}\ cm^{-1}$	
$5(3, F_1)$	2	4	1.096(23)	$10^{-9}\ cm^{-1}$	
$5(3, F_2)$	2	4	3.81(37)	$10^{-10}\ cm^{-1}$	
$5(5, F_1)$	2	4	0.0	*	
$5(5, F_1)$	2	4	0.0	*	
$5(5, F_2)$	2	4	-1.118(29)	$10^{-9}\ cm^{-1}$	

Table 2-1 (cont.)

$\Omega(K,n\Gamma)$	n_+	n_-	Value (st. dev.)	units	Other notation
			ν_4 vibrational state		،
$0(0, A_1)$	4	4	989.250350(16)	cm^{-1}	ν_4
$1(1, F_1)$	4	4	4.0324109(49)	cm^{-1}	$3\sqrt{2}B\zeta_4$
$2(0, A_1)$	4	4	-4.5718(23)	$10^{-4}\ cm^{-1}$	
$2(2, E)$	4	4	-2.86282(42)	$10^{-3}\ cm^{-1}$	
$2(2, F_2)$	4	4	-1.097037(37)	$10^{-2}\ cm^{-1}$	
$3(1, F_1)$	4	4	0.0	*	
$3(3, F_1)$	4	4	-5.5264(24)	$10^{-5}\ cm^{-1}$	
$4(0, A_1)$	4	4	0.0	*	
$4(2, E)$	4	4	-1.1531(69)	$10^{-7}\ cm^{-1}$	
$4(2. F_2)$	4	4	0.0	*	
$4(4, A_1)$	4	4	-2.743(24)	$10^{-8}\ cm^{-1}$	
$4(4, E)$	4	4	3.877(11)	$10^{-7}\ cm^{-1}$	
$4(4. F_2)$	4	4	4.4211(66)	$10^{-7}\ cm^{-1}$	
$5(1, F_1)$	4	4	1.286(35)	$10^{-9}\ cm^{-1}$	
$5(3, F_1)$	4	4	0.0	*	
$5(5.0F_1)$	4	4	0.0	*	
$5(5,1F_1)$	4	4	-8.03(25)	$10^{-10}\ cm^{-1}$	

Notes: Parameters (*) with zero values were fixed to zero to account for ambiguities in the Hamiltonian, as explained in the text. The relationships given in the last column are from Ref. [LOETE83]. The principal ν_2/ν_4 interaction constant is $1(1, F_1)$, which is related to the traditional $B\zeta_{24}$.

Figure 2-4 (next page): Energy Levels of the $^{13}CD_4$ Dyad

Figure 2-5 (following page): Reduced Energy Levels of the $^{13}CD_4$ Dyad
$E_{red} = E - B_0 J(J+1) - \ldots$ (as explained in the text). The position of the level $(\nu_4, J=11, F_2^7)$, the initial level for the energy transfer experiments, is indicated by the pointer. On the right, the designations of the Coriolis sublevels of ν_4 are given.
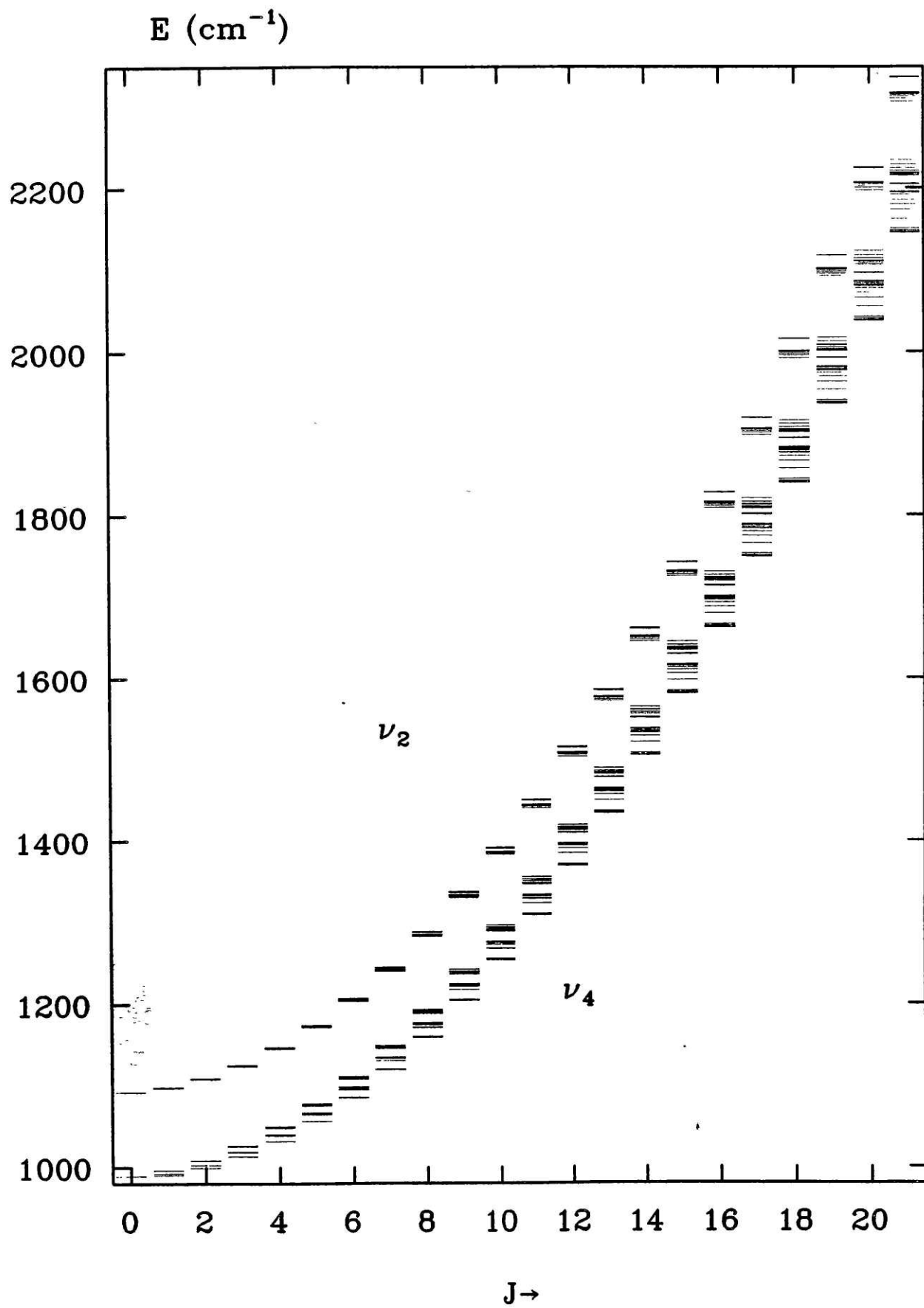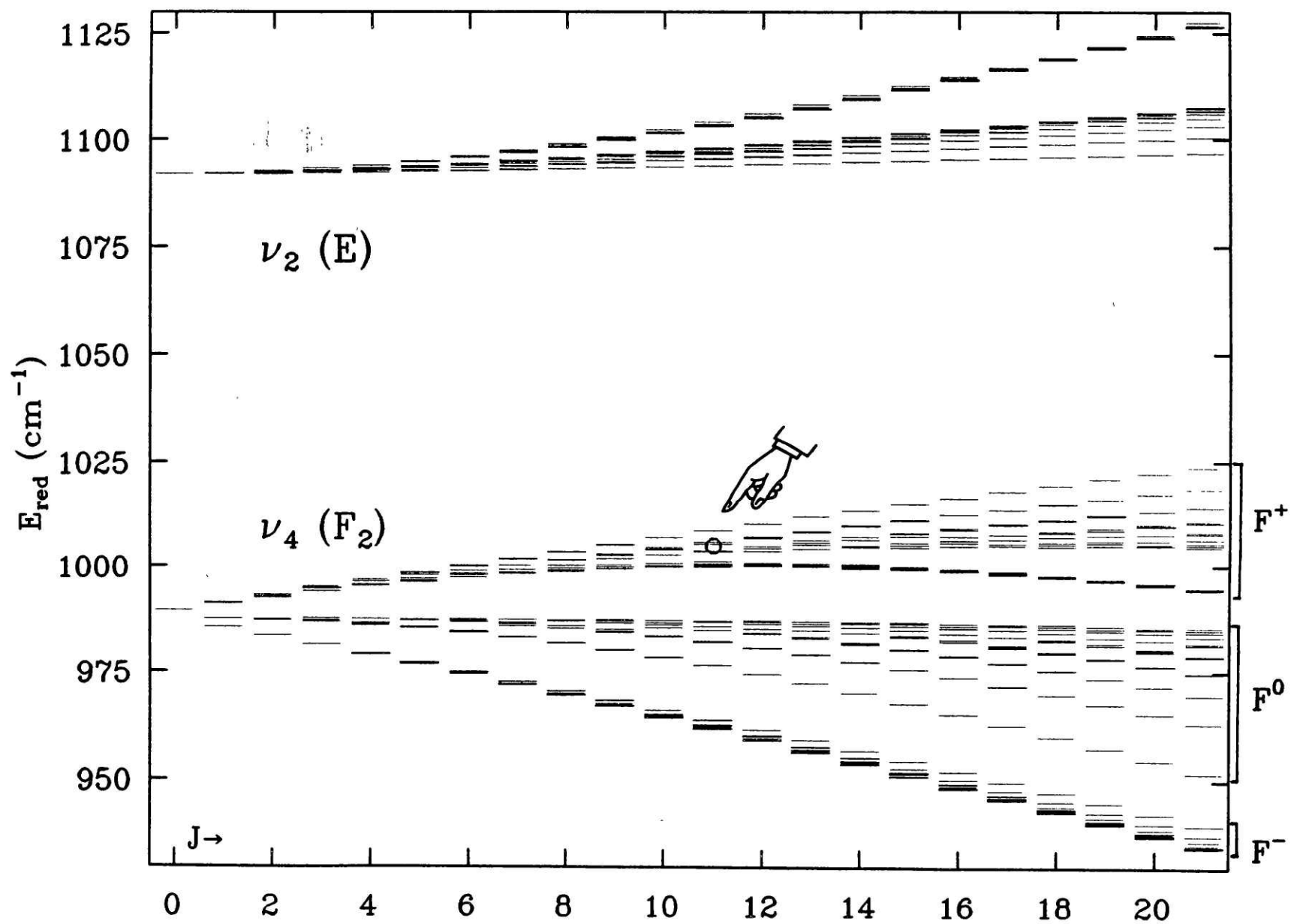
2.3.4 The Pentad Analysis

Once the dyad parameters were well known, the pentad analysis could begin. The analysis is a very sizeable undertaking because of its numerical complexity. Some of the five vibrational levels are degenerate, so there are altogether 19 vibrational basis functions to be used. There are some 3500 rotational levels with $J \leq 20$. The Hamiltonian for this problem is developed to third order, resulting in 63 terms, of which 42 are off-diagonal in the vibrational quantum numbers v_1, v_2, v_3, v_4. The 40 non-zero terms determined in the dyad analysis are transferred to the pentad analysis, with fixed values [PPCP82].

The assignment of transitions may be done in the usual way by confining the analysis at first to low J values and extrapolating to higher J in steps, allowing an increasing number of parameters to vary freely. An important tool used in making many assignments is brought about by the following realization: two transitions terminating in the same level will have similar residuals in $\nu_{obs} - \nu_{calc}$ if their assignments are correct. This is true because the relative energies of the ground state rotational levels are known to extremely high accuracy, so that one may assume that the residual arises solely from the uncertainty of the upper state energy. Another important observation used to advantage in the assignment process is that transitions to clustered tetrahedral levels usually show very similar residuals. The spacings between clustered levels can usually be predicted to higher accuracy than the absolute energy of the cluster.

By means of successive extrapolations and least-squares refinements, we were able to push the analysis to a moderately high J value ($J \sim 11$). At this point, we could attempt to model the hotband transitions, pentad$\leftarrow$dyad. This requires a knowledge of both the level energies and the intensities of transitions between individual tetrahedral components [PIERRE80]. G. Pierre assembled an additional computer program to perform this intensity calculation, starting with the eigenfunctions computed for the pentad in the maturing pentad analysis. As a first approximation, the transition moment for the ν_4 vibration was the only one considered. This is a reasonable approximation since the $\Delta v_4 = 1$ pentad$\leftarrow$dyad transitions are the only ones allowed in the harmonic approximation. (Specifically, these are $2\nu_4 \leftarrow \nu_4$ and $\nu_2 + \nu_4 \leftarrow \nu_2$; Δv_2 transitions of the type $2\nu_2 \leftarrow \nu_2$ and $\nu_2 + \nu_4 \leftarrow \nu_4$ are "forbidden," as is $\nu_2 \leftarrow 0$. Transitions such as $\nu_3 \leftarrow \nu_4$ are two-quantum transitions.) Intensities are calculated by developing the dipole operator using the same tensorial formalism as for the Hamiltonian [LOETE83].

The calculated hotband spectrum proved to be in good agreement with the transitions measured by FTIR and by our IRDR measurements, although discrepancies at higher J were present (as expected). This augments considerably the data available for the pentad analysis. The pentad parameters are now adjusted to fit three independent sets of rovibrational data: infrared transitions measured near 1000 cm^{-1} and near 2000 cm^{-1}, and Raman transitions near 2000 cm^{-1}. This strategy is currently being followed by G. Millot and G. Pierre, and has allowed the analysis to proceed up to pentad $J = 18$ (at the time of this writing).

A comparison of calculated and observed hotband spectra in a small part of the dyad frequency region is shown in Fig. 2-6. Although the analysis of the pentad is as yet incomplete, the present level of accuracy is adequate for the assignment of transitions used in the collisional energy transfer measurements described in the following chapters. The pentad energies resulting from the analysis are shown in Fig. 2-7. This plot is a good demonstration of the complicated level structure in the pentad. For $J \sim 18$, there is a nearly continuous distribution of rotational levels over a span of about 250 cm^{-1}. Complicated level crossings occur for the pairs $\nu_1/(\nu_2 + \nu_4)$, $2\nu_2/\nu_3$, and $2\nu_4/(\nu_2 + \nu_4)$. In Table 2-2 we list the vibrational parentage of the $J = 11$ levels, evidence of the extensive mixing of the vibrational quantum numbers. The statistical results of the fit are given for the Raman data in Ref. [MILLOT87]. A future publication will include further statistics of the fit to all of the spectroscopic data. A portion of the hotband spectrum, from 960 to 980 cm^{-1}, is listed in Appendix 1.

At this time G. Millot and G. Pierre are refining the spectroscopic parameters to improve the fit for all J values. The results of this analysis, and of similar analyses already completed for $^{12}CH_4$ [PPCP82] and $^{12}CD_4$ [LOLCK85], will allow spectroscopists to assess the validity of the third-order tensorial Hamiltonian as a model of the pentad states. At the highest J values ($J \sim 18$ in $^{13}CD_4$), the deficiency of the Hamiltonian truncated to third order is apparent: calculated transition frequencies are in error by as much as 0.05 cm^{-1}. Many of the transitions can still be assigned, even up to $J = 20$, but a larger Hamiltonian will be required to obtain a satisfactory fit. With this experience in hand, one can then attempt to address the higher polyads. We are also in a position to use the great abundance of spectroscopic information on the various isotopic forms of methane to deduce accurate values of the molecule's structural parameters and the force constants of the vibrational potential function. Currently, the knowledge of the force constants is surprisingly poor for such a simple polyatomic molecule [GRAY79]. Before improvements can be made, however, further theoretical work is needed to clarify the relationship between the deduced rovibrational parameters and the fundamental vibrational potential, especially when the vibrations have strong interactions. Some efforts toward this end have been made recently [ABOU84,LOLCKR85].

Table 2-2. Principal vibrational contributions to pentad levels of $J=11$, F_1 rovibrational symmetry.

Only those contributions $\geq$ 10% are shown. In this table, the $\nu_2+\nu_4$ vibration is abbreviated as "ν_{24}."

n	E (cm^{-1})	Vibrational Contributions				
		$2\nu_4$ (A$_1$,E,F$_2$)				
1	2269.08539	$2\nu_4$(F$_2$) 63%	$2\nu_4$(E) 30%			
2	2269.96265	$2\nu_4$(F$_2$) 62%	$2\nu_4$(E) 30%			
3	2271.94453	$2\nu_4$(F$_2$) 60%	$2\nu_4$(E) 30%			
4	2287.50260	$2\nu_4$(F$_2$) 30%	$2\nu_4$(A$_1$) 28%	$2\nu_4$(E) 27%		
5	2288.89038	$2\nu_4$(A$_1$) 63%	ν_1 15%	$2\nu_4$(E) 11%		
6	2290.34820	$2\nu_4$(A$_1$) 44%	$2\nu_4$(F$_2$) 20%	$2\nu_4$(E) 18%	ν_1 10%	
7	2292.48492	$2\nu_4$(F$_2$) 30%	$2\nu_4$(A$_1$) 29%	$2\nu_4$(E) 28%		
8	2295.84865	$2\nu_4$(A$_1$) 38%	$2\nu_4$(F$_2$) 26%	$2\nu_4$(E) 21%	ν_1 10%	
9	2307.91374	$2\nu_4$(E) 57%	$2\nu_4$(F$_2$) 20%			
10	2309.25307	$2\nu_4$(F$_2$) 64%	$2\nu_4$(E) 24%			
11	2311.74279	$2\nu_4$(F$_2$) 74%	$2\nu_4$(E) 12%			
12	2324.87633	$2\nu_4$(F$_2$) 83%				
13	2327.03748	$2\nu_4$(F$_2$) 61%	$2\nu_4$(E) 20%			
14	2330.10194	$2\nu_4$(E) 46%	$2\nu_4$(F$_2$) 40%			
15	2342.87096	$2\nu_4$(F$_2$) 42%	$2\nu_4$(E) 36%			
16	2351.89135	$2\nu_4$(E) 50%	$2\nu_4$(F$_2$) 37%			
17	2356.29468	$2\nu_4$(E) 51%	$2\nu_4$(F$_2$) 40%			
18	2362.53730	$2\nu_4$(E) 52%	$2\nu_4$(F$_2$) 43%			
		$\nu_2+\nu_4$ (F$_1$,F$_2$) and ν_1 (A$_1$)				
19	2400.51229	ν_{24}(F$_2$) 52%	ν_{24}(F$_1$) 33%			
20	2401.07608	ν_{24}(F$_2$) 49%	ν_{24}(F$_1$) 41%			
21	2401.70339	ν_{24}(F$_2$) 48%	ν_{24}(F$_1$) 34%			
22	2402.29576	ν_{24}(F$_2$) 46%	ν_{24}(F$_1$) 45%			
23	2402.96635	ν_{24}(F$_2$) 50%	ν_{24}(F$_1$) 30%			
24	2411.57018	ν_{24}(F$_2$) 84%				
25	2418.12832	ν_{24}(F$_1$) 44%	ν_1 18%	ν_{24}(F$_2$) 15%		
26	2420.28876	ν_{24}(F$_2$) 57%	ν_{24}(F$_1$) 30%			
27	2424.19622	ν_{24}(F$_2$) 41%	ν_{24}(F$_1$) 33%	ν_1 11%		
28	2425.55025	ν_{24}(F$_2$) 44%	ν_{24}(F$_1$) 35%			
29	2432.94771	ν_{24}(F$_1$) 39%	ν_{24}(F$_2$) 31%	ν_1 12%		
30	2435.59840	ν_{24}(F$_1$) 37%	ν_{24}(F$_2$) 34%	ν_1 14%		
31	2442.57170	ν_{24}(F$_2$) 32%	ν_{24}(F$_1$) 31%	ν_1 22%		
32	2446.91255	ν_{24}(F$_1$) 68%	ν_{24}(F$_2$) 13%			
33	2448.32193	ν_{24}(F$_1$) 49%	ν_{24}(F$_2$) 23%	$2\nu_2$(E) 10%		
34	2449.32551	ν_1 47%	$2\nu_4$(A$_1$) 17%	ν_{24}(F$_1$) 14%	ν_{24}(F$_2$) 13%	
35	2454.10541	ν_1 40%	ν_{24}(F$_1$) 24%	$2\nu_4$(A$_1$) 17%	ν_{24}(F$_2$) 10%	
36	2454.93383	ν_1 32%	ν_{24}(F$_1$) 22%	ν_{24}(F$_2$) 16%	$2\nu_4$(A$_1$) 14%	
37	2456.35578	ν_{24}(F$_2$) 42%	ν_{24}(F$_1$) 21%	ν_1 10%	$2\nu_4$(F$_2$) 10%	
38	2459.29171	ν_{24}(F$_2$) 59%	ν_{24}(F$_1$) 23%	$2\nu_4$(F$_2$) 12%		

Table 2-2 (cont.)

n	E (cm^{-1})	Vibrational Contributions		
		$2\nu_2$ (A$_1$,E)		
39	2533.57311	$2\nu_2$(A$_1$) 50%	$2\nu_2$(E) 47%	
40	2538.35096	$2\nu_2$(E) 46%	$2\nu_2$(A$_1$) 45%	
41	2539.50760	$2\nu_2$(E) 57%	$2\nu_2$(A$_1$) 33%	
42	2540.93732	$2\nu_2$(E) 90%		
43	2543.60780	$2\nu_2$(E) 79%		
44	2545.78305	$2\nu_2$(E) 74%	$2\nu_2$(A$_1$) 10%	
45	2548.02142	$2\nu_2$(A$_1$) 46%	$2\nu_2$(E) 37%	ν_{24}(F$_1$) 12%
46	2552.52004	$2\nu_2$(E) 48%	$2\nu_2$(A$_1$) 29%	ν_{24}(F$_1$) 14%
47	2554.69786	$2\nu_2$(E) 41%	$2\nu_2$(A$_1$) 36%	ν_{24}(F$_1$) 18%
		ν_3 (F$_2$)		
48	2581.60009	ν_3 92%		
49	2581.60802	ν_3 93%		
50	2581.62564	ν_3 93%		
51	2589.57939	ν_3 91%		
52	2589.76854	ν_3 92%		
53	2589.92469	ν_3 93%		
54	2599.52882	ν_3 92%		
55	2599.57295	ν_3 92%		
56	2599.61112	ν_3 93%		

Figure 2-6: Comparison of Calculated and Observed Spectra

Both hotband and fundamental transitions are shown. The middle spectrum is a portion of the FTIR spectrum taken by A. Valentin and L. Henry at 4 Torr and 300 K; units are cm^{-1}. The calculated hotband spectrum is from a preliminary stage of the analysis, up to pentad $J = 14$. (The line assignments for the hotband spectrum are contained in Appendix 1.) Merci à Gérard Pierre.
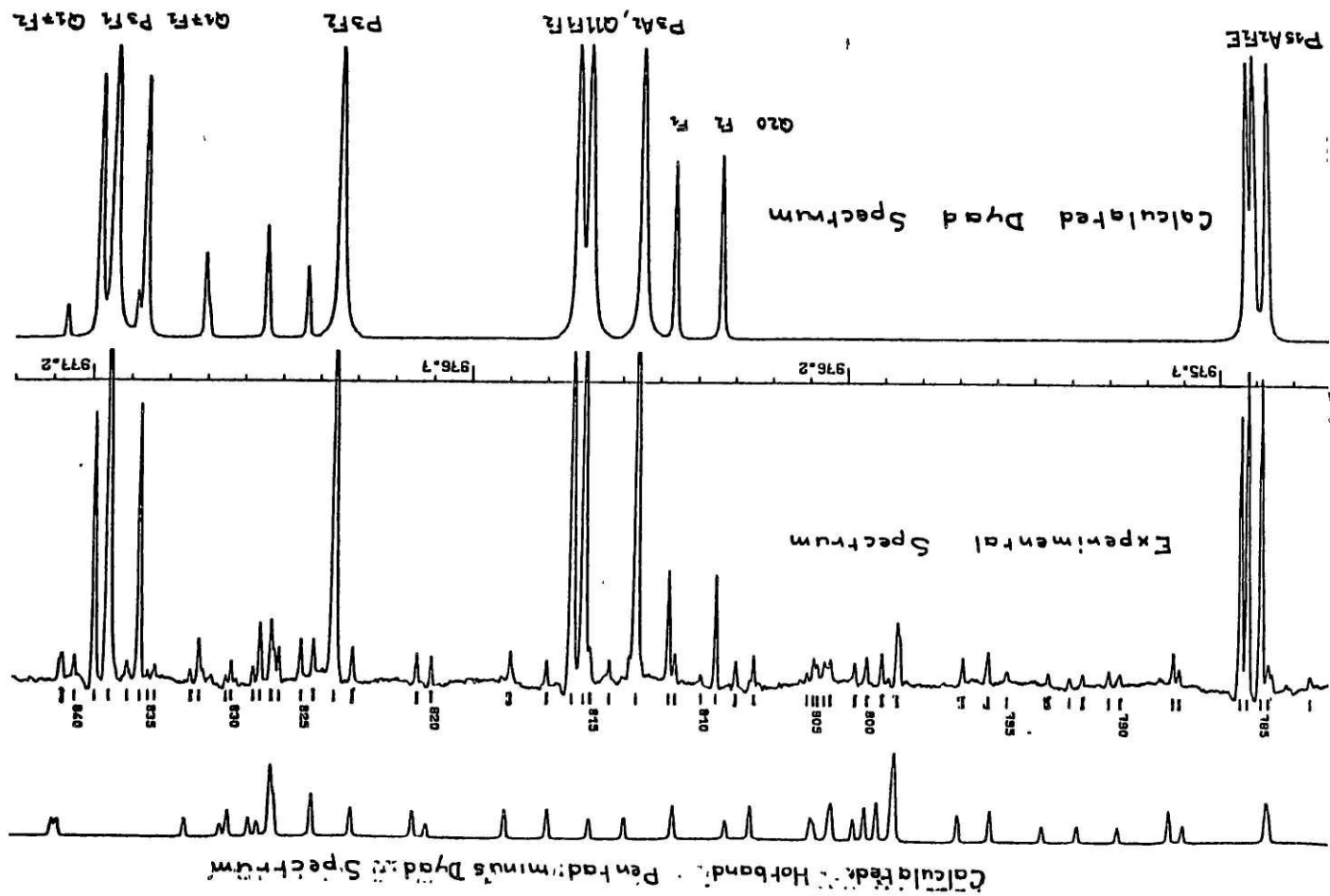
Figure 2-7: Reduced Energy Levels of the Pentad

$E_{red} = E - B_0 J(J+1) - \ldots$, as explained in the text.

E_{red} (cm^{-1})

2250

2200

2150

2100

2050

2000

1950

1900

ν_3 (F_2)

$2\nu_2$ (A_1, E)

ν_1 (A_1)

$\nu_2 + \nu_4$ (F_1, F_2)

$2\nu_4$ (A_1, E, F_2)

0   2   4   6   8   10   12   14   16   18

J→
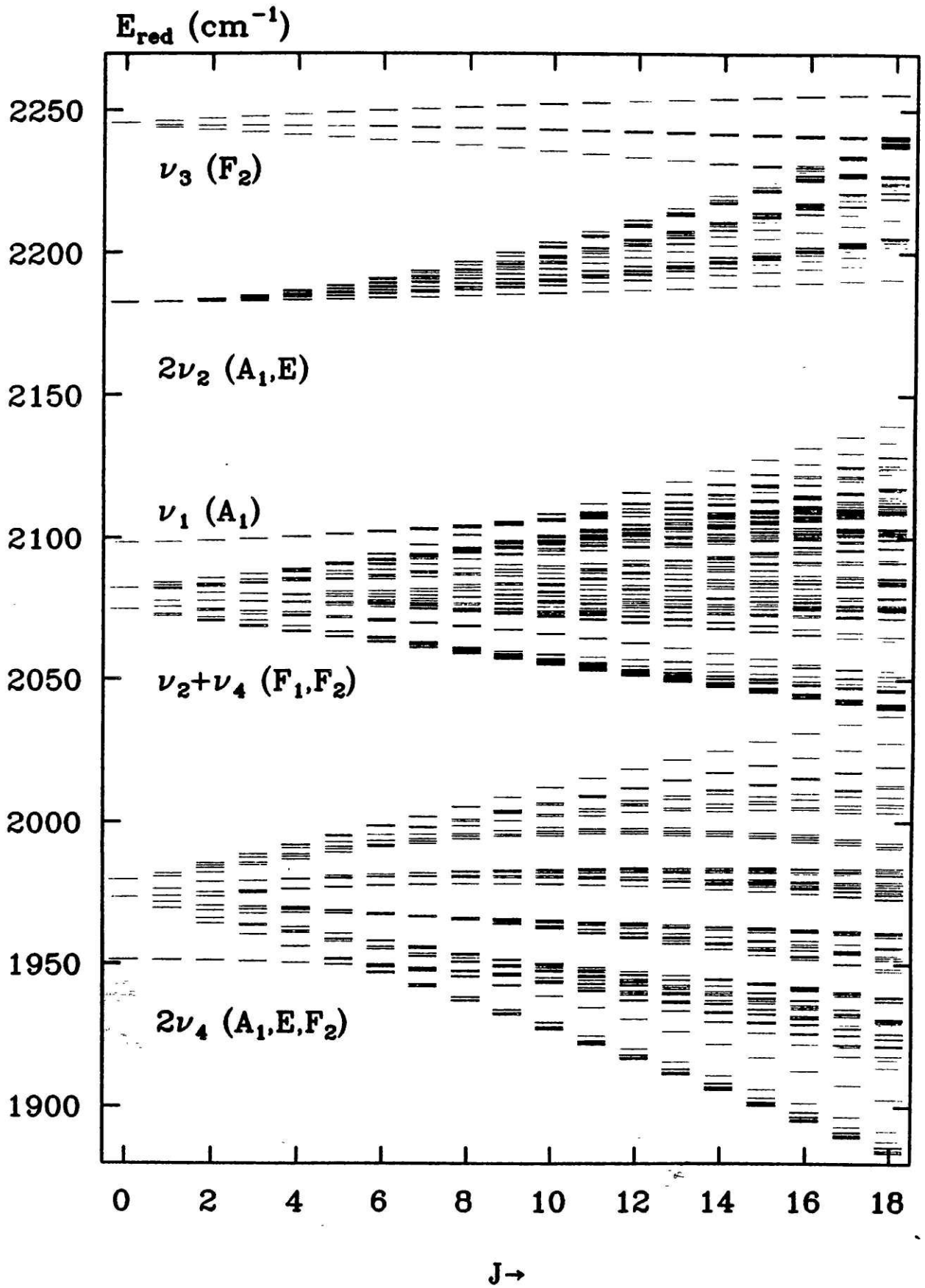
Chapter Three
Collisional Depopulation Rates in $^{13}CD_4$

3.1 Introduction

As a first glimpse into the collisional relaxation behavior of methane, we will discuss measurements of the rate of total depopulation of a rovibrational level. Conceptually, this is perhaps the simplest collisional process: we populate some specific initial level, and the population decays by collisional transfer to a large set of final levels, undistinguished by the experiment. We monitor only the disappearance of molecules from the initial level. The simple rate of total depopulation gives us a useful measure of the cross section for rotationally inelastic collisions, shedding some insight into the nature of the interaction responsible for the change of state. This will lay the groundwork for the more detailed study of the state-to-state processes in Chapter 4. Nearly all of our total depopulation measurements were reported in a Chemical Physics Letter, included in this thesis as Appendix 2. In this chapter, I will add a few experimental details and supplement the discussion of the results.

Total depopulation rates are measured in a three-level double resonance scheme, as shown in Fig. 3-1. A pulse from the pump laser excites molecules to a single rovibrational level over a brief time interval (500 nsec). The upper level of the pumped transition is within the ν_4 vibrational state. The ensuing collisional depopulation of the level is monitored by tuning the weak probe laser to a transition originating in the pumped level, and by following in time the amount of absorption of the probe by the sample. In addition to measuring the depopulation rate, we can measure the rate at which the lower level of the pumped transition is refilled by collisional energy transfer. In this case, the probe is tuned to transition (b) of Fig. 3-1. The decay rate of this double resonance signal yields a measure of the rotational relaxation cross section that is characteristic of the ground vibrational state of methane.

47

$v_4=2$ 11 $F_1{}^{13}$

(a)

974.604 cm^{-1}

12 $F_2{}^5$

$v_4=1$

11 $F_2{}^7$

980.721 cm^{-1}

(b)

942.381 cm^{-1}

CO_2 10P(22)

$v_4=0$ 12 $F_1{}^1$
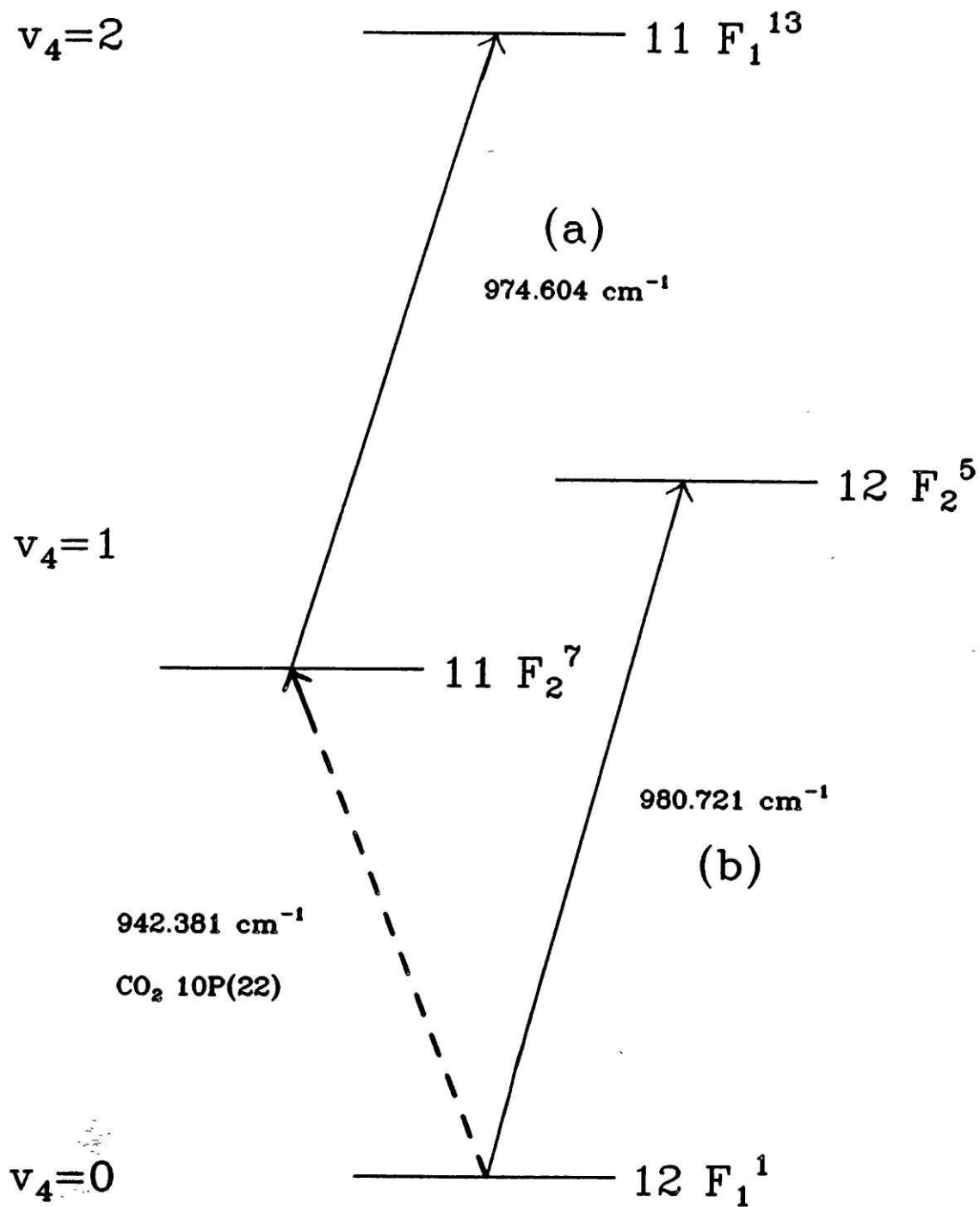
Figure 3-1: Pump-Probe Scheme for Depopulation and Refilling Rate Measurements

Dashed line indicates pumped transition.

In both depopulation and refilling measurements, we expect that *rotational* relaxation is primarily responsible for the observed signal, and that vibrational relaxation makes only a small contribution. This assumption could be justified adequately on the basis of the long history of energy transfer experiments in polyatomic molecules. since they have revealed an almost universal hierarchy of equilibration rates in which $k_{rot} >> k_{vib}$ [YARD80]. But in fact. we are not forced to accept this by fiat. When we examine state-to-state energy transfer in methane in Chapter 4, we will see that there is indeed a separation of time scales for rotational and vibrational relaxation. It is therefore reasonably accurate to call the depopulation rate a "rotational relaxation" rate, and we will do so frequently in the following discussion.

3.2 Experimental

The experimental apparatus used in the depopulation measurements has been described in detail in a previous paper [HARR84]. A number of additional hints were presented in the thesis of D. Harradine [HARRT84]. In this section I will simply outline the experimental details for the sake of completeness of the discussion, and point out new features as appropriate. A schematic drawing of the apparatus is shown in Fig. 3-2.

The pump laser in our setup is a carbon dioxide laser. For the measurements described in this chapter, we used a continuous-discharge, low-pressure (~10 Torr) laser described in detail in Ref. [HARR84]. Pulses are formed by rotating the mirror at one end of the optical cavity; this is done simply by mounting the mirror on the shaft of a D.C.-powered motor that rotates at 150 revolutions/sec. The use of a D.C.-powered motor rather than one powered by line voltage insures that line voltage fluctuations do not affect the speed of the motor. We used a curved mirror (R = 10 m, 1.5" diam.) with a silicon substrate and "enhanced silver" coating for 10.6 μm (Laser Power Optics). Mirrors become scratched after a month or so of high-speed rotation in the air, and must be replaced when warranted by a drop in laser power. Pulses produced by this laser at a repetition rate of 150 pulses/sec have a duration of ~500 nsec (FWHM) and peak power ~3 kW.

Figure 3-2: IRDR Schematic (next page) →

Some features of the drawing apply for the apparatus used for the measurements of Chapter 4. The HgCdTe detector pictured below the CO_2 laser can be used to detect scattered pump-laser light.

CO$_2$ laser

HgCdTe detector

Sample cell

Pol.

Diode laser

HgCdTe detector

Monochromator 0.5 M

50
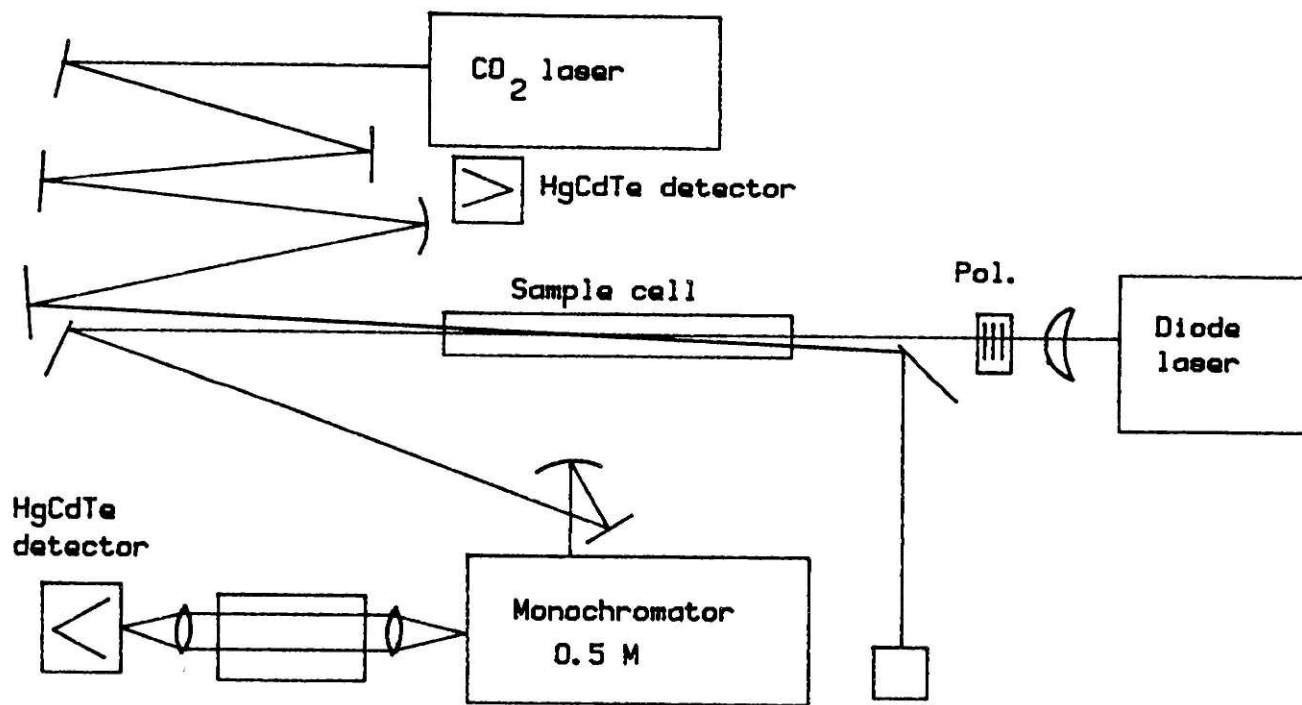
The probe laser is a tunable infrared diode laser that operates at cryogenic temperatures (20-50 K). We use a standard apparatus produced by Laser Analytics (SP5800). Our cold head is of the older type, with an aluminum housing; three vibration-isolation rods support the second stage, on which the diodes are mounted. A number of laser diodes were used for the measurements described throughout this thesis, all of PbSnTe composition, and all of which operated near 10 μm. Most measurements were made with the older-style diodes that have a maximum tuning-current rating of 2 A. (The newer "stripe" diodes have a current maximum of 1 A.) Lasers of this type have output powers of ~0.1 mW in c.w. operation.

The probe laser beam is collimated by a 2 in. focal length lens (f/1) and passed through a polarizer oriented with its axis orthogonal to the polarization axis of the pump laser. This helps to prevent scattered pump-laser light from falling on the diode laser, which is extremely sensitive to such perturbations. The probe beam is focussed near the center of the cell. Here, it crosses the pump-laser beam at a small angle ($<1°$), small enough that the beams are effectively overlapped throughout the 70 cm cell. The probe laser beam is then directed through a ½ meter monochromator (Bausch & Lomb); this isolates a single longitudinal mode of the diode laser output, and filters out scattered radiation from the pump laser. The probe beam is then focussed onto a HgCdTe detector (Santa Barbara Research), cooled to 77 K. The detector element is specially selected for its fast time response (time constant $\tau \simeq 50$ nsec).

We find that the diode laser beam is quite difficult to collimate. At the focal plane, the beam is usually elliptical in shape; sometimes, two or more intensity maxima occur in the beam profile. The effective half-power diameter of the beam is normally 4-5 mm. For this reason, the pump-laser beam is brought to a weak focus in the intersection region to produce a matching spot size.

The detector signal goes directly to a fast amplifier provided by Santa Barbara Research. The amplified signal is sent either to a transient recorder (Biomation 820) or to a boxcar integrator (PAR 160) to capture the transient changes in transmission of the probe beam. When detecting with a boxcar, one can monitor the size of the transient signal as the probe laser is tuned across various spectral features. Double resonance spectra can be collected in this way as a function of the delay time between the pump-laser pulse and the boxcar gate, allowing one to map out the evolution of a set of double resonance signals. Alternatively, we can achieve much better time resolution by fixing the probe laser to a specific spectral feature and collecting the signal waveform (the "decay curve") with the transient recorder. For a single pump laser pulse, the entire transient signal, carried by the c.w. probe laser beam, is obtained over any desired time interval; successive

shots can be averaged until the signal-to-noise ratio is satisfactory. The Biomation 820 transient recorder has a maximum time resolution of 50 nsec between points, and a bandwidth extending to 4 MHz (-3 dB point).

During signal averaging with the transient recorder, the probe laser must be maintained at line center of the probed transition. For the depopulation measurements described below, we do this simply by monitoring the signal detected by the boxcar, and manually tuning the diode laser frequency to optimize the signal. (The diode laser frequency is adjusted by controlling the current passing through the crystal.) On the other hand, we sometimes detect double resonance signals that occur when the probe laser is tuned to a strong absorption transition of the fundamental band (as in the measurements of the "refilling rate" discussed above). In this case, the probe laser frequency can be "locked" to the feature by a standard frequency-modulation technique described in Ref. [HARR84]. Generally, we found that the drift of the diode laser frequency was small, so that by manual correction it was relatively easy to maintain the frequency at the desired value. We should point out, however, that the extent of frequency drift varies markedly among diodes, so the technique described above is not universally applicable.

The sample cell is made from a glass tube 70 cm in length, with an i.d. of 25 mm. The cell is equipped with ZnSe windows, A.R. coated on both sides for 10.6 μm (Two-Six, Inc.). Cell pressure is measured with a capacitance manometer (MKS Baratron, model 227A, 0-10 Torr range) with an accuracy of $\pm 0.15\%$. During the measurements, there was a small amount of outgassing by the manometer, so pressures were accurate only to ± 3 mTorr. Our sample of $^{13}CD_4$ was obtained from Los Alamos National Laboratories. The content of various isotopic species of methane is estimated [MCDOW85] to be 91.2% $^{13}CD_4$, 6.9% $^{12}CD_4$, and 1.8% $^{13}CHD_3$. Methane has a high vapor pressure at the temperature of liquid nitrogen, so we could not purify our sample before use. It was simply released from a glass bulb whose cold finger was cooled to 77 K.

3.2.1 Frequency Instability of the Diode Laser

The most serious experimental difficulty that we encounter is frequency jitter in the diode laser output. I refer here to rapid frequency fluctuations, not the slow frequency drift mentioned above. Frequency jitter is a problem that arises independently of any external perturbations. It is an intrinsic feature of the diode laser apparatus, which includes the cryogenic refrigerator assembly as well as the diode element itself. It poses a serious obstacle to many kinds of spectroscopic research with diode lasers, and therefore merits careful consideration.

Diode lasers are maintained at cryogenic temperatures by a closed-cycle compressed-helium refrigerator; a standard apparatus made by CTI Cryogenics (Model 21SC) is normally used. The compressed helium is circulated through the cold head by means of a piston operating at 3 cycles/sec. Since the piston is situated very close to the diodes, traumatic vibrations caused by the piston action are transmitted to the diode crystal and sometimes produce a sinusoidal modulation of the laser output frequency. This effect was first publicized by Melandrone *et al*. [MELAN85], and it is an inescapable feature of all Laser Analytics cold heads, judging from communication that the author has had with other experimenters. In the Melandrone paper, the authors observe the frequency of the modulation waveform to be "a few kHz," although they state that it varies among different diodes and different operating conditions. In our diodes, we have observed much higher modulation frequencies. Figure 3-3 shows a transient perturbation with a modulation frequency of ~160 kHz. Note also the regular, sinusoidal appearance of the transient. We detected this by setting the diode laser to one side of a strong absorption feature (with width $\Delta \nu \sim 100$ MHz), and detecting the transmission through the sample. The steep slope of the feature translates laser frequency modulation into intensity oscillations of the detected signal. The amplitude of the modulation waveform, i.e. the extent of the frequency jitter, is also highly variable for different devices. For the diode used to produce Fig. 3-3, the jitter is perhaps one-half of the laser linewidth, where $\Delta \nu_{laser} \simeq 30$ MHz. This diode is among the quietest performers we have seen. In the worst cases, the jitter can be several times the intrinsic laser linewidth, especially if the diode has a high "tuning rate" (output frequency change versus tuning-current change, with units of MHz/mA).

Frequency modulation induced by mechanical vibrations causes a deterioration of the signal-to-noise ratio of the experiment in two ways. First, the frequency components of the intensity oscillations exemplified in Fig. 3-3 interfere with the frequency spectrum of the double resonance signals, which have a large bandwidth (extending from a few Hz to at least 10 MHz). We should note that the transient intensity oscillations are many times larger than the double resonance signals that we wish to extract. Although the transient perturbations have a regular sinusoidal shape, the amplitude, phase, and frequency of the oscillations vary randomly from one piston cycle to the next, so that the oscillations cannot simply be subtracted out. Signal levels are also reduced due to the laser being off line center for a significant portion of the time.

Vibration–induced FM

$\nu = 160$ kHz

detuned from absorption line
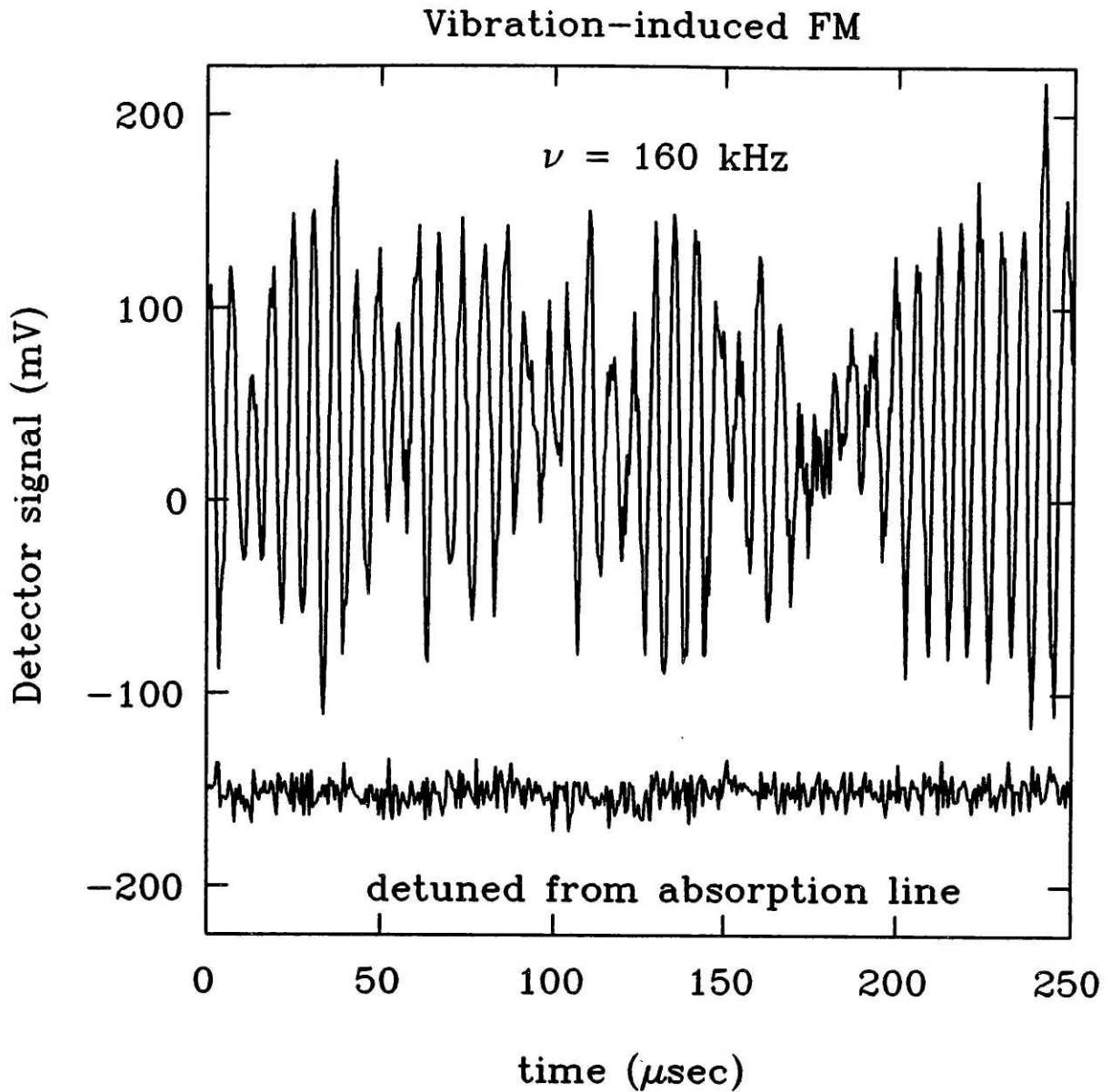
Figure 3-3: Transient Oscillations Due to Frequency Modulation of the Diode Laser
The upper trace was taken with the diode laser tuned to one side of an absorption line. The bottom trace shows the amplitude stability of the laser: it is detuned from the line so that FM does not show up. This demonstrates that the top trace is caused by frequency, not amplitude, fluctuations in the diode laser output. Bottom curve displaced for clarity.

Clearly, improvements in the design of the cold head and the refrigeration system are necessary. Until such advances are made, the experimenter's only recourse is to examine each new diode very carefully, and to purchase only those diodes in which vibration-induced frequency jitter is at a tolerable level. This usually entails a tedious and exhaustive search of the manufacturer's stock, and invariably provokes a considerable amount of consternation on the part of the salesman.

3.3 Data Reduction

Decay curves were recorded for a range of $^{13}CD_4$ pressures between 25 and 200 mTorr. (Examples are shown in Appendix 2.) An exponential function was fitted to the falling portion of the curve (after the end of the pump-laser pulse) by a non-linear least-squares procedure employing the Marquardt algorithm [BEVIN69]. A plot of decay rate versus pressure was found to be linear, and its slope gives the decay rate constant k (in units of μsec^{-1} $Torr^{-1}$). To obtain the binary rate constants $k(^{13}CD_4 - M)$, we took a set of curves at a fixed pressure of $^{13}CD_4$ and various pressures of the collision partner M, using the slope of the plot of rate versus p_M. Rate constants are converted from μsec^{-1} $Torr^{-1}$ to cm^3 $molecule^{-1}$ sec^{-1} (using the ideal gas law). An effective cross section σ_{rot} can then be deduced from the measured rate constant k by means of the well-known relation [YARD80]:

$$\sigma_{rot} = \frac{k}{\overline{v}_{rel}} = k \left(\frac{\pi\mu}{8k_BT}\right)^{\frac{1}{2}}$$

where μ is the reduced mass of the colliding pair, so that $\overline{v}_{rel}$ is the mean relative velocity. The cross section, in Å^2, can now be compared with the collision cross section estimated by kinetic theory [HIRS54]:

$$\sigma_{LJ} = \pi d^2 \cdot \Omega^{(2,2)*}$$

where $\Omega^{(2,2)*}$ is the collision-integral correction, determined by the attractive well depth ε of the Lennard-Jones isotropic interaction potential. The well depth and the Lennard-Jones diameter d are deduced from measurements of bulk properties of the gas. The Lennard-Jones cross section is a useful "yardstick" against which to compare the rotational relaxation cross section. For collisions between unlike species A and M, we use well depths and diameters determined by the usual combination rules:

$$\varepsilon_{AM} = (\varepsilon_A \varepsilon_M)^{1/2}$$
$$d_{AM} = \frac{1}{2}(d_A + d_M).$$

This procedure has been used to interpret a wide variety of rotational and vibrational relaxation phenomena. The validity of the combination rules for ε_{AM} and d_{AM} is supported by the

Parmenter-Tang theory for collision efficiencies for vibrational relaxation in polyatomic molecules [PARM78]. A recent application of this approach to vibrational relaxation rates in *para*-difluorobenzene has shown that the collision efficiencies can be successfully rationalized in terms of the Lennard-Jones well depths [THOM87].

Since the publication of Appendix 2, we have measured one additional cross section, $\sigma(^{13}CD_4-^{12}CD_4)$. We also remeasured the cross sections for collisions with Kr and Xe, and found slightly smaller values than reported in Appendix 2. A revised list of cross sections is presented in Table 3-1.

Table 3-1. Depopulation and Refilling Rates for $^{13}CD_4$.

Coll. partner	$(p\tau)^{-1}$ μsec^{-1} Torr^{-1}	$k \times 10^{10}$ cm^{3}molec^{-1}sec^{-1}	σ_{rot} Å^2	σ_{LJ} Å^2	
$v_4=0$, $J=12$, F_1^1 (refilling rates)					
$^{13}CD_4$	10.5(2)	3.26	41.9(8)	49.7	
He	4.6(1)	1.4	10.2(2)	21.5	
Ne	4.7(7)	1.5	19(3)	31.6	
Ar	5.45(30)	1.7	25(1.4)	44.7	
Kr	6.1(6)	1.9	31(3)	50.9	
Xe	6.4(4)	2.0	34(2)	59.0	
CH_2F_2	6.5(3)	2.0	31(1.4)	~63	
$v_4=1$, $J=11$, F_2^7 (depop. rates)					
$^{13}CD_4$	16.6(3)	5.17	66.5(1.2)		@300K
$^{13}CD_4$	25.4(1.4)	3.95	72(4)		@150K
$^{12}CD_4$	15.8(1.6)	4.84	62(6)		
He	6.5(3)	2.0	14.7(7)		
Ne	7.2(6)	2.2	28(2.5)		
Ar	8.3(7)	2.6	38(3)		
Kr	15.7(7)	4.88	66(4)		
Xe	16.2(7)	5.03	64.2(3.4)		
CH_2F_2	9.9(2)	3.1	48(2)		

3.4 Discussion

The measured relaxation cross sections are displayed in Fig. 3-4. We plot σ_{rot} versus $\mu^{1/2}$ only because this provides a convenient scale, not because of any anticipated functional dependence on the reduced mass. We also plot the ratio σ_{rot}/σ_{LJ}, which one might take to be a measure of the effectiveness of an encounter at the Lennard-Jones distance of approach. (Many authors call σ_{rot}/σ_{LJ} the "collision efficiency" or "probability." The difficulty with that terminology is that the probability, so defined, can paradoxically be greater than unity.) We can see that $^{13}CD_4$-M relaxation cross sections are all on the order of the Lennard-Jones cross section. (The deviations are at most a factor of two.) This suggests that the *isotropic* Lennard-Jones interaction potential provides a rough measure of the range of the *anisotropic* interaction that is responsible for rotationally inelastic events.

For relaxation by self-collisions, the cross section is higher than for collisions with atoms of roughly the same mass (compare $\sigma[^{13}CD_4$-$^{13}CD_4]$ with $\sigma[^{13}CD_4$-Ne]). Part of the reason for this is the deeper attractive well (137 K) in the methane-methane interaction, as compared with the methane-neon interaction (70 K) [HIRS54]. But even when this is taken into account (by comparing with σ_{LJ}), the self-relaxation cross section appears to be quite large (~35% larger than σ_{LJ} for relaxation in ν_4). As stated in Appendix 2, we feel that this reflects the presence of an additional relaxation channel available in self-collisions. Exchanges of rotational quanta between the collision partners might make a significant contribution to the relaxation rate. We can symbolize this as follows:

$$^{13}CD_4(\nu_4, J_1) + {}^{13}CD_4(0, J_2) \Rightarrow {}^{13}CD_4(\nu_4, J_1'') + {}^{13}CD_4(0, J_2'') + \Delta E_{trans}$$

A sensible name for this event is "intermolecular R-R" energy transfer. Such processes could occur with small changes in total rotational energy:

$$J_1'' - J_1 \simeq J_2 - J_2'', \quad \text{for } J_1 \simeq J_2.$$

(If the J values are substantially different, then a rotational energy match will occur with $\Delta J_1 \neq \Delta J_2$; in this case, the orbital angular momentum L of the collision can change to make up for the net change in $J_1 + J_2$.) If ΔE_{trans} is small, there is a "rotational resonance" in the collision; the exchange might occur with high probability [OKA73]. Collisions with $^{12}CD_4$ would have a similarly "enhanced" cross section, since the rotational level structures of $^{13}CD_4$ and $^{12}CD_4$ are nearly identical; this may be why $\sigma(^{13}CD_4$-$^{12}CD_4)$ is close to the self-relaxation cross section. For methane-neon collisions, on the other hand, intermolecular R-R processes are not applicable. Rotational relaxation in this case must be accompanied by changes in translational energy.

The value of σ_{tot} for the level $|\nu_4, J=11, F_2^7\rangle$ for self-collisions is ~35% larger than the Lennard-Jones cross section. The implications of this observation for the nature of the interaction between methane molecules will be explored fully in Chapter 5.

Figure 3-4 (next page): Rotational Relaxation Cross Sections →
Triangles: Depopulation Cross Sections
Circles: Refilling Cross Sections
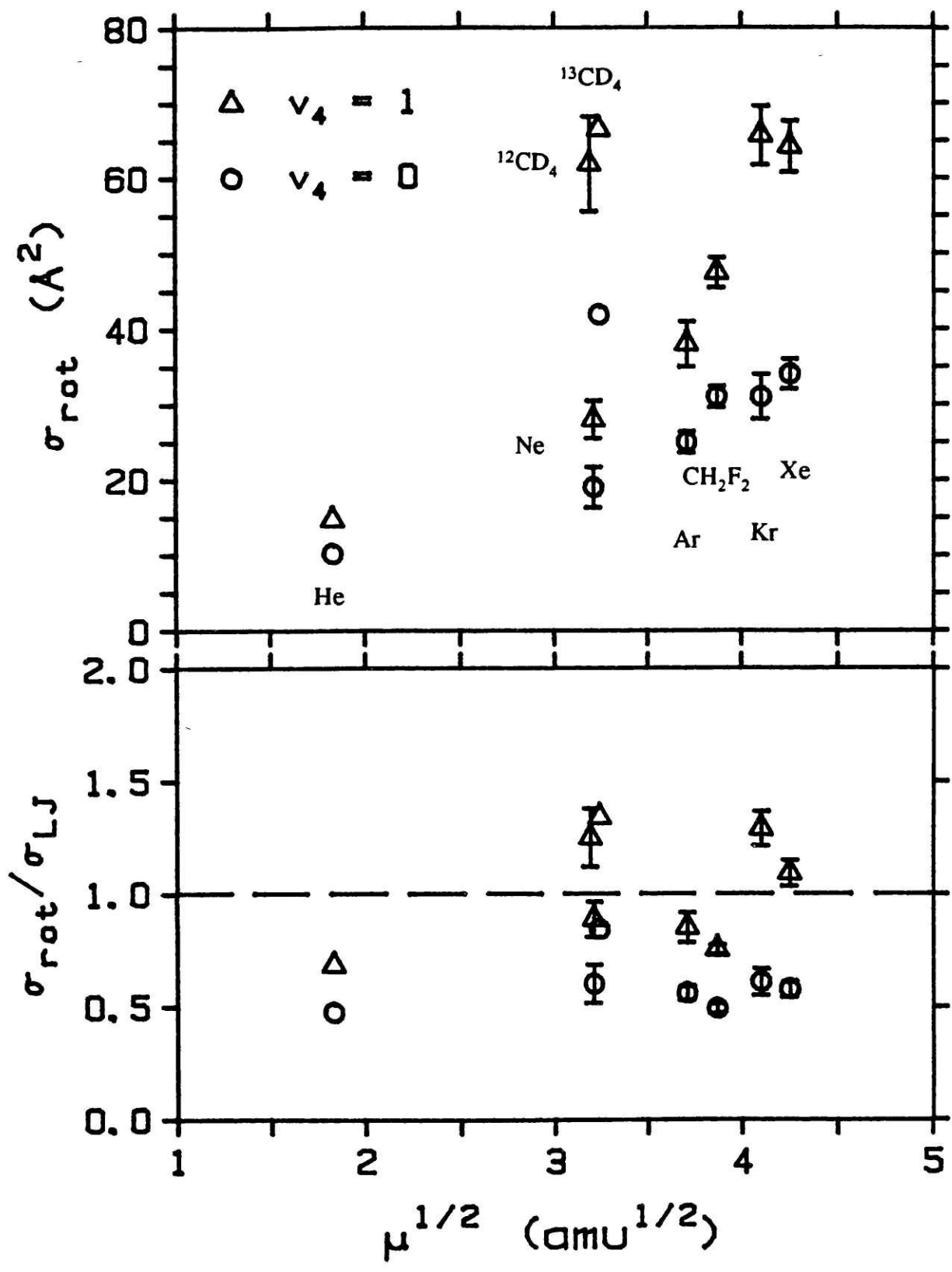
Chapter Four
State-to-State Energy Transfer

4.1 Introduction

In this chapter we will discuss the results of "four-level" double resonance measurements, in which both levels of the probed transition are different from the levels of the pumped transition. Double resonance signals in this configuration correspond to a net transfer of population from the pumped level to the probed level, providing us with the means of obtaining rate constants for energy transfer on a state-to-state basis. These measurements represent an extension of the depopulation measurements of Chapter 3 to the next finer level of detail. They are essentially the first measurements of the detailed collisional pathways among the fine-structure rotational levels (J, C^n) of a spherical-top molecule. (In the earlier IRDR measurements on SF_6, the fine-structure levels were only partially resolved.) We will see in this chapter that the collisional pathways are remarkably selective when viewed at this new level of detail.

We will examine results only for "excited-state four-level" double resonance signals, in which we pump a transition of the fundamental while probing a transition of the hotband (cf. Fig. 1-1). These signals are associated with relaxation (a) within the ν_4 vibrational state, and (b) to the ν_2 state by V-V transfer. It is possible to monitor rotational relaxation among the levels of the ground vibrational state by means of "ground-state four-level" double resonance signals (pump a fundamental transition, probe a different fundamental transition). But a difficulty arises in that pump-probe scheme, namely that double resonance signals are affected by population transfer in both the upper and lower levels of the probed transition. The extraction of state-to-state energy transfer rate constants is then a more difficult problem, which we did not attempt to analyze.

Before describing our results for state-to-state energy transfer in the $^{13}CD_4$ dyad (ν_2 and ν_4) levels, we need to review a few experimental limitations. Since we probe transitions of the hotband (pentad ← dyad), we should consider the overall appearance of the spectrum. Transitions in the hotband will be mainly of the type $\Delta \nu_4 = +1$, as we explained in Chapter 2. In Fig. 4-1 we indicate the positions of rovibrational transitions in these bands for rotational quantum numbers $0 \leq J'' \leq 12$. We see here that the $2\nu_4 \leftarrow \nu_4$ spectrum, which will be used to monitor purely rotational relaxation within ν_4, contains overlapping P, Q, and R branches. The transitions are distributed within a range 100 cm^{-1} wide. The $\nu_2 + \nu_4 \leftarrow \nu_2$ transitions are dispersed throughout a range of 80 cm^{-1}.
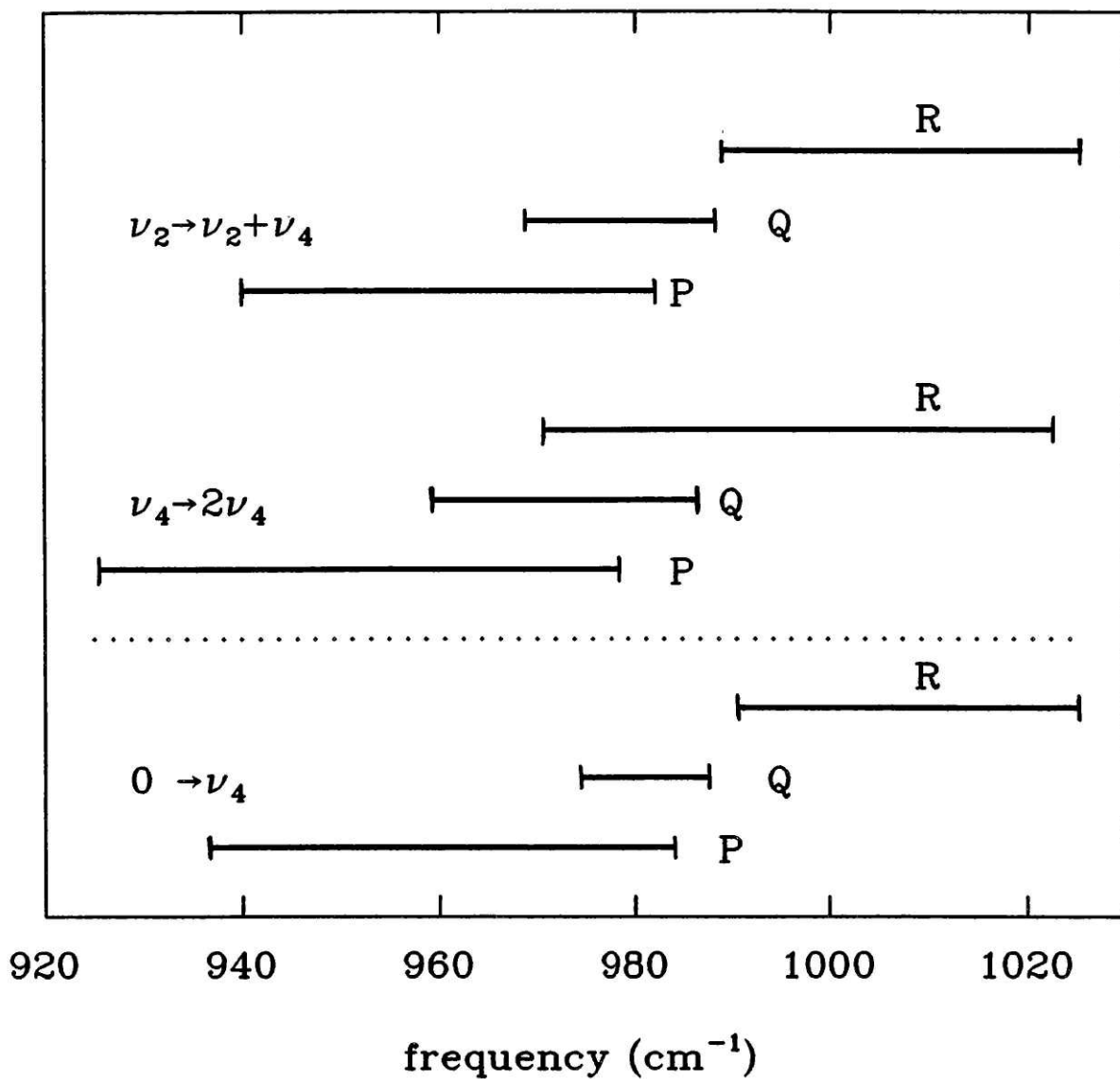
Figure 4-1: Positions of Lines of J = 0 to 12 in Fundamental and Hotband Spectra
Only the "allowed" transitions are included, for $J'' \leq 12$.

Diode lasers possess a number of desirable characteristics for use as probe lasers, but one serious limitation that must be reckoned with is restricted tunability. Although they are continuously tunable over short scans of typically $0.5-3$ cm^{-1} by current tuning through a "mode," the various modes obtainable by temperature adjustment generally do not adjoin one another in frequency. There are gaps of typically $0.5-10$ cm^{-1} between the modes available in a given diode. Individual diodes generally emit over a 100 cm^{-1} range, but because of these gaps, they generally cover only $20-80\%$ of the range. The degree of coverage varies, but has some correlation with laser linewidth (and tuning rate): narrow-linewidth lasers usually have poor coverage. In addition, we should mention that the output power varies with the diode mode by a factor of 10 or more. In many cases, the output power is sufficient to record an absorption spectrum, but too low to recover the weak transient absorption signals in double resonance. We found that among those modes with suitable tuning characteristics, only about 50% are strong enough to obtain good signal-to-noise ratios for IRDR decay curves in methane.

Since these rather serious limitations are inherent features of the diode laser capabilities, a single laser can be used to record signals in only small portions of the 100 cm^{-1} range encompassed by the hotbands shown in Fig. 4-1. Even though we used four different diode lasers to collect the data described in this chapter, we were able to monitor only a fraction ($\sim 30\%$) of the possible transitions. Therefore, it was not possible to use the apparatus to examine systematically every important energy transfer pathway. This would require a considerable investment in diode lasers. Instead, we made a survey of some of the important pathways that we hope gives a reasonably complete picture of the relaxation behavior. Table 4-1 shows a list of transitions that we were able to monitor for the state-to-state studies.

A second important experimental limitation concerns the choice of $^{13}CD_4$ transitions to be pumped. As is well known, the CO_2 laser can only be discretely tuned between available emission lines (rovibrational lines of a combination band in the CO_2 molecule) [STEIN74]. We can pump only those molecular transitions that lie near one of these frequencies. A list of good coincidences is shown in Table 4-2. (A more complete list of these, including coincidences with larger detunings and with laser lines of isotopically substituted CO_2, is contained in Ref. [PIERRE87].) While we were able to obtain IRDR signals for a few of these pump transitions, the bulk of our work was done with the first one listed, which gives rise to the strongest signals. For all of the probe transitions listed in Table 4-1, the initially excited level is therefore $(\nu_4, J=11, F_2^7)$. The population decay curves resulting from this scheme will be the subject of the remainder of this chapter. Our state-to-state relaxation results for other pump-transition schemes will not be discussed in detail.

Table 4-1. Hotband probe transitions monitored for state-to-state measurements. Pumped level: $J = 11$, F_2^7 (F^+ sublevel of ν_4); $E = 1352.43$ cm^{-1}.

J	n" C" n	ν_{cal} (cm^{-1})	Int (arb)	O-C (mK)	Sub lev	ΔE (cm^{-1})	ΔJ	$\Delta (R\text{-}J)$	Comment
Q(11)	7 F$_2$ 13	974.60397	2.31	1.23	F$^+$				] (pumped
Q(11)	7 F$_2$ 14	977.66844	0.45		F$^+$				] level)
Q(14)	3 F$_2$ 5	974.58229	1.06	1.11	F$^-$	154.50	3	-2	
R(13)	10 F$_2$ 11	1020.35785	1.19	-5.05	F$^+$	134.08	2	0	
Q(11)	10 F$_2$ 26	977.84803	1.49	-0.73	ν_2	90.01	0		
Q(12)	8 F$_2$ 14	977.44248	1.70	-0.28	F$^+$	62.41	1	0	] princ
R(12)	8 F$_2$ 10	1009.52761	1.51	-6.81	F$^+$	62.41	1	0	
Q(12)	8 F$_1$ 15	979.17221	1.85	-1.51	F$^+$	61.89	1	0	] weak
R(12)	8 F$_1$ 9	1009.99582	1.57	-6.02	F$^+$	61.89	1	0	]
R(12)	7 F$_1$ 8	1009.96975	1.73	-2.85	F$^+$	58.38	1	0	
Q(12)	6 F$_2$ 11	977.37058	4.26	6.02	F^0	44.25	1	-1	]
R(12)	6 F$_2$ 7	1020.89149	2.13	1.11	F^0	44.25	1	-1	]
Q(12)	6 F$_1$ 12	977.36355	4.13	3.65	F^0	43.78	1	-1	
Q(12)	5 F$_1$ 11	976.90361	3.74	5.99	F^0	41.71	1	-1	]
R(12)	5 F$_1$ 6	1021.02122	2.14	1.08	F^0	41.71	1	-1	]
R(12)	5 F$_2$ 5	1021.04921	2.81	1.09	F^0	38.34	1	-1	
R(12)	4 F$_1$ 4	1021.30950	2.78	0.10	F^0	38.21	1	-1	
Q(12)	4 F$_2$ 4	964.76195	3.33	-15.95	F^0	32.11	1	-1	
R(12)	3 F$_2$ 3	1022.29342	6.17	5.38	F$^-$	19.13	1	-2	
R(12)	3 F$_1$ 3	1022.30357	6.19	4.97	F$^-$	19.11	1	-2	
R(12)	2 F$_1$ 2	1021.11312	6.41	4.38	F$^-$	17.79	1	-2	
R(12)	2 F$_2$ 2	1020.63594	6.51	4.36	F$^-$	17.26	1	-2	
R(12)	1 F$_1$ 1	1020.47545	6.60	0.15	F$^-$	16.91	1	-2	
R(12)	1 F$_2$ 1	1020.29025	6.63	0.65	F$^-$	16.72	1	-2	
Q(11)	8 F$_1$ 13	978.54014	0.79		F$^+$	-1.92	0	0	weak
R(11)	7 F$_1$ 7	1006.61968	1.78	-0.58	F$^+$	-4.86	0	0	princ
R(11)	6 F$_2$ 7	1006.45804	1.64	-0.04	F$^+$	-5.25	0	0	(princ?)
Q(11)	5 F$_2$ 11	977.77904	5.26	4.06	F^0	-18.47	0	-1	] princ
R(11)	5 F$_2$ 6	1018.65304	2.57	2.66	F^0	-18.47	0	-1	]
Q(11)	4 F$_2$ 10	977.48371	4.68	4.59	F^0	-20.66	0	-1	
Q(11)	4 F$_1$ 5	965.24587	3.72	-9.37	F^0	-28.85	0	-1	
Q(11)	3 F$_2$ 9	984.34593	2.15	-2.01	F^0	-28.87	0	-1	] weak
Q(11)	3 F$_2$ 5	965.32257	3.81	-9.67	F^0	-28.87	0	-1	] weak
R(11)	2 F$_1$ 2	1018.42318	7.97	3.42	F$^-$	-42.72	0	-2	
R(11)	2 F$_2$ 2	1018.37011	7.98	2.19	F$^-$	-42.84	0	-2	

Table 4-1 (cont.)

J	n"	C"	n	ν_{cal} (cm^{-1})	Int (arb)	O-C (mK)	Sub lev	ΔE (cm^{-1})	ΔJ	$\Delta (R-J)$	Comment
Q(10)	5	F_1	10	978.17549	6.24	2.31	F^0	-76.12	-1	-1	
Q(10)	5	F_2	9	978.40438	5.72	0.22	F^0	-77.14	-1	-1	] weak
R(10)	5	F_2	6	1015.05516	1.77	-0.56	F^0	-77.14	-1	-1	
Q(10)	4	F_2	8	979.19617	4.60	-0.57	F^0	-79.66	-1	-1	}
R(10)	4	F_2	4	1014.73364	3.25	1.26	F^0	-79.66	-1	-1	
R(10)	1	F_2	1	1015.29075	9.79	-0.05	F^-	-98.64	-1	-2	
R(10)	1	F_1	1	1015.21046	9.84	-0.26	F^-	-98.74	-1	-2	
Q(7)	7	F_1	15	977.32434	3.00	-0.64	ν_2	-112.26	-4		
Q(7)	6	F_2	16	976.96157	3.05	3.83	ν_2	-112.31	-4		
P(9)	6	F_1	12	950.76819	6.91	0.01	F^+	-112.75	-2	0	princ
Q(9)	7	F_2	11	977.77491	2.50	0.39	F^+	-113.14	-2	0	
R(9)	5	F_1	5	998.40362	2.76	-0.22	F^+	-116.33	-2	0	
Q(9)	5	F_2	10	978.84012	6.52	-0.02	F^0	-129.28	-2	-1	
Q(9)	4	F_2	6	964.60759	1.60	0.31	F^0	-131.26	-2	-1	
R(6)	8	F_2	14	1002.53254	3.58	-0.94	ν_2	-146.25	-5		
Q(8)	6	F_1	9	974.65977	4.52	-0.77	F^+	-159.61	-3	0	princ
P(8)	6	F_2	11	954.38990	7.74	0.40	F^+	-161.65	-3	0	
Q(8)	2	F_1	3	974.87400	2.19	1.30	F^-	-192.54	-3	-2	
R(8)	1	F_1	1	1010.08213	12.69	-0.33	F^-	-193.27	-3	-2	
R(8)	1	F_2	1	1009.87256	12.84	-0.66	F^-	-193.52	-3	-2	
R(7)	5	F_2	6	1005.57337	3.10	-2.37	F^+	-203.34	-4	0	weak
Q(7)	3	F_2	4	961.50620	1.92	1.30	F^0	-217.86	-4	-1	
Q(7)	2	F_2	3	965.20985	4.05	0.05	F^0	-222.00	-4	-1	]
R(7)	2	F_2	2	1004.61252	3.77	0.68	F^0	-222.00	-4	-1	
Q(6)	5	F_2	6	977.46994	5.60	-0.14	F^+	-241.81	-5	0	princ
Q(6)	5	F_1	7	977.51503	5.20	-0.33	F^+	-242.00	-5	0	
P(6)	4	F_1	7	961.45972	8.55	0.98	F^+	-243.75	-5	0	
Q(6)	4	F_2	7	984.16655	6.22	-0.65	F^+	-244.61	-5	0	weak
R(6)	3	F_2	5	1005.52337	7.61	0.03	F^0	-254.91	-5	-1	
R(6)	3	F_1	5	1005.50189	7.54	-0.09	F^0	-255.30	-5	-1	
Q(6)	2	F_1	3	964.84400	3.19	0.50	F^0	-257.54	-5	-1	
R(6)	1	F_2	1	1004.36908	14.39	-0.88	F^-	-267.48	-5	-2	
P(5)	4	F_2	6	964.76357	8.20	0.93	F^+	-276.97	-6	0	]
R(5)	4	F_2	5	1002.21778	2.56	-0.18	F^+	-276.97	-6	0	
R(5)	3	F_2	4	1002.47391	7.95	-0.21	F^0	-286.26	-6	-1	

Table 4-1 (cont.)

J	n"	C"	n	ν_{cal} (cm^{-1})	Int (arb)	O-C (mK)	Sub lev	ΔE (cm^{-1})	ΔJ	$\Delta (R-J)$	Comment
R(4)	4	F_2	6	998.48949	3.11	-0.49	F^+	-303.16	-7	0	
R(4)	2	F_2	4	998.42235	7.70	-0.55	F^0	-313.60	-7	-1	
R(4)	1	F_2	3	999.00594	12.71	-0.74	F^-	-320.54	-7	-2	
R(4)	1	F_1	2	998.76419	13.22	-0.79	F^-	-320.64	-7	-2	
R(3)	3	F_1	1	977.57541	2.56	-0.11	F^+	-327.00	-8	0	

Table notes

Transition notation: J, n", and C" are the quantum labels of the lower (dyad) level; n is for the upper level. Hence, the notation Q(11) 7 F_2 13 designates the transition (ν_4, J=11, F_2^7) → ($2\nu_4$, J=11, F_1^{13}).

ν_{cal}: the transition frequency calculated in the analysis, in units of cm^{-1}.

Int: the calculated intensity in arbitrary units.

O-C: the residual in the observed frequency minus the calculated frequency, in units of mK (10^{-3} cm^{-1}). The observed frequencies are from the FTIR spectrum taken by A. Valentin and L. Henry at 4 Torr.

Sublev: the Coriolis sublevel (F^+, F^0, or F^-) of the lower level of the transition. The flag "ν_2" means that the lower level is in the ν_2 vibration. All of the transitions marked "ν_2" are of the type $\nu_2+\nu_4\leftarrow\nu_2$.

ΔE: the difference in energy between the probed dyad level and the pumped level. $E_{probe} - E_{pump}$, in cm^{-1}. $E_{pump} = 1352.43$ cm^{-1}.

ΔJ: $J_{probe} - J_{pump}$.

$\Delta(R-J)$: the quantity $(R - J)_{probe} - (R - J)_{pump}$.

Comments: "weak" means that the probe laser power was too weak to observe a signal with good S/N, but where we tried anyway. "princ" means that the probed level is one of the principal relaxation channels from the pumped level (see text).

Table 4-2. $^{13}CD_4$ Transitions in Coincidence with CO_2 Laser Lines.

All transitions but the one indicated are in the ν_4 fundamental. Transition notation is explained in Notes of Table 4-1. CO_2 lines are in the 10.6 μm branch of $^{12}C^{16}O_2$.

Transition (J") n"C" → n'			ν_{cal} (cm^{-1})	Int. (arb)	CO_2 line	$\nu_L-\nu_{cal}$ (MHz)	DR seen?	
P(12)	1 F_1	7	942.3810	496.2	P(22)	68	Y	
Q(17)	2 F_1	3	947.7369	5.0	P(16)	152		(weak)
Q(17)	1 F_2	4	947.7375	4.8		133		(weak)
Q(8)	0 F_1	2	970.5451	11.1	R(12)	65	Y	(forbidden)
Q(10)	0 A_2	2	978.4678	685.4	R(24)	133	Y	
Q(21)	3 F_1	9	978.4680	17.5		94		(weak)
Q(22)	1 F_1	11	983.2522	1.5	R(32)	2		(weak)
Q(12)	0 F_1	6	986.5735	589.7	R(38)	-183		(large Δ)
R(5)	4 F_2	2	984.3825	2.8	R(34)	21	Y	$2\nu_4{\leftarrow}\nu_4$ transition

4.1.1 Nuclear Spin Restrictions on Collisional Energy Transfer

It is well known that the nuclear spin state of a molecule is not easily changed by collision, in contrast to the facile changes of rovibrational state. In determining the important channels for relaxation from a particular pumped rovibrational level in methane, we need to bear in mind the restrictions imposed by nuclear spin statistics. A rovibrational level of a particular symmetry species in the T_d group is associated with a characteristic nuclear spin function (or functions). Different levels have well-known nuclear spin statistical weights [HERZ45]. A particularly enlightening discussion of these was given by Hougen [HOUG76]. Table 4-3 is reproduced from his paper, showing the statistical weights in both CH_4 and CD_4. We see that in CH_4, each of the three nuclear spin species (I = 0, 1, 2) is identified with one of the rovibrational species A, E, F. Hence, we have the collisional selection rules on the *rovibrational species*:

$$A \leftrightarrow A, \; E \leftrightarrow E, \; F \leftrightarrow F. \qquad (4.1)$$

All other transitions are strictly forbidden. (The selection rules are relaxed when intramolecular effects such as spin-rotation interactions cause mixing of the symmetry species C. These interactions are negligible for methane, though, and will be disregarded throughout the discussion.) It is interesting to note that transitions such as $F_1 \rightarrow F_2$ cause a change of parity of the molecule, since the overall species changes, $A_2 \rightarrow A_1$. Likewise, parity remains the same in the transition $F_1 \rightarrow F_1$.

66

Table 4-3. Nuclear spin statistical weights for CH_4 and CD_4, taken from Ref. [HOUG76].

Molecule	Rovibrational species	Nuclear spin functions	Overall species	Statistical weight
CH_4	A_1	$A_1(I=2)$	A_1	$(2I + 1) = 5$
	A_2	$A_1(I=2)$	A_2	$(2I + 1) = 5$
	E	$E(I=0)$	A_1+A_2	$2(2I + 1) = 2$
	F_1	$F_2(I=1)$	A_2	$(2I + 1) = 3$
	F_2	$F_2(I=1)$	A_1	$(2I + 1) = 3$
CD_4	A_1	$A_1(I=4,2,0)$	A_1	$\Sigma_I(2I + 1) = 15$
	A_2	$A_1(I=4,2,0)$	A_2	$\Sigma_I(2I + 1) = 15$
	E	$E(I=2,0)$	A_1+A_2	$2\Sigma_I(2I + 1) = 12$
	F_1	$\begin{pmatrix}F_2(I=3,2,1)\\F_1(I=1)\end{pmatrix}$	$\begin{pmatrix}A_2\\A_1\end{pmatrix}$	$\Sigma_I(2I + 1) = 18$
	F_2	$\begin{pmatrix}F_2(I=3,2,1)\\F_1(I=1)\end{pmatrix}$	$\begin{pmatrix}A_1\\A_2\end{pmatrix}$	$\Sigma_I(2I + 1) = 18$

For CD_4, the nuclear spin statistics are more complicated, since the peripheral atoms have higher spin $(I=1)$. The nuclear spin wavefunctions must be labelled by symmetry C^{ns} as well as total spin I in order to distinguish them: note that for $I=2$, for example, there are three different spin species $C^{ns} = A_1$, E, F_2. Table 4-3 shows that a rovibrational level of symmetry species C contains more than one nuclear spin species, which don't interconvert by collision. Therefore, when we excite CD_4 molecules to a rovibrational level of species F_2, to take an example, we excite simultaneously molecules with four different nuclear spin functions. Collisional energy transfer then proceeds in parallel for the four different species, undistinguished by our experiment. Examination of Table 4-3 shows that the collisional transitions allowed by nuclear spin conservation still obey the same selection rules, Eq. 4.1, as for CH_4. It is fortunate that the simple expression still holds. The finer distinctions arising from the larger number of nuclear spin functions in CD_4 are masked by a degeneracy with respect to the rovibrational designation. In a preliminary account of our work on $^{13}CD_4$, we made a simple demonstration of the operation of these selection rules [LAUX84]. Note that the considerations of parity for collisional changes of state also remain intact for the deuterated molecule. A transition $F_1 \rightarrow F_2$ must involve a change of overall species in order to conserve nuclear spin, although in this case the change of overall species is *either* $A_1 \rightarrow A_2$ or $A_2 \rightarrow A_1$.

4.2 Vibrational Energy Transfer

Three distinct vibrational energy transfer processes should be considered for methane molecules in the ν_4 vibrational state. In order of descending probability, these are:

(I) Intramolecular V-V:
$$^{13}CD_4(\nu_4) + M \longrightarrow {}^{13}CD_4(\nu_2) + M$$

(II) Intermolecular V-V:
$$^{13}CD_4(\nu_4) + {}^{13}CD_4(0) \longrightarrow {}^{13}CD_4(0) + {}^{13}CD_4(\nu_4/\nu_2)$$
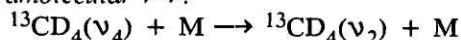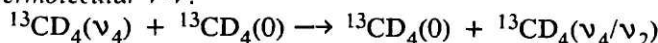
(III) Vibration-to-translation, V-T:
$$^{13}CD_4(\nu_4) + M \longrightarrow {}^{13}CD_4(0) + M$$
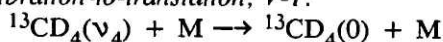
We have omitted collisional excitation of molecules from ν_4 to vibrational levels higher than ν_2 (e.g., $\nu_4 \rightarrow 2\nu_4$) on the grounds that the large uptake of energy required (~ 1000 cm^{-1}) makes it unlikely. Process (I) is expected to be quite feasible since it can occur with a very small change of internal energy. The rotational level stacks of ν_2 and ν_4 are overlapping in energy, creating the possibility of nearly isoenergetic transfer for a suitable change of J ($\Delta J \simeq 2$). (See Fig. 2-4.) Process (II) can occur with a very small change in the total vibrational energy of the two colliding molecules, but requires a very substantial transfer of energy (~ 1000 cm^{-1}) from one molecule to another. This transfer is unlikely to take place within the short time duration of the collision. In some molecules, intermolecular V-V transfer may be enhanced by the long-range forces that arise from the oscillating dipole moment of the vibrating molecule [YARD80], but in methane, the transition dipole moment of ν_4 is probably too small ($\mu \simeq 0.05$ D) to have a large effect. Finally, process (III) entails the conversion of a large amount of vibrational energy to translational energy, and is notoriously slow for that reason. For the molecule $^{12}CD_4$, the V-T rate for self-relaxation is 290(80) sec^{-1} Torr^{-1} [ZITT73], which corresponds to

$$\sigma_{VT}/\sigma_{LJ} \simeq 2.5 \times 10^{-5}.$$

For $^{12}CD_4$ - He collisons, this ratio was found to be simlarly small, 5.6×10^{-5}. The hierarchy of rates embodied in this discussion is discussed at length by Yardley [YARD80].

With our detailed spectroscopic data in hand, we set out to observe intramolecular V-V transfer in $^{13}CD_4$. A typical example of a decay curve for an IRDR signal is shown in Fig. 4-2, curve (b). This was obtained by exciting to the level (J=11, F_2^7) in ν_4 and monitoring the probe transition Q(7) $F_2^6 \rightarrow F_1^{16}$ of the hotband $\nu_2 + \nu_4 \leftarrow \nu_2$. On the vertical axis we plot the amount of absorption of the probe laser beam, which is proportional to the population of the probed level. Signal levels are extremely low in this pump-probe scheme, since the initial population of the

pumped level is dispersed among a very large set of final levels. It was necessary to average the signal for 32,000 pulses of the pump laser to obtain the curve shown. The curve exhibits a slow exponential rise and a slower decay. Since the rise time of the curve is about 3 times longer than the 500 nsec duration of the pump-laser pulse, it is an accurate reflection of the V-V relaxation time between the ν_4 and ν_2 levels.

Before analyzing the curve for its rise time, however, we must consider the rotational specificity of the V-V channel that we detect. The rate of increase of population in the probed level contains contributions from the following energy transfer pathways.

(i) $(\nu_4, J=11, F_2^7) \longrightarrow (\nu_2, J=7, F_2^6)$

(ii) $(\nu_4, J=11, F_2^7) \longrightarrow (\nu_4, J_{int}) \longrightarrow (\nu_2, J=7, F_2^6)$

(iii) $(\nu_4, J=11, F_2^7) \longrightarrow (\nu_2, J_{int}) \longrightarrow (\nu_2, J=7, F_2^6)$

The first pathway is simple direct transfer from initial to final level. The second pathway involves rotational relaxation to intermediate levels within ν_4, followed by V-V transfer to the probed rotational level through a number of possible rotational pathways. Similarly, pathway (iii) involves intermediate rotational levels of ν_2, from which rotational relaxation can lead to the final level. In order to assess the relative contributions of direct and indirect pathways, we tuned the probe laser to a nearby transition to monitor the ν_4 level ($J=12$ F_1^5). The result is shown as curve (a) of Fig. 4-2. This curve does not have a simple exponential rise, but a complicated profile that results from rotational redistribution within the ν_4 state. It is apparent that this redistribution is somewhat faster than subsequent transfer to levels of the ν_2 state. Since these pathways operate simultaneously, we must conclude that the direct transfer, pathway (i), is obscured by the "scrambling" effect of pathways (ii) and (iii). The rise time of curve (b) in Fig. 4-2 must therefore be considered to be a rotationally averaged V-V relaxation time, even though we measure it by monitoring an individual rotational state of ν_2.

69
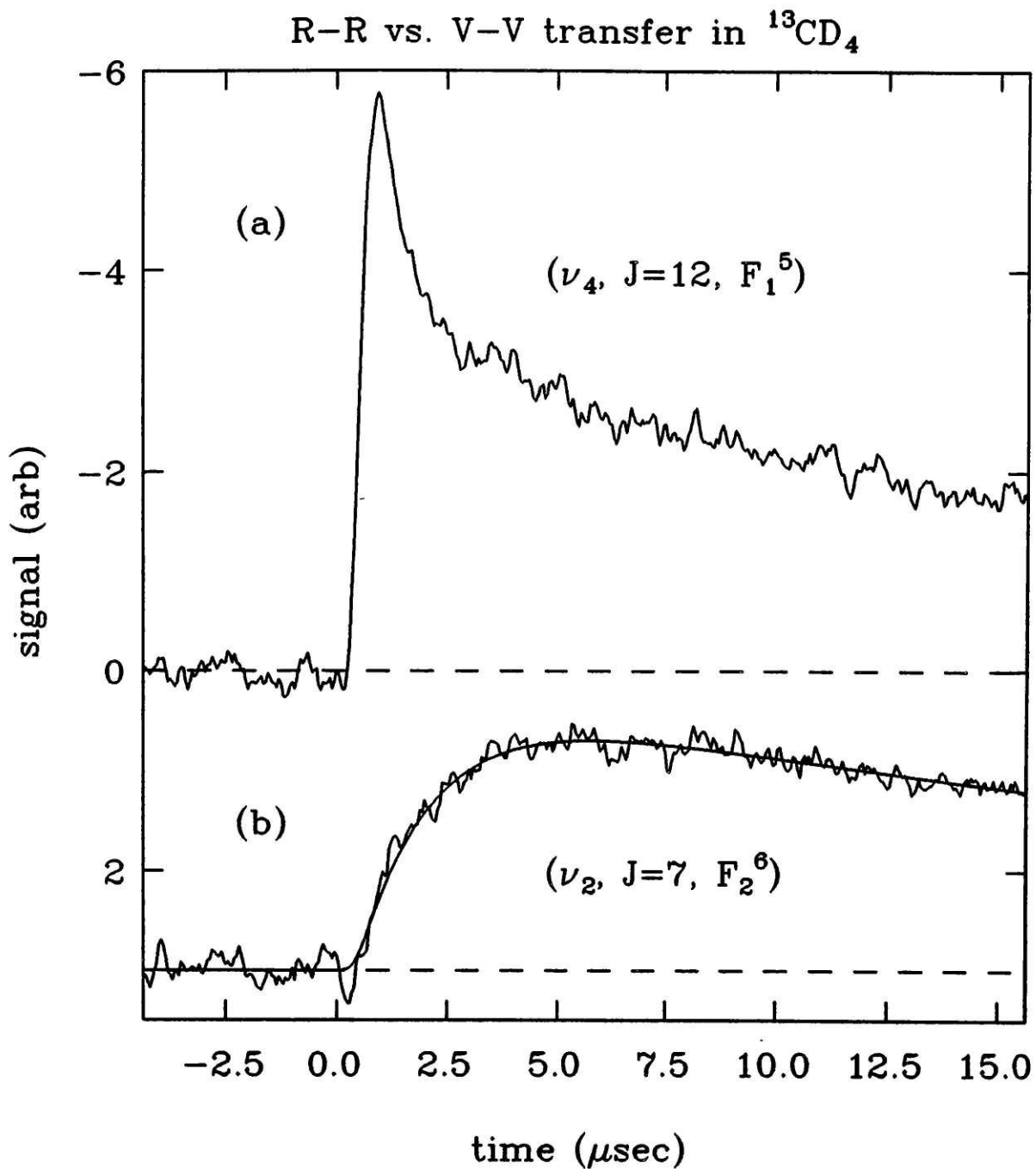
Figure 4-2: Decay Curves For Vibrational (V-V) and Rotational Energy Transfer

Initial level: $(\nu_4, J=11, F_2^7)$. (a) Probe laser tuned to a $2\nu_4 \leftarrow \nu_4$ transition. (b) Probe on $\nu_2 + \nu_4 \leftarrow \nu_2$ transition. Pressure: 200 mTorr $^{13}CD_4$ + 460 mTorr He. For the fitted curve in (b), $\lambda_+ = 0.614(19)~\mu sec^{-1}$ and $\lambda_- = 0.0302(13)~\mu sec^{-1}$.

In view of these considerations, we can implement a simple kinetic analysis that allows us to estimate the $\nu_4 \rightarrow \nu_2$ effective energy transfer rate. If we make the simplifying assumption that rotational equilibration in ν_4 precedes the vibrational equilibration with ν_2, we can model the problem as a three-level system, shown in Fig. 4-3, in which the vibrational states are considered as single levels. Both can transfer population to the ground vibrational state by relatively slow (and irreversible) V-T pathways. The solution of the set of coupled differential equations for this system is given by Yardley [YARD80, pp. 65-67]. In simplified form, we can write it as:

$$N_4(t) = c_4 e^{-\lambda_+ t}$$

$$N_2(t) = c_2 \left(e^{-\lambda_- t} - e^{-\lambda_+ t} \right)$$

where

$$\lambda_+ = K_{24}(1 + \chi)$$
$$\lambda_- = (K_{04} + K_{02})/(1 + \chi)$$
$$\chi = (g_4/g_2)\exp[-(E_4 - E_2)/kT]$$

and

N_4, N_2 are the populations of ν_4 and ν_2

E_4, E_2 are the energies of ν_4 and ν_2

g_4, g_2 are the vibrational degeneracies

c_4, c_2 are constants depending on the initial populations and rate parameters [YARD80]

$K_{ij} = \Sigma_M k_{ij}[M]$

The important feature is that, under the assumption that the three-level description is valid, the population curve for ν_2 contains an exponential rise and an exponential fall. This seems to be a good description of the observed curve (b) in Fig. 4-2. The exponential rise rate bears a simple relationship to the V-V transfer rate. A fitted bi-exponential curve is shown with the data in Fig. 4-2b. The bi-exponential function is convoluted with the temporal profile of the pump-laser pulse to take into account the non-negligible duration of the excitation.
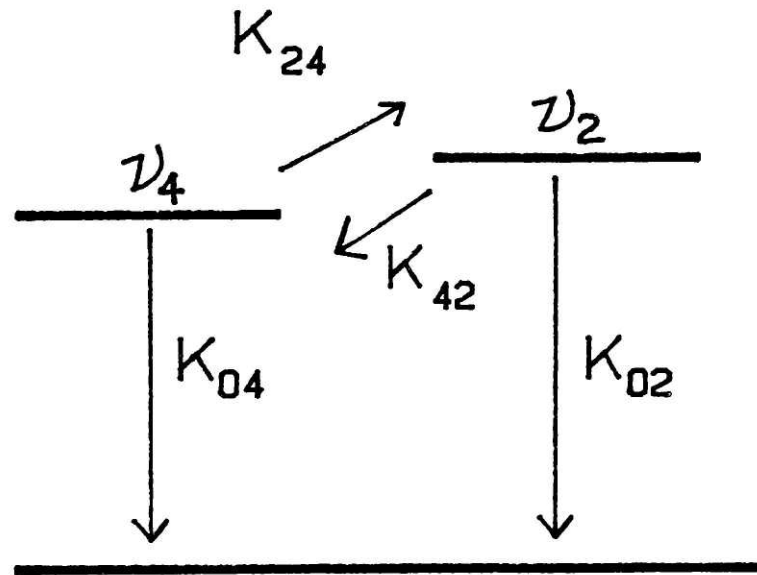
Figure 4-3: Three-Level Kinetic Model for V-V Energy Transfer

We obtained curves as in Fig. 4-2b for a series of $^{13}CD_4$-He mixtures with $p(^{13}CD_4) = 0.2$ Torr and $p(He) = 0.3$-1 Torr. The resulting rate constants for V-V transfer for collisions with $^{13}CD_4$ and with He are shown in Table 4-4. The effective V-V cross section is only a fraction of the Lennard-Jones cross section, similar to other V-V rates in methane measured by other techniques [YARD80]. Optoacoustic measurements of the $\nu_4 \to \nu_2$ rate in CH_4 yielded a much smaller value than our measurement [AVRA81]. This is caused partly by the larger vibrational energy gap (~ 200 cm^{-1}), but the difference in rates might also reflect the difficulties in extracting state-to-state rate constants from acoustic data. Our measurement of the $\nu_4 \to \nu_2$ rate is the first in which the rate of increase of population in ν_2 is detected directly. This is not possible with detection by infrared fluorescence, since ν_2 is infrared-forbidden.

Table 4-4. Vibrational Relaxation Rate Constants

Coll. partner	k_{VV} (μsec^{-1} Torr^{-1})	σ_{VV} ($\mathring{A}^2$)	σ_{LJ} ($\mathring{A}^2$)
self	0.56(11)	2.3(5)	49.7
He	0.076(22)	0.17(5)	21.5

		Previous Measurements (self-relaxation)	
Molecule	Process	k	Ref.
$^{12}CD_4$	$\nu_4 \to 0$ (V-T)	340(14) sec^{-1} Torr^{-1}	[PERR82] (Optoacoustic)
$^{12}CH_4$	$\nu_4 \to \nu_2$	0.017 μsec^{-1} Torr^{-1}	[AVRA81] (Optoacoustic)
$^{12}CH_4$	$\nu_3 \to 2\nu_4, \nu_2 + \nu_4$	0.6 μsec^{-1} Torr^{-1}	[YARD80] (IR fluor.)

A more detailed analysis of the V-V energy transfer rate was not attempted. The three-level kinetic system used in our analysis is probably not detailed enough, since the comparison shown in Fig. 4-2 demonstrates that a significant amount of V-V transfer takes place on the time scale of rotational relaxation. We obtained decay curves for a few other levels of ν_2 using the same pumped transition. We found that the rise rates (λ_+) of the curves do not vary significantly, although the slower falling portions of the curves have a slight dependence on rotational state. This suggests that the falling portion of the curve $N_2(t)$ is related to rotational redistribution occurring in ν_2 during the measurement. The simple three-level model, however, does not account for

rotational relaxation within either vibrational state. The V-V rate constants reported in Table 4-2 should be interpreted as effective rate constants for $\nu_4 \rightarrow \nu_2$ energy transfer that represent averages over the many rotational pathways involved.

A more satisfactory approach to our data would involve the explicit treatment of individual rotational levels within ν_4 and ν_2. similar to what we will describe for rotational relaxation later in this chapter. The solution of the system of the numerous coupled levels would be very difficult. In order to make a meaningful comparison between kinetic model and experiment, one would need an exhaustive set of data for the evolutions of rotational level populations in ν_2. We elected not to follow such an approach, although we have shown that in principle it is possible. Until a more detailed analysis is achieved, we may proceed with our analysis of rotational energy transfer in ν_4. using the assumption that the rate constants in Table 4-2 are representative of the rates of loss of population from rotational levels of ν_4 by V-V energy transfer.

The initial part of the decay curve in Fig. 4-2a corresponds to purely rotational relaxation in ν_4. One can see that this occurs rapidly compared to the duration of the pump-laser pulse. Our next step is to perform a kinetic analysis of such curves in order to extract rate constants for state-to-state rotational energy transfer. In order to obtain meaningful rate constants, the excitation pulse needs to be short compared to the rise time of the curve in Fig. 4-2a. This could be achieved by resorting to lower pressures (or collision frequencies), but the signal-to-noise ratio of the data would be reduced beyond tolerable limits. We felt that the wisest course of action was to use a shorter pump-laser pulse. We turn now to a brief discussion of the relevant experimental details.

4.3 Experimental — The CO_2 TEA Laser

The pulse duration of the rotating-mirror laser used up to this point cannot be made shorter than 500 nsec (FWHM), except by extracavity chopping with an electro-optic device. We decided instead to use a pulsed-discharge CO_2 laser of the TEA type (Transverse Excitation at Atmospheric pressure). This type of CO_2 laser is known to produce a pulse with a short "spike" that is useful for time-resolved experiments. Since a great deal of signal averaging is required for our measurements, the operation of the TEA laser at high repetition rates is necessary. We designed and built a laser in our laboratory with this goal in mind.

The electrodes used to create the high-voltage (25 kV) discharge in the laser head were purchased from Tachisto Laser Systems Inc. They are made of aluminum and are nickel-plated,

and measure 16 in. × 1¼ in., with a thickness of 3/8 in. The electrodes are separated by ½ in. The key ingredient that allows the pulsed discharge to operate at high repetition rates (up to 50 Hz, or pulses/sec) is a high-speed, high-output circulation fan positioned close to the discharge region. Rapid circulation of the discharge gases is necessary so that the sample between the electrodes is replenished between shots; a build up of decomposition products otherwise occurs, leading to arc discharge between the electrodes. The fan is a tangential blower (Lau Inc., model T3-18.0) whose 18 in. length matches the length of the discharge region. It is turned by an electric motor stationed outside of the laser head. The rotary feedthrough coupling the motor to the fan must be air-tight, so that the gas mixture remains pure during operation. (Exclusion of atmospheric gases from the mixture is very important for arc-free operation.) We used a vacuum rotary feedthrough from Ferrofluidics Corp. in which a simple vacuum-sealed shaft extends to either side of the interface, allowing one to apply high torque to the fan. The gas mixture in the laser head is cooled by a heat exchanger mounted next to the circulation fan.

Pre-ionization of the gas mixture is accomplished by the simple method of spark discharges by rows of pins along either side of the electrodes, 2 in. away from the center of the discharge. The 32 pairs of pins are made from 0.165 in. brass rod, grooved at the ends to make sharp edges. The assembly of electrodes and pre-ionization pins and capacitors is contained in a welded stainless-steel box with inside dimensions 24 in. × 16½ in. × 7½ in. The assembly is suspended beneath an insulating piece of Delrin that forms the top of the box. All seams in the structure are carefully fitted with O-ring seals, so that the laser head can be evacuated to a pressure of < 1 Torr before filling with the gas mixture.

The high-voltage circuit that excites the discharge is shown schematically in Fig. 4-4. The thyratron, storage capacitor, and charging and damping resistors are contained in a shielded box (the "modulator") to minimize the escape of rf noise. The high-voltage pulse (~25 kV) generated by the modulator is carried to the laser head by a 5 ft. coaxial cable (Rowe Ind.) to which we attached additional shielding. The added shielding was anchored firmly to the panelling at either end by a flange arrangement, so that a continuous Faraday enclosure surrounds the main current loop of the discharge circuit. The shielding must be attached *at the point of entry* of the cable in order to suppress rf noise.

75
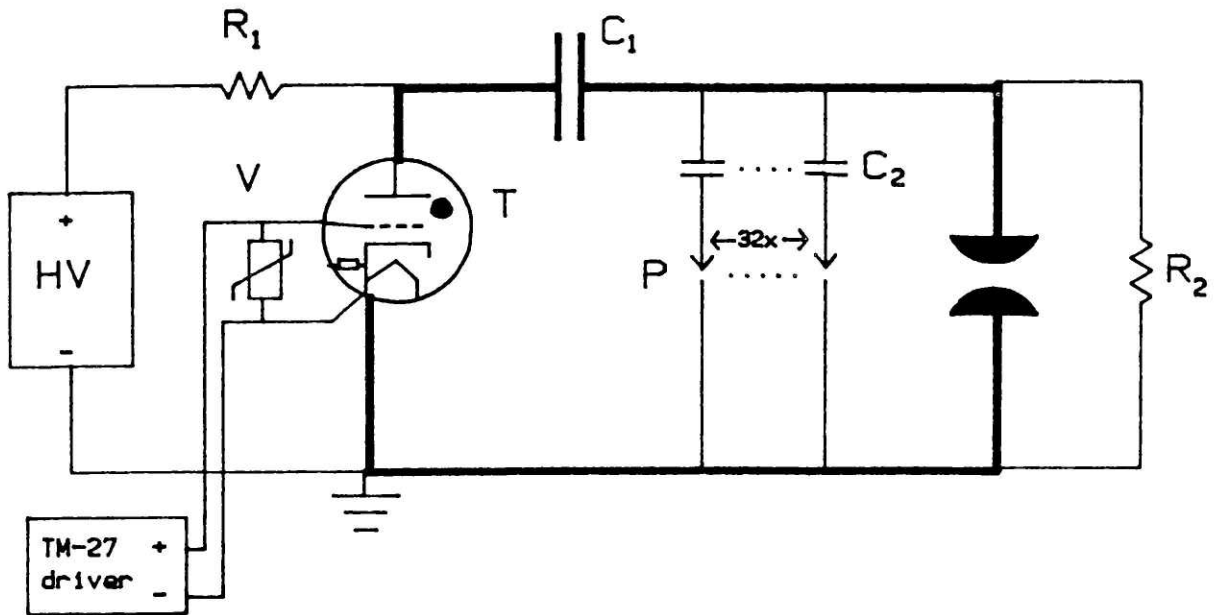
Figure 4-4: CO_2 TEA Laser Circuit Diagram

The components are as follows:

HV: 35 kV DC switching power supply (Candela HVD-1000A)

R_1: Charging resistor, 50 Ω, 225 W

R_2: Damping resistor, 1 kΩ, 50 W

C_1: Storage capacitor, 0.02 μF (Maxwell Labs): rated at 35 kV, 100 Hz discharge rate

C_2: Pre-ionizer capacitors, 461 pF, 30 kV (Murata); 32 total

T: Thyratron, EG&G HY-32

TM-27: Thyratron driver unit (EG&G)

P: Pre-ionization pins, made from brass rod; 32 total

V: Varistor (GE MOV V660PA100C)

Brewster windows made of ZnSe (Two-Six, Inc.) were epoxied to Delrin mounts, attached to the laser head by O-ring flanges machined into the mounts. Wavelength selection of the laser output was achieved by a Littrow-mounted grating (PTR Optics, ML-303, 150 lines/mm, original ruling). An output coupler is positioned at the other end of the optical cavity. This element is a plano-concave partially reflecting ZnSe window (Two-Six) with 1 in. diameter and 10 m radius of curvature, coated for 85% reflection at 10.6 μm on the curved side and A.R. coated on the flat side. An iris diaphragm is used as an intracavity aperture to control the transverse mode quality.

4.3.1 Control of the Pulse Length

The highest pulse energies are obtained when the TEA laser is operated with a gas mixture of He, CO_2, and N_2 at ratios of approximately 4:1:1, and with a total pressure of 3 p.s.i.g. (1.2 atm). The time profile of the pulse under these conditions is similar to that shown in Fig. 4-5a, in that it contains an initial "spike" of duration ~75 nsec, and then a long "tail" extending to ~1 μsec. This curve was obtained with a photon-drag detector (Rofin model 7425) with time response ~1 nsec, recorded by a transient digitizer (Tektronix 7912AD) with time response ~2 nsec. The "tail" of the pulse is an undesirable feature in its effect on the decay profiles of double resonance signals for state-to-state energy transfer. It could make it difficult to distinguish between similar rise times for different pathways. Fortunately, the "tail" can be suppressed by a variety of techniques, the simplest of which is reduction of the N_2 content of the gas mixture. When we use a gas mixture of He and CO_2 in the ratio 4:1, and make sure to close the intracavity iris to a small diameter (~7 mm), the pulse shape of Fig. 4-5b results. The "tail" is virtually eliminated here, but at the expense of the pulse energy, which is reduced to ~20% of its value with the normal gas mixture. Still, we obtain typically 5-15 mJ/pulse for the pulse shape of Fig. 4-5b; this was used for the state-to-state energy transfer experiments described in this chapter. Figure 4-5a demonstrates that the "tail" of the pulse persists even when N_2 is absent from the gas mixture, if one opens the intracavity iris too far.

Also shown in Fig. 4-5b is the shape of the CO_2 TEA laser pulse as obtained by the detection system used for the probe laser (viz., the HgCdTe detector and the Biomation transient recorder). This reflects the limited detection bandwidth for the decay curves that we will discuss in this chapter. The longer pulse shape represents the effective excitation profile for the pumped transition.

77
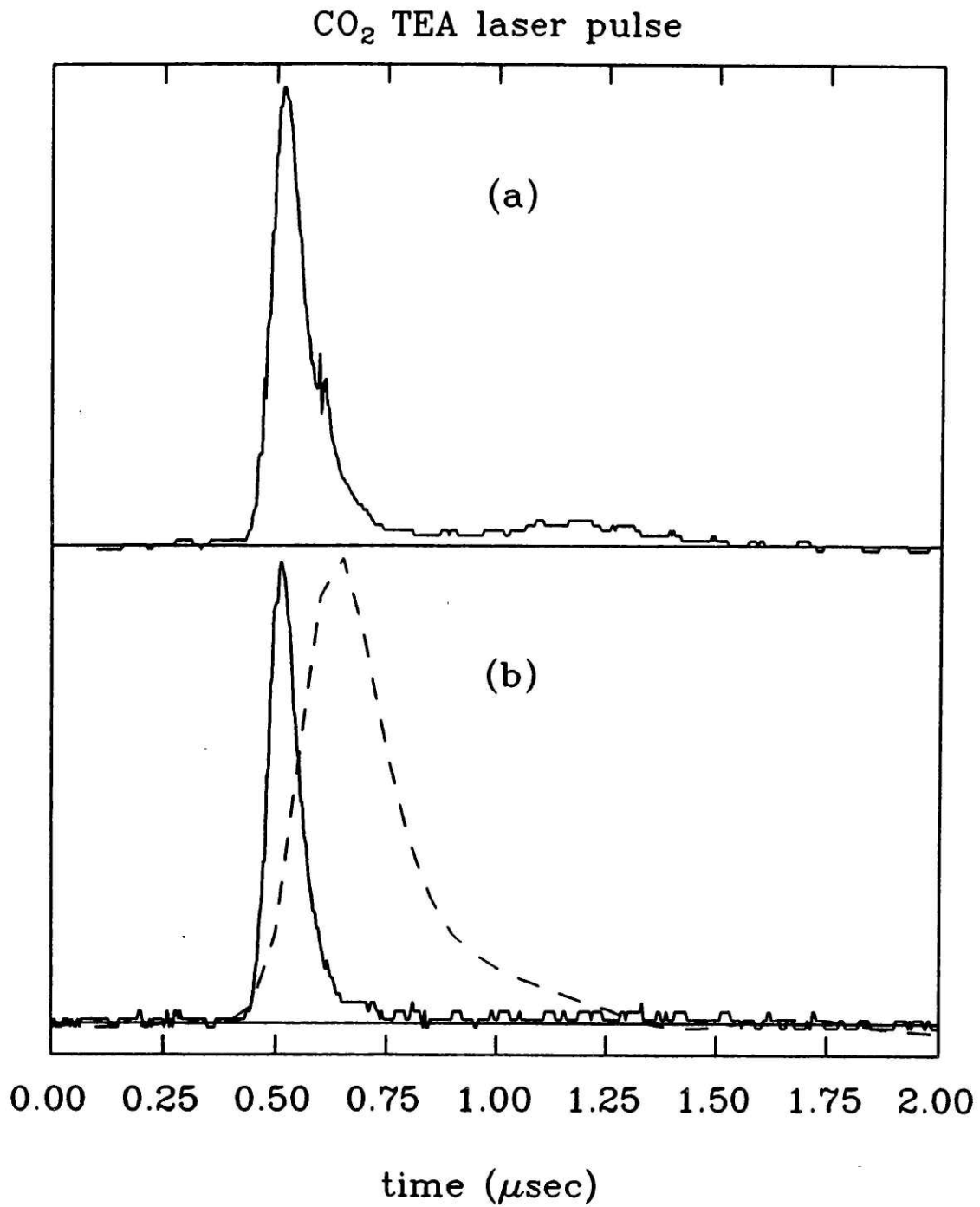
CO$_2$ TEA laser pulse

Figure 4-5: CO$_2$ TEA Laser Pulse

Gas mixture of He:CO$_2$ = 4:1. (a) Intracavity iris opened. (b) Iris closed to eliminate tail of pulse. Dashed curve shows pulse shape as detected by probe-laser detector (HgCdTe) and Biomation digitizer.

The large pressure-broadened bandwidth of the CO_2 TEA laser output (perhaps 3 GHz in a gas mixture at 1 atm) encompasses several longitudinal modes of the optical cavity. The multiple modes in the output beat against each other, causing the time profile of the pulse to take on a jagged appearance. This is shown in Fig. 4-6, where the digitizer time scale is expanded, as compared to Fig. 4-5. Since the cavity length of our laser is not stabilized, the envelope of frequency components in the laser output shifts randomly on a shot-to-shot basis, so that the pattern of mode beating is highly variable. Fig. 4-6 therefore shows a portion of a *single* laser shot, which displays a prominent beat component at 143 MHz. This arises from interference between neighboring longitudinal modes, which are separated by c/2L [DEMT82], where c is the speed of light and L the cavity length (L = 105 cm in our laser). Although mode beating in the pulse profile can be eliminated by operating in a single longitudinal mode [DEMT82], we made no effort to do so, since the response of the probe-laser detection system is not fast enough to be affected by the rapid oscillations of Fig. 4-6.

4.3.2 Problems with the Operation of the CO_2 TEA Laser

The TEA laser can operate at repetition rates as high as 50 Hz without a serious decline in the pulse energy. Long-term operation at high repetition rates is not possible, however, since the pulse energy gradually decreases and occasional arcs occur in the discharge within a few minutes. More satisfactory performance was achieved at lower pulse repetition rates, so we generally ran the laser at 20 Hz during data collection. In this way, the laser can be left on for more than an hour at a time without trouble, as long as the gas mixture is flowed slowly through the laser head. After extended periods, however, we found it necessary to pump out the laser head and replenish the gas mixture in order to restore the pulse energy. The inability of the laser to run satisfactorily at high repetition rates is probably due to the inefficiency of pre-ionization by pin-type spark discharges, since this leads to a build up of gases harmful to the discharge (such as CO and O_2). Replacing the pre-ionization setup, however, would probably entail a nearly complete reconstruction of the laser head and HV electronics.

Mode—beating in CO_2 pulse

time (nsec)
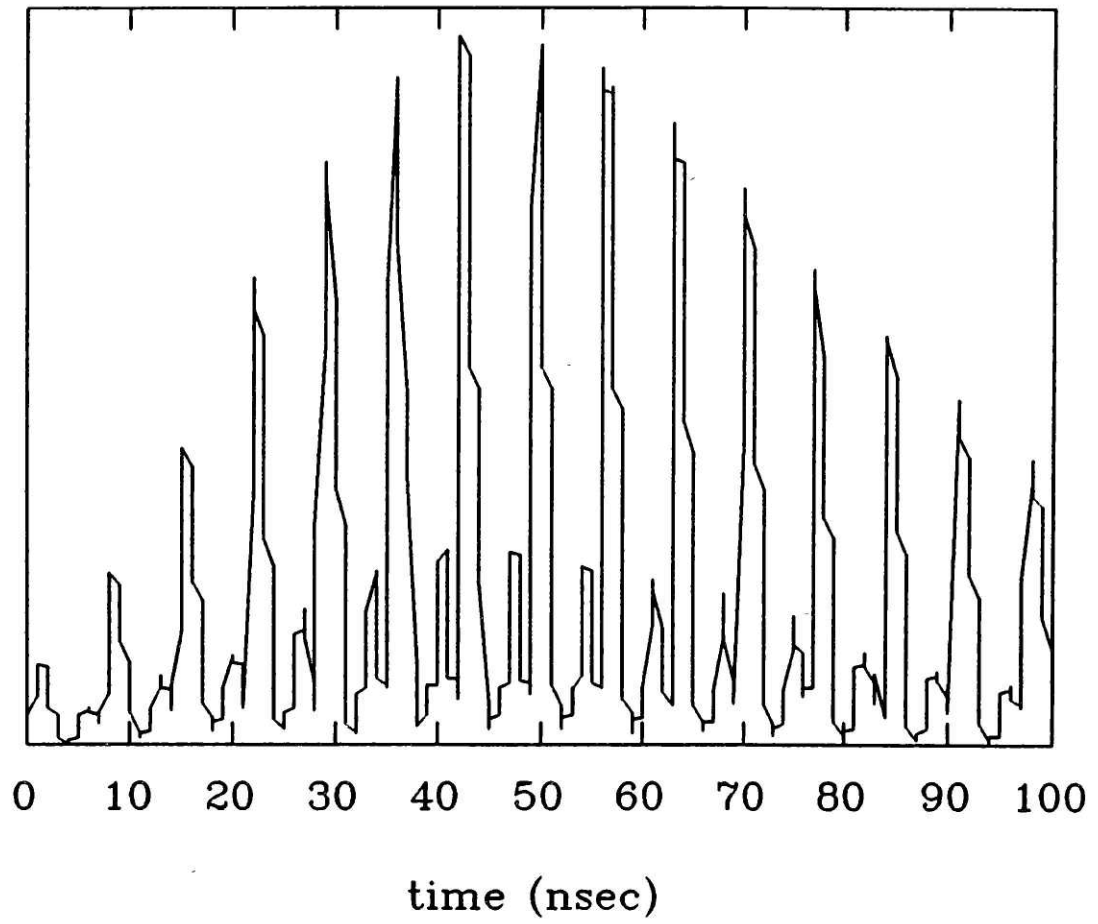
Figure 4-6: CO_2 TEA Laser Pulse at High Time Resolution

Another problem with our CO_2 TEA laser is that it produces a prodigious amount of rf noise. The ground of the laser should be isolated from the grounds of all other instruments because of the high peak currents surging through the system. The less-than-ideal designs of the laser head and modulator make it extremely difficult to shield the system well. short of placing the entire apparatus in a shielded room. The latest and most advanced designs by commercial manufacturers are compact, well shielded. and more nearly noise-free, and would be less troublesome than our laser. We found that the Laser Analytics diode laser apparatus is *extremely* sensitive to rf noise, requiring us to take special precautions against pickup. These measures are described in Appendix 3. In addition. we took the usual step of insuring that all signal-carrying BNC cables were well shielded. We generally used RG-223 cable, which has a double layer of shielding, and sometimes added another layer of copper braid to the exterior of the cable.

4.3.3 A Word About Timing of the Electronics

When collecting a large number of digitized decay curves for signal averaging. one must insure that the detection electronics are timed reliably. The boxcar integrator and transient recorder must be synchronized with the pump-laser pulse with a minimum of time jitter (<20 nsec). One way to attempt this is to use the "synch out" pulse of the thyratron driver (TM-27) in the TEA laser electronics. but we found that the resultant jitter was too large. Also. the BNC cable carrying the "synch out" pulse acts as an efficient conduit for rf noise from the TEA laser. The best solution is to use an "optical trigger": we detect scattered radiation from the pump-laser pulse with a fast (HgCdTe) infrared detector, and use that pulse as a trigger. This technique has one drawback: the scattered-light detector that we use has an intrinsic delay, so that the signal-processing electronics are not triggered until ~ 300 nsec after the start of the pump-laser pulse. In order to establish a good baseline for our decay curves, we need to begin recording the signal 1-2 μsec before the laser pulse. The transient recorder was therefore operated in "pre-trigger" mode, in which it stores in memory a portion of the signal occurring at a selected time prior to the trigger. This feature of the Biomation transient recorder was essential to the data acquisition.

4.4 Rotational Energy Transfer in Methane-Methane Collisions

We turn now to an examination of purely rotational energy transfer pathways within the ν_4 vibrational state of $^{13}CD_4$. The initially excited level implied throughout the discussion is $(\nu_4, J = 11, F_2{}^7)$, obtained through the pump transition shown in Table 4-2. The following discussion will be oriented around a survey of relaxation pathways that we made involving many final rotational states, but all studied at a pressure of 200 mTorr of $^{13}CD_4$. This pressure was judged to be a good compromise between the trade-off factors of acceptable signal-to-noise ratios and sufficiently slow relaxation rates. A few selected pathways were studied at several pressures in the range 100 to 200 mTorr. At pressures in this range, we averaged decay curve signals over typically 5,000-10,000 pump-laser shots, depending on experimental conditions. All of our observations result from methane-methane collisions only; no mixtures with buffer gases were used. The pathways that we were able to monitor are listed in Table 4-1. Following a qualitative description of the rotational energy transfer data, we will discuss a kinetic model of the results that will give us some quantitative measures of the rates involved.

4.4.1 Description of the Results

Collision-induced changes of rotational state in the ν_4 level of methane can involve changes of several independent quantities. Perhaps the most elementary of these is the total angular momentum J. We might expect that the probability of a quantum number change ΔJ generally decreases with increasing $|\Delta J|$, since there is a limited amount of torque between molecules that can arise in a collision. The likelihood of a transition ΔJ is constrained also by the accompanying change of energy; for example, for $\Delta J = -4$ from the initial level, $\Delta E_{rot} \simeq -k_B T$. We must also be aware of changes of the approximate quantum number R, which corresponds to the purely rotational angular momentum, separated from the angular momentum of vibration. For the probability of a transition ΔR, the same constraints apply as for ΔJ. But we should also consider the combination of the two changes, since it is related to the state of the vibrational angular momentum. In Chapter 2, we saw that the quantity $(R - J)$ has the three values $+1$, 0, and -1 in the state $\nu_4 = 1$. The pumped transition, $P(12)F_1{}^1 \rightarrow F_2{}^7$, terminates in the F^+ Coriolis sublevel, where $(R - J) = +1$ [HERZ45]. Hence, we can monitor separately transitions of $\Delta(R - J) = 0$, -1, and -2. Finally, we need to consider collisional changes of the rotational fine-structure label C^n: we may have $F_2{}^7 \rightarrow F_1{}^n, F_2{}^m$, where the final level may have arbitrary quantum numbers J and R. We should bear in mind that the separation between fine-structure levels is small compared to the separation between levels of different J and R (cf. Fig. 2-3). How do we expect the energy

transfer probability to vary with ΔC^n? We don't know what to expect, except that energy constraints should not be important. In the following discussion, we will consider in sequence our observations for ΔC^n, $\Delta(R - J)$, and ΔJ.

Let us first examine relaxation pathways to different C^n levels. Figure 4-7 shows one comparison for pathways from $(\nu_4, J = 11, F_2{}^7)$ to $(\nu_4, J = 12, R = 13)$. The decay curves display remarkable differences. For the level $(J = 12, F_2{}^8)$ there is a large and rapid initial increase in population, followed by a loss of population to other neighboring levels; the other levels show only a slow initial uptake of population, after which they remain at a nearly constant level on the observed time scale. We should mention that several collisions occur during the measurement period; at 200 mTorr, the mean interval between collisions (as determined from the Lennard-Jones collision cross section) is about $0.5 \,\mu$sec, and we measure signals for several microseconds. Thus, we expect that population transfer by multiple-step pathways can make a contribution to the observed signal, in addition to the simple single-step pathways from initial to final level caused by one collision. Later in this chapter we will try to distinguish the effects by kinetic modelling, but for now we can say that the data in Fig. 4-7 indicate clearly that the transition probabilities from initial to final state are substantially different for the particular fine-structure levels indicated. This is true despite the close similarity of the energy gaps in the three cases ($\Delta E = 58\text{-}62$ cm^{-1}).

The contrasting behavior for different final levels C^n can also be seen for levels of other final J values. Fig. 4-8 shows comparisons for two pathways of $\Delta J = -2$ and for two pathways of $\Delta J = -5$. We are therefore led to the surprising conclusion that rotational energy transfer in methane is selective with respect to the fine-structure designation C^n, even when the final levels have the same J_R values. Figs. 4-7 and 4-8 seem to indicate that the energy transfer pathways may be divided roughly into two classes of rates, at least for the purpose of discussion: there are "principal" pathways, for which a large initial peak occurs in the population evolution, and "secondary" pathways that do not display a large peak.

Figure 4-7: Energy Transfer to 12_{13} F$^+$ Levels (next page)
Pressure: 200 mTorr $^{13}CD_4$.

Figure 4-8: C^n-Selective Transfer to J $= 9, 6$ F$^+$ Levels
(following page)
Pressure: 200 mTorr $^{13}CD_4$

$J_R = 11_{12}(F_2{}^7) \rightarrow 12_{13}$ levels

signal (arb)

-3

-2

-1

0

1

2

3

$12\ F_2{}^8 \quad \Delta E = 62.4\ \text{cm}^{-1}$

$12\ F_1{}^8 \quad \Delta E = 61.9\ \text{cm}^{-1}$

$12\ F_1{}^7 \quad \Delta E = 58.4\ \text{cm}^{-1}$

$0 \quad 1 \quad 2 \quad 3 \quad 4 \quad 5 \quad 6 \quad 7$

time (μsec)

$9_{10}F_1^{6}$ $\Delta E = -112.8$ cm^{-1}

$9_{10}F_2^{7}$ $\Delta E = -113.1$ cm^{-1}

$6_7F_2^{5}$ $\Delta E = -241.8$ cm^{-1}

$6_7F_1^{5}$ $\Delta E = -242.0$ cm^{-1}
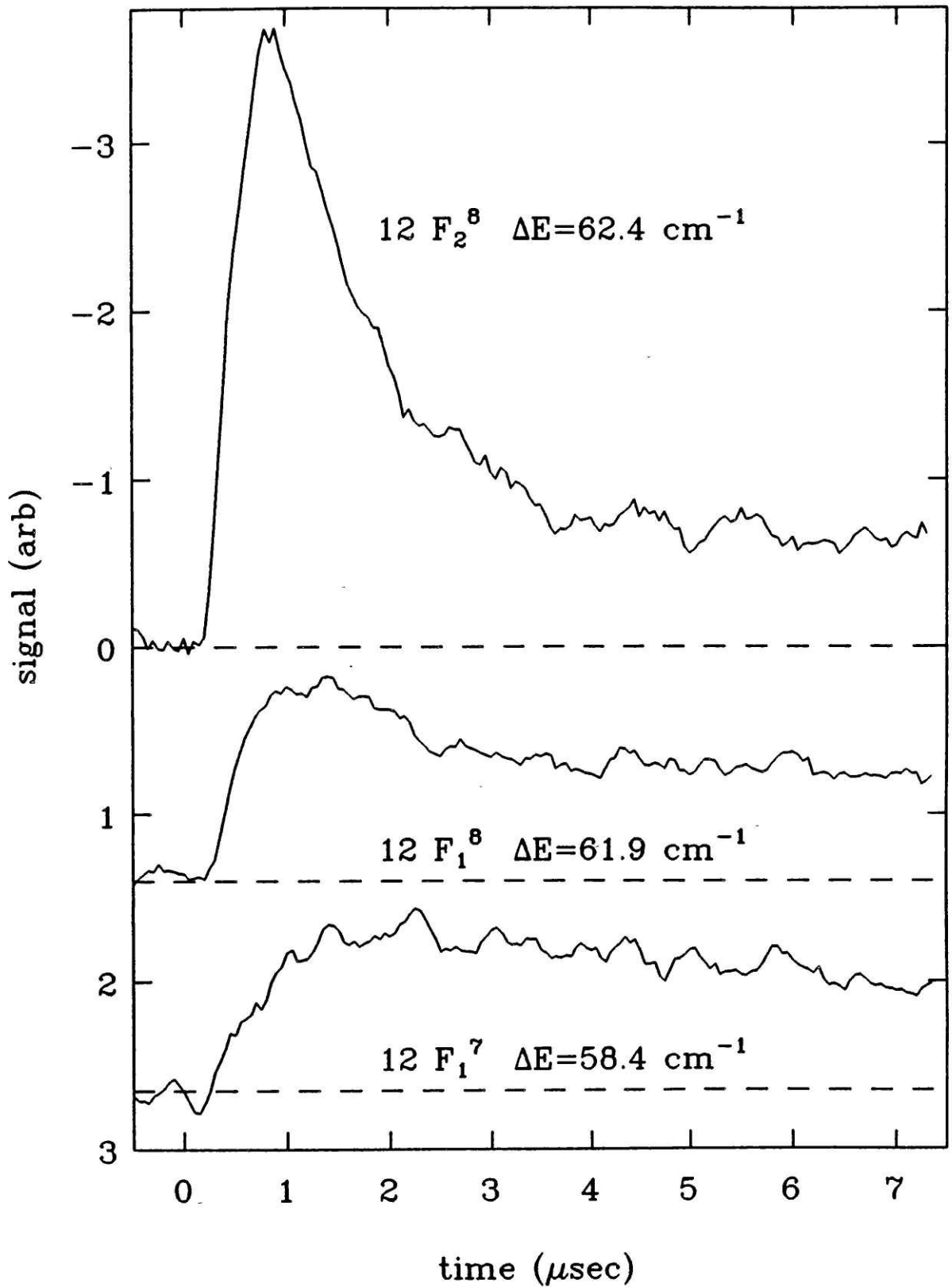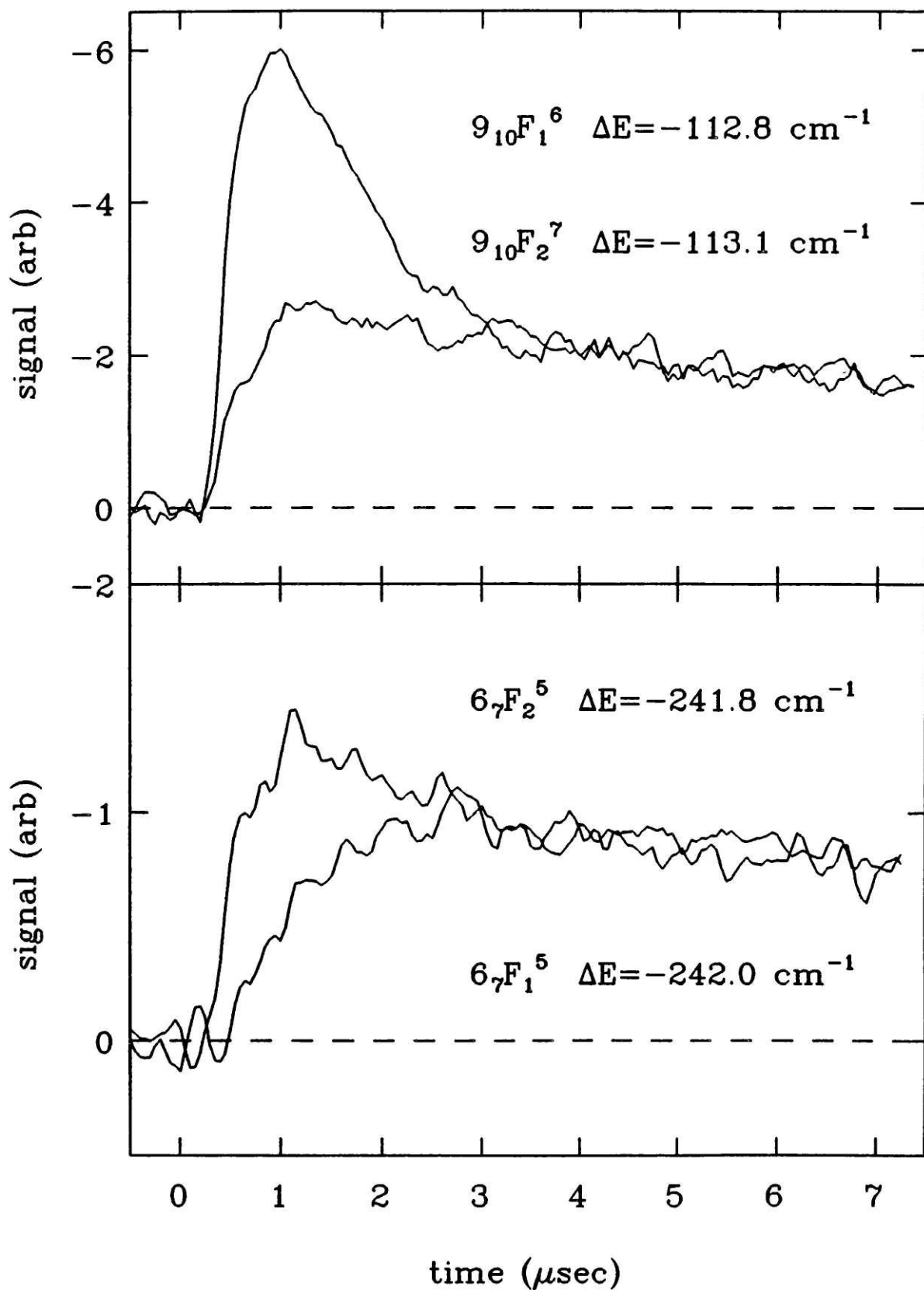
Bearing in mind the dependence of state-to-state transition probabilities on C^n, let us consider changes of the quantum numbers J and R. For given J_R in the ν_4 state, there are about R/2 fine-structure levels (of F_1 or F_2 symmetry) accessible from the initial state, F_2^7. (To be precise, the number of F-symmetry levels is R/2 for R even, and (R+1)/2 for R odd [WILS35].) For the set of levels of $J_R = 12_{12}$, we managed to obtain decay curves for all six levels C^n. These curves are shown in Fig. 4-9. We see here that the six fine-structure levels again display a variation in the rates of uptake of population. Note that there seems to be no correlation between the energy change and the apparent energy transfer rate, and that the energy gaps for the six pathways are all fairly small ($\Delta E = 32\text{-}44$ cm^{-1}). The significant result here is that none of the six pathways appears to be a principal pathway: none of the curves exhibits a large initial peak as does the curve for $(J=12, F_2^8)$ in Fig. 4-7. We can hypothesize that this contrast is related to the R quantum numbers of the levels. The level $(J=12, F_2^8)$, like the initial level, is in the F^+ Coriolis sublevel, and thus has $R = 13$; the six levels of Fig. 4-9 are all of $R = 12$. For the principal pathway ($11_{12}F_2^7 \rightarrow 12_{13}F_2^8$), we have $\Delta(R - J) = 0$; for the secondary pathways in Fig. 4-9, we have $\Delta(R - J) = -1$.

For the set of levels with $J_R = 12_{11}$ (in the F^- Coriolis sublevel of ν_4), we again obtained decay curves for all six fine-structure levels. These are shown in Fig. 4-10. Again, we find no principal energy transfer pathways; for transfer to these levels, we have $\Delta(R - J) = -2$. By comparing Fig. 4-9 with Fig. 4-10, in fact, one can see that $\Delta(R - J) = -2$ transfer appears to proceed with a lower rate than transfer via $\Delta(R - J) = -1$. From the whole set of our data for transfer from $(J=11, F_2^7)$ to $(J=12, C^n)$, we see that principal pathways occur only for $\Delta(R - J) = 0$. In the notation of the Coriolis sublevels, these pathways are denoted $F^+ \rightarrow F^+$.

Figure 4-9: Transfer to the $J_R = 12_{12}$ levels (F^0 Coriolis sublevel)

(next page)

Pressure: 200 mTorr $^{13}CD_4$

Figure 4-10: Transfer to the 12_{11} Levels (F^- Coriolis sublevel)

(following page)

Pressure: 200 mTorr $^{13}CD_4$

$J_R = 11_{12}(F_2^7) \rightarrow 12_{12}$ levels

$12 \ F_2^6 \quad \Delta E = 44.3 \ cm^{-1}$

$12 \ F_1^6 \quad \Delta E = 43.8 \ cm^{-1}$

$12 \ F_1^5 \quad \Delta E = 41.7 \ cm^{-1}$

$12 \ F_2^5 \quad \Delta E = 38.3 \ cm^{-1}$

$12 \ F_1^4 \quad \Delta E = 38.2 \ cm^{-1}$

$12 \ F_2^4 \quad \Delta E = 32.1 \ cm^{-1}$

signal (arb)

time (μsec)

87

$J_R = 11_{12}(F_2^7) \rightarrow 12_{11}$ levels

12 F_2^3 $\Delta E = 19.13$ cm^{-1}

12 F_1^3 $\Delta E = 19.11$ cm^{-1}

12 F_1^2 $\Delta E = 17.8$ cm^{-1}

12 F_2^2 $\Delta E = 17.3$ cm^{-1}

12 F_1^1 $\Delta E = 16.9$ cm^{-1}

12 F_2^1 $\Delta E = 16.7$ cm^{-1}

signal (arb)

time (μsec)
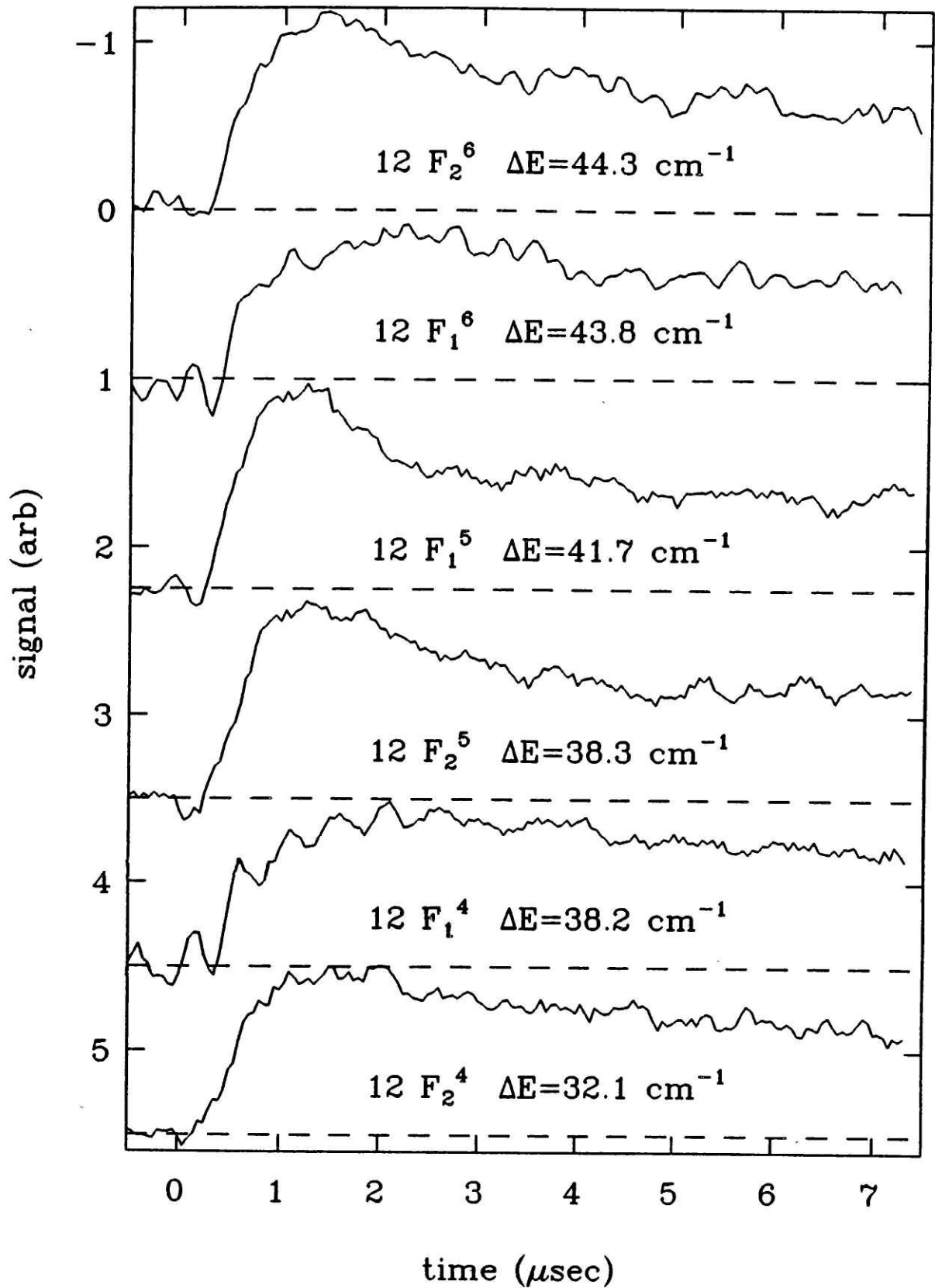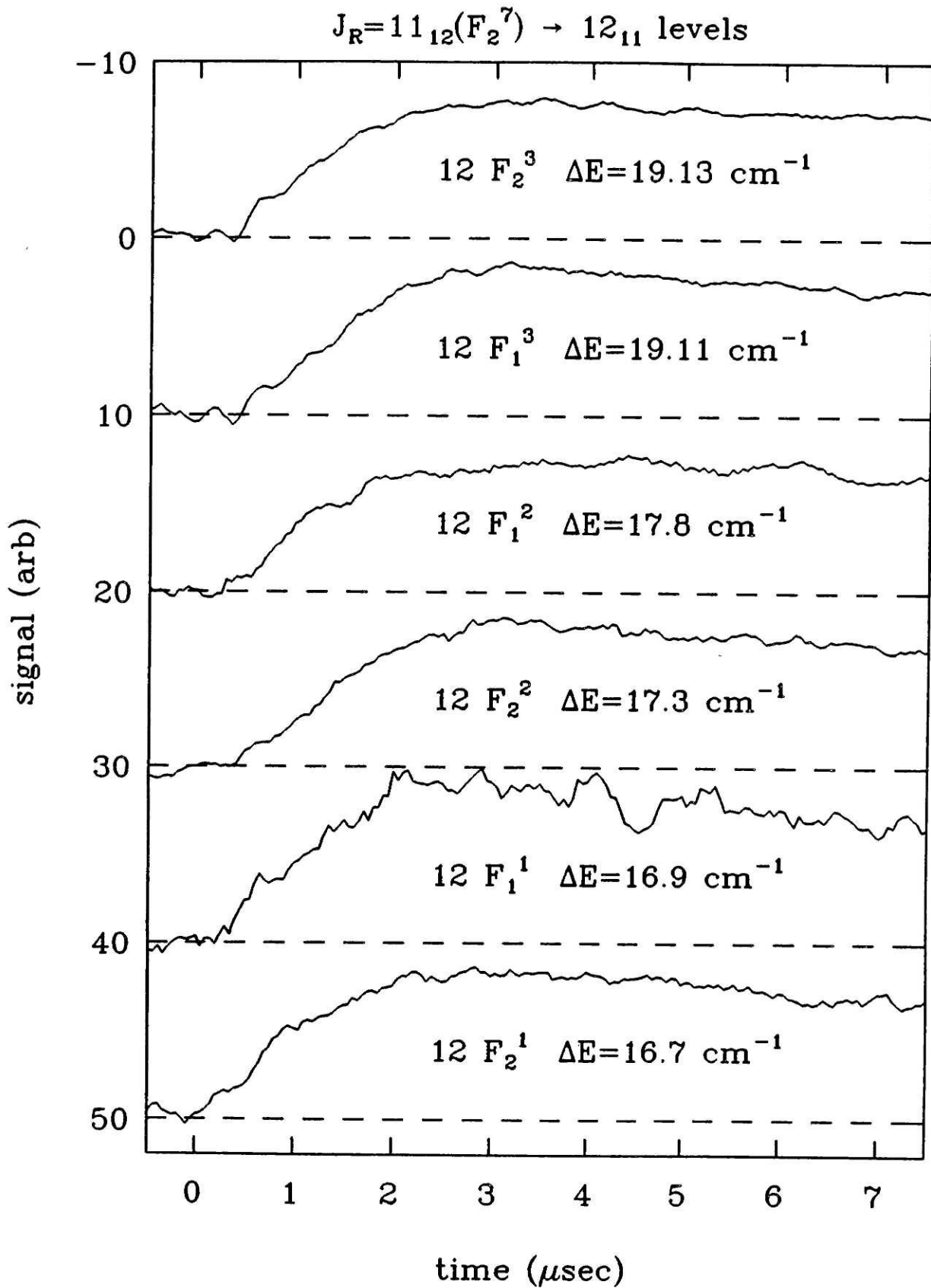
This conclusion seems to be supported by our observations for other levels of J_{final}. In the many pathways that we monitored to the F^0 and F^- Coriolis sublevels for $\Delta J \neq 0$, all were found to be secondary pathways. There is, however, a notable exception for $\Delta J = 0$. This is transfer to the level $(J=11, F_2^5)$, which falls in the F^0 Coriolis sublevel. For this $\Delta(R-J) = -1$ transition, the rate of transfer appears to be equally as rapid as for the principal pathways of $\Delta(R-J) = 0$. Figure 4-11 shows the evidence, along with decay curves for other $\Delta J = 0$ pathways. For the transition to $(J=11, F_2^5)$, we have $\Delta J = 0$, and the symmetry species remains the same (F_2). It is interesting to note that in the spectroscopic analysis, these two levels are in the same block of the Hamiltonian matrix, which is block-diagonal in the quantum labels J and C. In Chapter 5, we will explore the possible consequences of this connection with regard to the quantity $\Delta(R-J)$. All of the other $\Delta J = 0$, $\Delta R \neq 0$ pathways that we were able to monitor appear to be of secondary importance, as one can see in Fig. 4-11. The $\Delta J = \Delta R = 0$ pathway to $(J=11, F_1^7)$ is a principal pathway.

Figure 4-11: Transfer to Various J = 11 Levels (F^+, F^0, F^- Coriolis sublevels)

(next page)

Pressure: 200 mTorr $^{13}CD_4$

$$J_R = 11_{12}(F_2^7) \rightarrow 11_R(C^n)$$

$\Delta(R-J) = 0$

$11_{12}F_1^7 \quad \Delta E = -4.9 \ cm^{-1}$

$\Delta(R-J) = -1$

$11_{11}F_2^5 \quad \Delta E = -18.5 \ cm^{-1}$

$11_{11}F_2^4 \quad \Delta E = -20.7 \ cm^{-1}$

$\Delta(R-J) = -2$

$11_{10}F_1^2 \quad \Delta E = -42.7 \ cm^{-1}$

$11_{10}F_2^2 \quad \Delta E = -42.8 \ cm^{-1}$

signal (arb)

time (μsec)
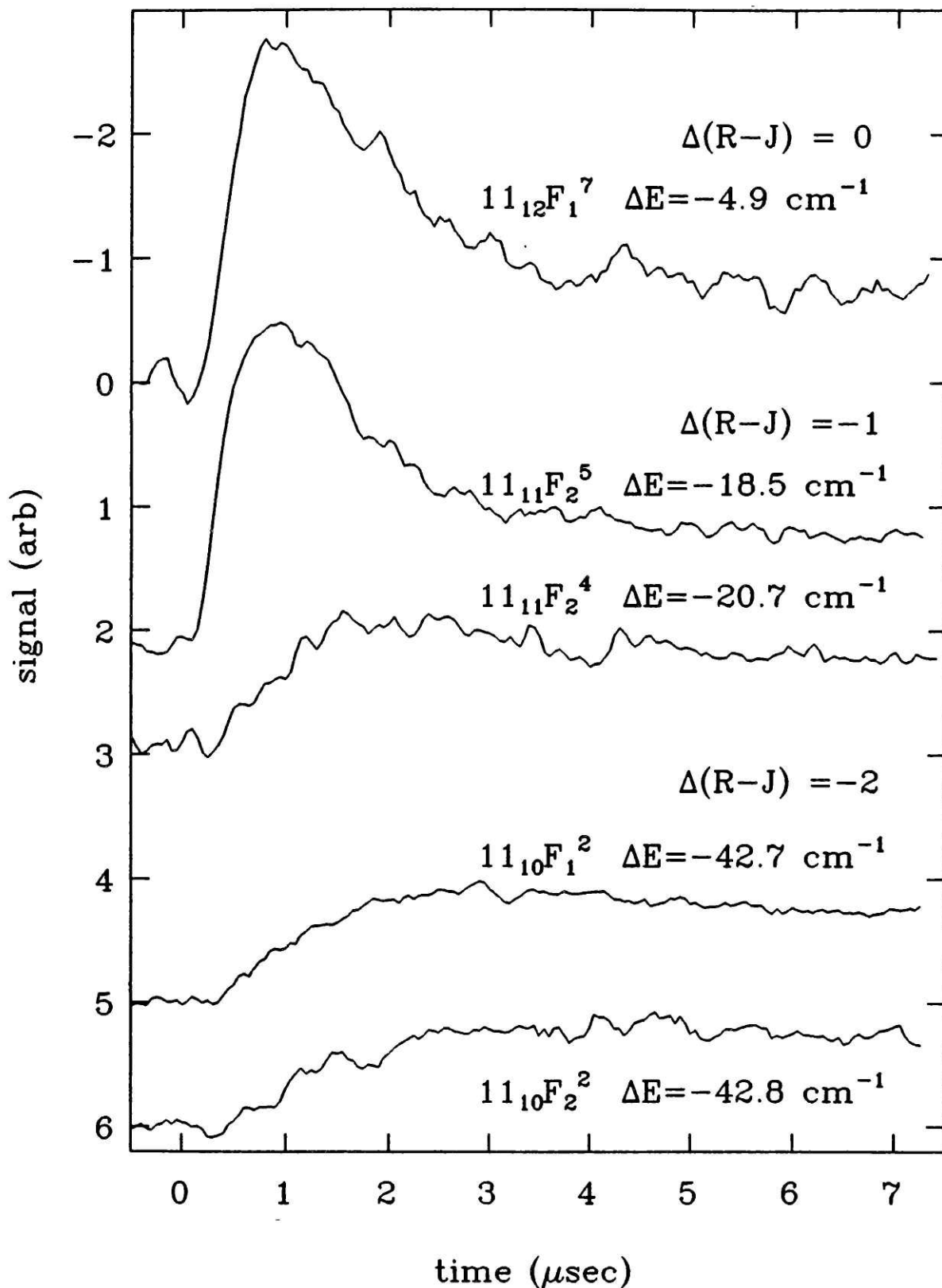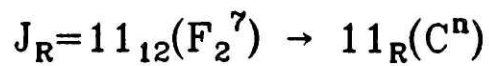
Now let us consider the overall trend for the energy transfer rates as a function of the change of J. We have mentioned that the principal channels for population transfer seem to be concentrated among the $F^+ \to F^+$ transitions, and that even within that subset of possibilities, there is a wide range of rates for final levels of different C^n. Thus, if we wish to assess the effect of increasing ΔJ on the energy transfer rate, we should confine our attention to those pathways judged to be the principal ones. The data we obtained indicate that there is a fairly pronounced distinction between the principal and secondary pathways, so there are no uncertainties about which to choose for this comparison. Of the 63 total pathways that we monitored (see Table 4-1), we determined that 7 are principal relaxation channels, as designated in Table 4-1; six of the 7 have $\Delta(R - J) = 0$ (i.e., are $F^+ \to F^+$ transitions). Some of these decay curves are shown together in Fig. 4-12. One can see here that the initial peaks of the decay curves, which are the most sensitive indicators of the state-to-state rates, diminish in size as $|\Delta J|$ increases (from $|\Delta J| = 1$ to 5). Thus, we see the expected trend of a decreasing transition probability with increasing change of angular momentum. The kinetic model of the data, to be discussed next, will allow us to estimate how sharply the probability falls off with $|\Delta J|$.

Let us summarize the observations first. We have seen that state-to-state rotational energy transfer pathways are remarkably specific with respect to the fine-structure designations C^n of the initial and final states. It appears that the principal channels for relaxation, starting from $(\nu_4, J = 11, F_2^7)$, comprise a surprisingly small subset (about one tenth) of the allowed channels. The principal pathways seem to be of the type $\Delta(R - J) = 0$ (or $F^+ \to F^+$), with one exception. Finally, the energy transfer rate is observed to decline with ΔJ (and therefore with ΔE_{rot}) for the principal pathways.

Figure 4-12: Principal Relaxation Channels at 200 mTorr $^{13}CD_4$

(next page)

The smooth curves are the results of the kinetic model discussed in the text.

Principal channels from $11_{12}F_2{}^7$

$12_{13}F_2{}^8$ $\Delta E = 62.4$ cm^{-1}

$11_{12}F_1{}^7$ $\Delta E = -4.9$ cm^{-1}

$9_{10}F_1{}^6$ $\Delta E = -113$ cm^{-1}

$8_9 \ F_1{}^6$ $\Delta E = -160$ cm^{-1}

$6_7 \ F_2{}^5$ $\Delta E = -242$ cm^{-1}

signal (arb)

time (μsec)
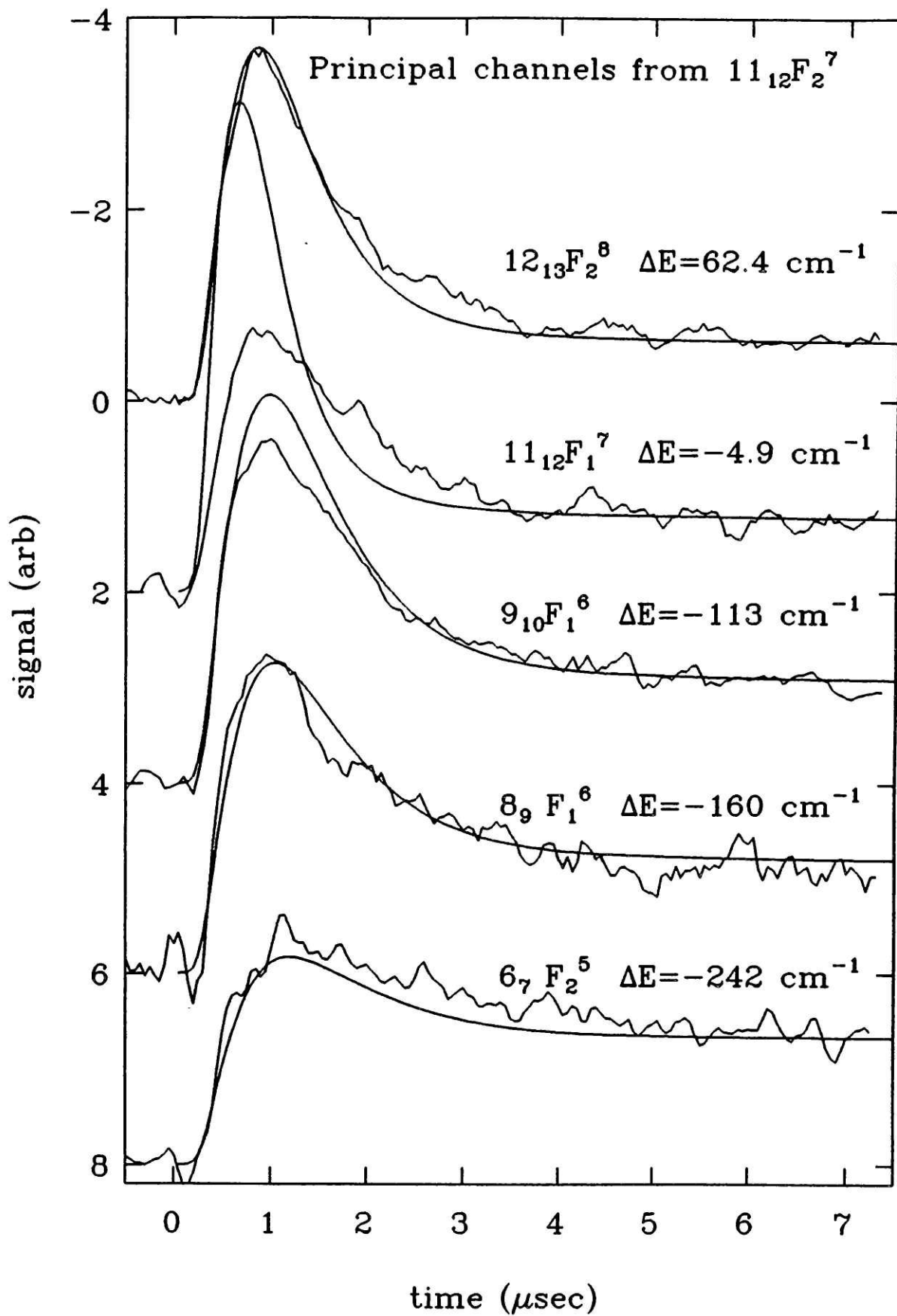
4.4.2 A Simple Kinetic Model

Since we have now established a qualitative framework for the interpretation of the state-to-state rotational energy transfer data, we can attempt to obtain quantitative measures of the individual rate constants that determine the form of the population evolution curves. It is essential to remember that experimental conditions are such that multiple collisions give rise to the observed signals. The sensitivity of our experiment (when done on this particular molecule) is not high enough to allow us to measure relaxation times on the time scale of only one mean gas-kinetic collision interval; that would require reducing the pressure (and thereby the collision frequency) by an order of magnitude. Under our conditions, a given rotational level can acquire population through direct transfer from the initially excited level, or by a sequence of collisional transitions through n intermediate steps, although the contribution made by an n-step pathway diminishes rapidly with n. Multiple-collision effects lead to ambiguities, since the combination of two highly probable collisional transitions can have an effect similar to a single-collision transition that proceeds with low probability. For example, a level within $J_R = 12_{12}$, whose decay curves are represented in Fig. 4-9, might gain population through any of these channels:

$$(J_R = 11_{12} \ F_2{}^7) \quad \xrightarrow{k_1} \quad (12_{12})$$

$$(J_R = 11_{12} \ F_2{}^7) \quad \xrightarrow{k_{2a}} \quad (12_{13} \ F_2{}^8) \quad \xrightarrow{k_{2b}} \quad (12_{12}) \qquad k_{2a} >> k_1$$

$$(J_R = 11_{12} \ F_2{}^7) \quad \xrightarrow{k_{3a}} \quad (11_{11} \ F_2{}^5) \quad \xrightarrow{k_{3b}} \quad (12_{12}) \qquad k_{3a} >> k_1$$
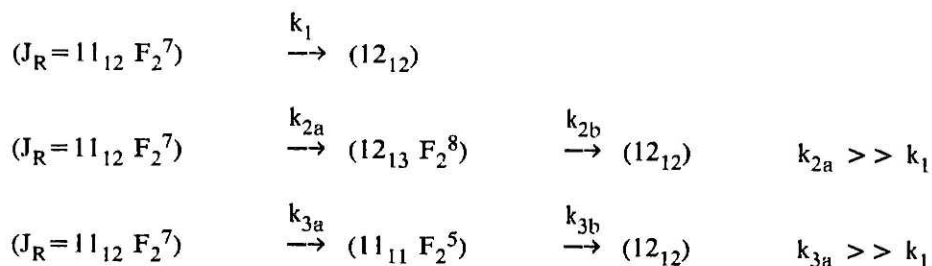
In the two indirect pathways, we know that the first steps are "fast;" they are principal pathways. If the second steps were similarly fast, it would prove difficult to determine the slow direct-transfer rate constant k_1. Due to the abundance of individual levels that are energetically accessible, there are many conceivable multiple-step pathways between a given pair of states. Of course, the presence of fast steps between two levels remote from the initial level cannot be determined except by measurements using one of these levels as the initial level. The experimental limitations that we outlined before do not permit a systematic study of this sort.

This is a problem frequently encountered in collisional energy transfer studies in complicated multi-level systems. The usual course of action is to implement a Master Equation approach, which takes into account population transfer between remote levels [BENSH81]. This allows us to simulate the effects of mutiple collisions. In general, the equation for the rate of change of population of level i (i = 1,...,L) can be written:

$$\dot{N}_i = \sum_{\substack{j \neq i}}^{L} k_{ij}N_j - \sum_{\substack{j \neq i}}^{L} k_{ji}N_i$$

$$= \sum_{\substack{j \neq i}}^{L} k_{ij}N_j - N_i \sum_{\substack{j \neq i}}^{L} k_{ji}$$

$$= \sum_{\text{all } j}^{L} k_{ij}N_j \ , \qquad k_{ii} = -\sum_{\substack{j \neq i}}^{L} k_{ji}$$

where k_{ij} is the rate of transfer of population from level j to level i. The depopulation rate of level i, k_{ii}, is related to the rates of transfer of population into the level by the conservation criterion:

$$k_{ii} = - \Sigma_j \ k_{ij}$$

In matrix notation, we write the Master Equation as

$$\dot{N} = K \cdot N(t) \tag{4.2}$$

where N(t) is a vector of level populations and K is a matrix of rate coefficients. The solution of the coupled differential equations gives us the evolutions of the individual level populations. In the equation for the pumped level, we add a term to account for the time-dependent introduction of population by laser pumping:

$$\dot{N}_p = \Sigma \ k_{ij}N_j + \alpha I(t)$$

where I(t) is the temporal profile of the pump-laser pulse, and α is an appropriate proportionality constant. Note that this allows us to account for collisional transitions occurring during the laser pulse. This is an essential feature of the model, since the measured decay curves show that significant population accumulates in neighboring levels before the pulse has subsided. For the pulse profile, we use the dashed curve of Fig. 4-6b, obtained with the limited time resolution of the probe-laser detection system. In this way, we incorporate the effect of the limited instrumental frequency response on the appearance of the decay curves. These measures are essential in extracting accurate quantitative data from the experimental measurements.

A formidable obstacle arises when implementing Eq. 4.2, namely that the number of individual rovibrational levels in the system is so large. For J = 0 to 20 in the methane dyad, there are 551 levels of F symmetry to be included in the calculation. If we restrict the calculation to rotational levels of ν_4, we still have 331 levels. The rate matrix K for the system then contains $331(331-1)/2 = 54,615$ independent state-to-state rate constants. (Forward and reverse rate

constants for a given pair of levels are related by the principle of detailed balance.) These rate constants must be determined by comparison of the numerical solution of the set of coupled differential equations with the experimentally measured curves for all of the levels. Such a comparison is not possible with our data, since we could not monitor all of the rotational levels in the system; even if we could, though, the refinement of rate constants would require a lot of work on the old slide rule. One possible simplification is obtained if we use a scaling law to determine the state-to-state rate constants, under the assumption that the rate constants are scaled in a simple way with the change of energy or angular momentum. The commonly used scaling laws, such as the exponential energy gap law, can be parametrized in a simple expression and adjusted to achieve a satisfactory reproduction of the data [BRUN82].

But we still have the problem that we cannot compare the calculation with observed data for every accessible energy level. Another simplification is suggested by the similarity of many of the decay curves, as the data for $J_R = 12_{11}$ in Fig. 4-10. We can approximate the large system of levels by grouping together some of them, and treating the groups as single units in the calculation. This would seem to be appropriate especially for groups of levels to which there are only secondary channels for population transfer. Since it is difficult to model realistically the slow uptake of population in these levels via a large number of simultaneous multiple-step pathways, the grouping procedure allows us to include the levels in the calculation but to treat them in an effective way.

A different problem arises in conjunction with an experimental difficulty. The magnitude of the observed signal is proportional to the population of the probed level as a function of time, but signal magnitudes for different levels are not comparable to each other on a meaningful basis. This is a result of instrumental fluctuations, especially those associated with the probe laser. When the diode laser is tuned from one spectral region to another (i.e., tuned to different scan modes), the intensity, spot size, shape, and spatial location of the beam all change in unpredictable ways, affecting the size and shape of the region of overlap of the two lasers. The laser linewidth and frequency stability also vary to some extent. The problems are compounded by fluctuations of the pump-laser intensity. It would be a nearly hopeless task to account for all of these variations in order to compare signal intensities for different decay curves. We should also mention that the intensities of the probed transitions have a rotational-state dependence that has not yet been mapped out with high accuracy. This introduces proportionality factors relating each signal intensity to a population; the relative magnitudes of the factors are known only to ~10%.

Fortunately, there is a way to proceed without needing to refer to the absolute magnitudes of the decay curve signals. A careful look at the decay curves in Figs. 4-7 to 4-12 reveals that all of them appear to reach a nearly constant level after a period of 8-10 μsec. In fact, when we record data on long time scales, we can see that all of the curves have a slowly decaying component lasting many tens of microseconds that is very similar for each probed level. A logical physical explanation for this behavior is that the total population of the ν_4 levels achieves rotational equilibration within ~10 μsec at a pressure of 200 mTorr of $^{13}CD_4$. Following this, slow decay processes cause a gradual, homogeneous decline of rotational level populations. These slow processes are probably a combination of V-V relaxation, V-T relaxation, and simple diffusion of excited molecules away from the viewing region. If we accept the assumption of quasi-equilibration, then we expect that rotational levels are eventually brought to relative populations determined by the Boltzmann distribution. Then the levels $(J=12\ F_2{}^8)$ and $(J=12\ F_1{}^8)$ of Fig. 4-7 should reach nearly equal populations, since their Boltzmann factors are virtually identical. This assumption was made in plotting all of the data of Figs. 4-7 to 4-12. When decay curves for levels of similar Boltzmann factors were compared, we scaled the intensities arbitrarily so as to match up the decay curves at long time scales. The validity of this assumption was checked in a few exceptional cases when experimental conditions permitted a direct comparison of two signal intensities. This happens only when two probe transitions happen to fall next to each other, so that the diode laser characteristics change only negligibly when tuning between them. We found in these cases that the assumption of rotational equilibration on long time scales was justified.

With a cautious awareness of all of the difficulties mentioned above, we set up a model system of energy levels with which to perform a kinetic analysis of the data. Our goal was to obtain a set of rate constants for state-to-state energy transfer along the principal relaxation pathways from the initially pumped level. We adopted a simple model that would replicate some (but not all) of the features of the data. State-to-state rate constants for secondary relaxation channels, in particular, are difficult to model because of the ambiguities of multiple-collision effects, so they must be treated in an effective way. But we can hope to obtain an accurate estimate of the dependence of the collisional transition probabilities on the change of angular momentum, as embodied in the data of Fig. 4-12.

The model system of energy levels is derived from the realization that the principal relaxation channels comprise only a small subset of the possible channels. In general, we can group together the fine-structure levels with specified J_R values. This clearly would not be realistic for the F^+ Coriolis sublevel, however, where we detected selective transfer to particular levels within J_R

96

groups. Thus, we treat individually one fine-structure level from each J_R group of the F^+ sublevel. The pumped level ($J = 11$ $F_2{}^7$) is also treated individually, of course. The effect of this grouping scheme is that the 331 total levels for $J = 0 - 20$ are condensed into 79 distinct states, all of which can now be included in the master equation calculation. It is important to include a large enough number of levels so that the total population can eventually be dispersed in the right proportions determined by the Boltzmann weighting factors.

State-selective population transfer is incorporated in the model by a suitable choice of the elements of the rate matrix **K**. We treated the redistribution of population within the F^+ Coriolis sublevel in the following approximate way: the initially pumped level first transfers population to one specific level of each J_R group (namely, the level we have isolated from its parent group); let us denote these levels F^{+*}. Then these levels in turn transfer population rapidly to the remaining levels of their parent J_R groups. The redistribution is thus modelled as a stepwise process, with selectivity inherent in the first step. The last step is transfer to all the J_R groups of the other two Coriolis sublevels, F^0 and F^-. We neglect direct transfer from the levels F^{+*} to other J_R groups. This is probably a drastic approximation, but we expect these rates to be small. Since it is difficult to estimate exactly how small they are, we set them equal to zero. Another important approximation we use is that for a given final J_R group, we assume there is a principal channel only to one C^n sublevel. Actually, there may be more, but we detected at most one channel, so we use only one in the model. Additional experiments are needed to clarify this important point.

We used the exponential energy gap law to compute the state-to-state rate constants [BRUN82]. This particular scaling law was chosen for the purely pragmatic reason of simplicity. The rates for downward transfer are given by:

$$k_{fi} = (2J_f + 1) \, k_0 \exp[-C(E_i - E_f)/k_B T]$$

where k_0 and C are parameters to be determined. The rate constant is weighted by the M_J degeneracy of the final level, under the implicit assumption that all final M_J states are equally accessible. Upward rates are calculated from detailed balance. For transfer to a group of levels J_R, we weight k_{fi} with the number of levels in the group to achieve the proper balance of populations at equilibrium. In the special case of transfer from the F^{+*} levels to their respective J_R groups (i.e. $\Delta J = \Delta R = 0$ transfer), we use a different rate constant k_1, weighted by the size of the group. This effectively simulates rapid redistribution for these small energy changes. Rate constants for transfer between Coriolis sublevels are reduced by two parameters as follows:

$$k(F^+ \rightarrow F^0) = k_{fi}/p_1$$
$$k(F^+ \rightarrow F^-) = k_{fi}/p_2$$

Finally, we restrict the allowed changes of J by setting $k_{fi} = 0$ for $|\Delta J| > \Delta J_{max}$, with ΔJ_{max} a chosen parameter.

The master equation, Eq. 4.2, was solved numerically for the system of 79 levels by the Gear method, using a routine from the IMSL Library. We tried a number of values of the scaling law parameters and of ΔJ_{max}, judging the quality of the agreement between calculation and experiment by eye. A comparison is shown in Fig. 4-12 for the following set of parameters:

$k_0 = 0.05\ \mu sec^{-1}\ Torr^{-1}$
$C = 0.8$
$p_1 = p_2 = 5$
$k_1 = 2\ \mu sec^{-1}\ Torr^{-1}$
$\Delta J_{max} = 5$

The resulting rate constants are plotted in Fig. 4-13. The slower V-V and V-T processes and the loss of molecules from the probed region by diffusion can be effectively included by adding a small term to the depopulation rate of each level. We found, however, that this loss rate was negligibly small. In Fig. 4-14, we show experimental data for one relaxation channel taken at different pressures, and compare the results of the simulation scaled to these lower collision frequencies.

The agreement between calculated and observed curves is remarkably good for the principal relaxation pathways of $\Delta J \neq 0$ shown in Fig. 4-12. The resulting depopulation rate of the initially pumped level was checked to make sure that it agreed with the simple exponential decay rate of this level, within limits of $\sim 10\%$. This part of the agreement is not crucial, however, since our simple model includes only a restricted set of relaxation pathways from the pumped level. We adjusted rates primarily to fit the curves for the principal pathways. The very large number of secondary pathways from the initial level combine to help determine its overall depopulation rate. It is difficult to determine precisely how the total depopulation rate is apportioned among these many secondary pathways (and among the remaining principal pathways that we have not detected), so must be willing to tolerate a small discrepancy here. On the other hand, there is a serious discrepancy for the level $(11_{12}\ F_1^{\ 7})$, which lies close in energy to the initial level. We take this to represent an inadequacy of the model: the rate of transfer to this group is overestimated in order to act as the primary depopulation route for the pumped level (i.e., k_1 is artificially large). A more detailed model that included a larger number of relaxation channels from the F^{+*} levels would probably lead to better agreement. but the limited scope of our data does not offer a sufficiently stringent test of more detailed models.

$$k(11_{12}F_2{}^7 \rightarrow J_{J+1}C^n)$$
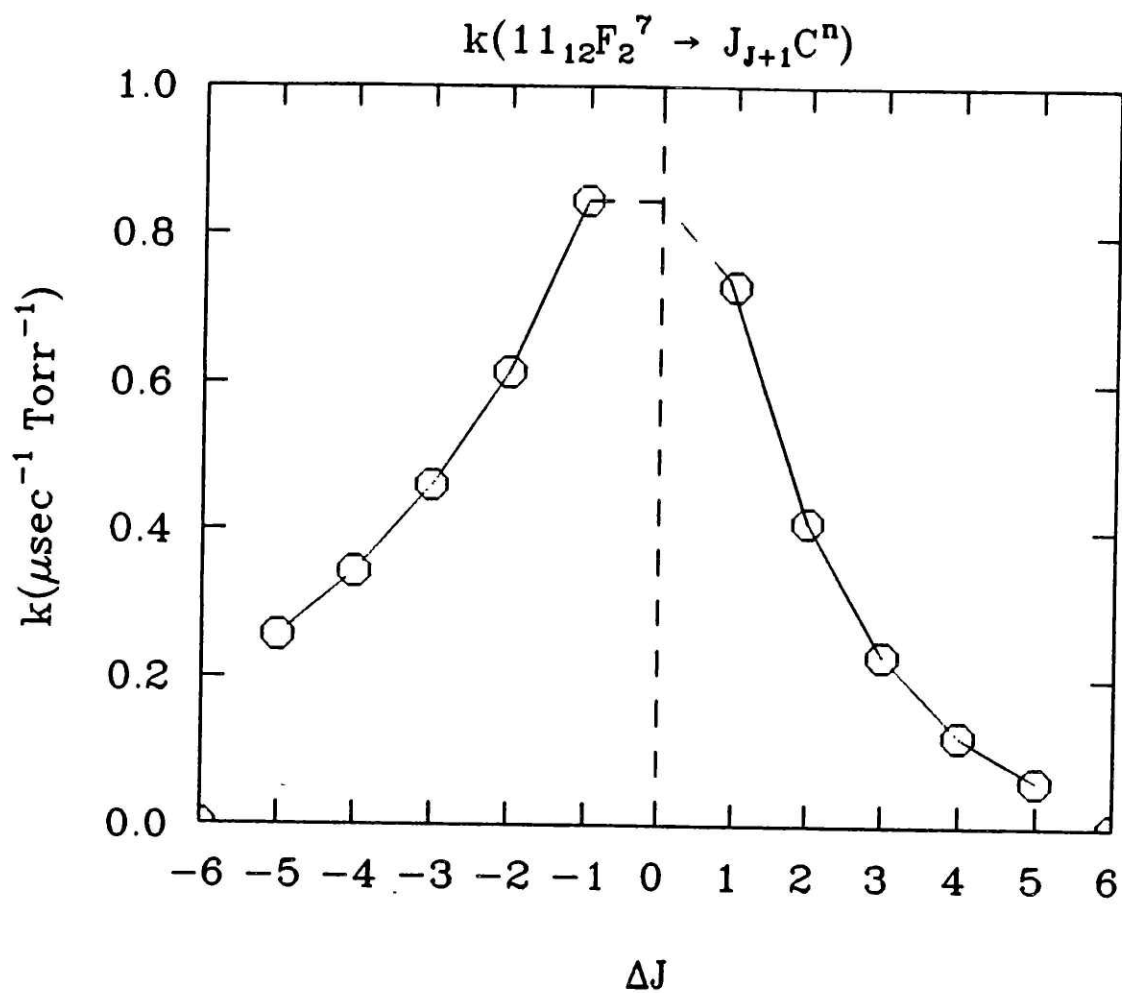
Figure 4-13: State-to-State Rate Constants for Principal Channels

Used in the kinetic model discussed in the text.

99
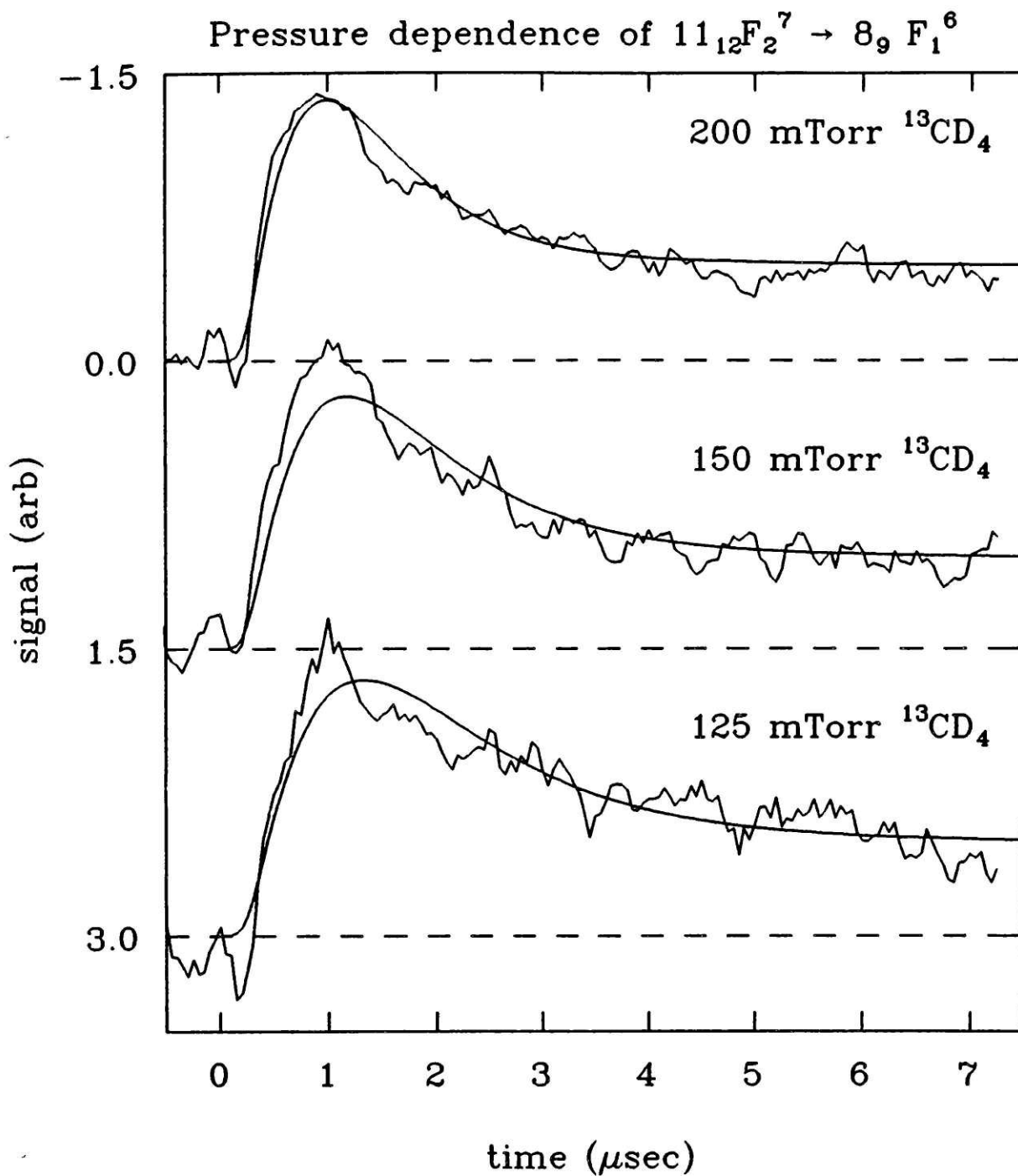
Figure 4-14: Transfer to $8_9 \, F_1{}^6$ at Different Pressures

The smooth curves are the results of the kinetic model.

The parameters p_1 and p_2, which govern transfer between Coriolis sublevels, are somewhat difficult to refine, as the calculation is not very sensitive to them. They simply control the underlying shifts of the population distribution among the large set of levels not populated by direct transfer from the initial level. Still, our calculation permits rough estimates of the relative rates of transfer between the sublevels: the transitions $(F^+ \to F^0, F^-)$ are less probable than transitions $(F^+ \to F^+)$ by a factor of 3 to 5. Note, however, that in our simple model we have ignored the single highly probable channel of the type $(F^+ \to F^0)$, displayed in Fig. 4-11. This is the pathway $(11_{12} \ F_2^7) \to (11_{11} \ F_2^5)$. For this pathway, the rate does not seem to be reduced, as we have assumed in using the parameter p_1. A more accurate estimate of the parameters p_1 and p_2 must await a more exhaustive set of data on the relaxation channels between the Coriolis sublevels. For example, it is conceivable that for each level of the F^+ Coriolis sublevel, there is a highly probable channel $(F^+ \to F^0)$ of $\Delta J = 0$, similar to the one that we have detected. This would require a more sophisticated kinetic analysis than we have attempted.

We felt that it would not be helpful to optimize the parameters of the scaling law by a least-squares refinement. The comparison between calculation and experiment is limited to a small subset of the total number of possible pathways, so that a least-squares analysis would not be a meaningful test of the entire rate matrix $\mathbf{K}$. A more detailed treatment would require the observation of population evolutions for all of the accessible rotational levels within some 300 cm^{-1} of the initial level. Our partial survey of the system, however, captures the flavor of the complex pattern of pathways involved. The important result of the analysis is the deduced dependence of k_{fi} on ΔJ for methane-methane collisions, shown in Fig. 4-13. This is the first such determination for self-collisions of a spherical-top molecule. It demonstrates unequivocally that large changes of the angular momentum of the molecule can occur in single collisions with significantly high probability.

Chapter Five
Discussion and Conclusions

In this chapter, we will review the experimental results from Chapters 3 and 4 with an emphasis on the unique features of collisional relaxation in methane as compared with other small polyatomic molecules. We will consider some previous work on energy transfer in methane so as to clarify what new features have been revealed by our approach. The spherical tops are a peculiar class of molecules because of their high symmetry. As we have seen, they are capable of displaying some rather eccentric collisional behavior, perhaps unforeseen by many in the field of energy transfer. We do not profess to be in complete command of these peculiarities, but we can speculate about their origins, using as a guide the wisdom gained from the broad range of experience provided by energy transfer in other molecules.

5.1 Total Depopulation Rates

In Chapter 3, we measured the total rate of transfer out of the level $(\nu_4, J=11, F_2^7)$ to all possible final levels. We found that the effective rotational relaxation cross section, σ_{rot}, is on the order of the Lennard-Jones cross section for methane — rare-gas collisions. For self collisions, σ_{rot} is ~35% larger than the Lennard-Jones cross section. It is interesting to compare this result with depopulation cross sections for self-collisions of other small polyatomic molecules. A few representative examples are shown in Table 5-1. It is quite evident here that polar molecules have rotational relaxation cross sections that are generally much higher than σ_{LJ}, in stark contrast to the non-polar molecules methane and SF_6.

Table 5-1. A Sampling of Depopulation Cross Sections.

	σ_{rot}	σ_{LJ}	Ref.
$^{13}CD_4$	67 Å^2	50 Å^2	this work
CDF_3	300 Å^2	99 Å^2	[HARR84]
H_2CO	500 - 700 Å^2	99 Å^2	[TEMPS87]
SF_6	140 Å^2	140 Å^2	[DUBS82]

This contrasting behavior is perhaps not very surprising when we consider the intermolecular potentials relevant to the different species. Strongly polar molecules interact via the mutual forces exerted by the permanent molecular dipoles. Studies of state-to-state rotational relaxation in these molecules have shown that the dipole-dipole interaction plays a dominant role in determining the outcome of the collision [OKA73]. This is seen most convincingly by the observed "propensity rules" for the change in angular momentum quantum numbers. Collision-induced transitions generally follow these rules less strictly than, for example, selection rules for optical transitions. Experiments on the symmetric tops NH_3 [OKA68] and CDF_3 [HARR84] revealed that in self-collisions, there are strong preferences for changes in J and K as follows:

$$\Delta J = 0, \pm 1; \quad \Delta K = 0.$$

These were interpreted as "dipole-type" propensity rules because of their resemblance to selection rules for electric dipole transitions. In experiments on H_2CO [TEMPS87], the preferred pathways were found to be

$$\Delta J = \pm 1; \quad \Delta K_a = 0; \quad \Delta K_c = \Delta J.$$

Similar results were found for D_2CO [ORR84]. Careful analysis of the results, using treatments similar to our kinetic analysis in Chapter 4, indicated small probabilities for pathways of $\Delta J = 2$ and 3, in both H_2CO and D_2CO. This was ascribed to the higher-order effects of the dipolar interaction, and possibly to the contributions of quadrupolar and other mutipolar interactions, which would induce higher changes in J. The implications of the multipolar expansion of the intermolecular potential have been treated in an indispensable review article by Oka [OKA73], in which the reasoning in the above remarks is explained fully.

We might attempt to apply the same line of reasoning to methane. In this molecule, the lowest-order permanent multipole moment allowed by T_d symmetry is the octupole moment. The leading term in the multipolar expansion is the octupole-octupole interaction. The potential energy of this interaction varies with distance as r^{-7}, while the dipole-dipole interaction varies as r^{-3}, so we expect the octupolar interaction to be of much shorter range (provided the coefficient of the octupole-octupole term is not too large). Therefore, on the basis of these admittedly simple considerations, we expect that the inelastic cross section for octupolar molecules such as methane should be smaller than that for dipolar molecules, other things being equal.

Oka demonstrated that the octupole-octupole interaction leads to quantum number changes as follows:

$$\Delta J = 0, \pm 1, \pm 2, \pm 3; \quad \Delta M = 0, \pm 1, \pm 2, \pm 3; \quad \text{parity} + \leftrightarrow -. \tag{5.1}$$

103

Our state-to-state energy transfer measurements of Chapter 4 provided a test of these propensity rules. Before we discuss that in detail, though, we should consider the limitations of the simple argument above. We must realize that for an interaction of short range (or small cross section), the multipolar expansion of the intermolecular potential converges very slowly. Oka uses the term "strong collision" for this case; collisions governed by long-range interactions are "weak" collisions. For strong collisions, many terms in the expansion of order higher than the octupole term must be considered. In addition, we must consider the effects of the non-permanent multipole moments (induction and dispersion interactions). The large set of terms thus included will allow a variety of changes in J to occur, including $\Delta J > 3$. So we should not expect propensity rules to apply that are as simple as the expression above, Eqn. 5.1. Nor should we expect to be able to make a direct connection between given changes of J and R and specific terms in the perturbation expansion. These are reflections of the fact that the perturbation treatment of the collision is not valid in the case of methane. This is perhaps unfortunate, for the perturbation treatment has been demonstrated to be successful in the interpretation of an extensive body of work on energy transfer in polar polyatomic molecules. The treatment of collisional behavior in light spherical tops requires theoretical approaches that are in this sense new and possibly more involved.

The measurement of an effective rotational relaxation cross section can of course be accomplished by traditional techniques that are far older than IRDR. In Appendix 2, we discussed a comparison between our depopulation cross section measurements and the results of ultrasonic techniques. The ultrasonic dispersion method yields a measure of the relaxation rate averaged over all of the thermally populated rotational levels. The rate must be deduced by a complicated deconvolution of the data, whereas IRDR yields a direct time-domain measurement of population changes. In the comparison of the results of the two approaches, large discrepancies were found, particularly in the trends of cross sections $\sigma_{rot}(^{13}CD_4 - M)$ versus the mass of the collision partner, M. The source of these discrepancies is not known, but their existence warrants a cautionary statement. A great many experimental techniques yield effective measures of relaxation rates that are often identified as "rotational relaxation rates;" but when interpreting these rates, one must be aware that they depend on the details of the physical behavior associated with the measurement. This is true especially when relaxation rates from the literature are used in modelling complex kinetic systems, such as Infrared Multiple Photon Excitation (IRMPE). The IRMPE literature contains examples of misuse of measured relaxation rates that probably invalidate the models used [TOSE86].

Another traditional measure of rotational relaxation cross sections that has been applied to methane is pressure broadening of spectroscopic transitions. Pressure-broadening parameters, $d\gamma/dN$, bear a close relationship to the total depopulation rates of the levels of the monitored transition. The difficulty with this relationship resides in the sensitivity of the spectroscopic linewidth to *every* process that interrupts the radiative interaction. Hence, in order to deduce that component of $d\gamma/dN$ that corresponds to the simple removal of population from a level, one must carefully assess the other conributions. (These other contributions, in infrared and Raman transitions, include vibrational and rotational dephasing in elastic collisions, and velocity-changing collisions, which can lead to Dicke narrowing.) An additional complication in $d\gamma/dN$ is that it contains contributions from relaxation occurring in both levels of the transition. Still, we find our total depopulation cross section to be roughly in agreement with a preliminary pressure-broadening coefficient for $^{13}CD_4$ of $d\gamma/dN = 0.084(3)$ cm^{-1} atm^{-1} (HWHM), measured for several Raman transitions in the Q(3) and Q(4) regions of ν_1 [MILLOT87]. (These regions include a few lines of $\nu_2 + \nu_4$ as well.) Using the relationship [TOWN55]

$$k \equiv \sigma vN = 2\pi(d\gamma/dN)$$

this converts to an effective rate constant of $21(1)$ μsec^{-1} Torr^{-1}, as compared to our measurement $k_{rot} = 16.6(3)$ μsec^{-1} Torr^{-1}. Dephasing is responsible for a part of $d\gamma/dN$, but the contribution is not yet known for $^{13}CD_4$. In CH_4, dephasing accounts for about 10% of $d\gamma/dN$ [VOLK84]. If the dephasing contribution were the same for $^{13}CD_4$, then the pressure broadening measurement would yield an estimate for the rotational relaxation rate that is within ~15% of our measurement. Note, however, that this value of $d\gamma/dN$ is associated with different rovibrational levels of the molecule. Pressure broadening studies in the ν_4 band of CH_4 show that individual transitions (J,C^n) have broadening coefficients that vary by as much as 40% [BALL86]. Similar variations for the ν_1 Raman transitions of $^{13}CD_4$ have been seen [G. Millot, priv. commun.], but more extensive studies are needed to deduce the range of variation. For the moment, we may conclude that the results of the IRDR and linewidth investigations are consistent within the fluctuations due to the detailed dependence of the depopulation rates on the rotational quantum numbers.

5.2 Vibration-to-Vibration Energy Transfer

A recent series of experiments on D_2CO and HDCO by Orr and colleagues indicates that Coriolis coupling between vibrational modes may influence the probability of collisional interconversion between the modes [HAUB87]. Under certain conditions, the V-V energy transfer probability may approach the very high probability of rotational state changes. Haub and Orr point

out that when the mixing between vibrational modes is large, V-V transfer can almost be considered a form of rotational energy transfer, in which the initial and final states are different only in the *balance* of vibrational character formed by the two normal modes. Our measurements on $^{13}CD_4$ did not reveal any pathways (Δv_i, ΔJ) with unusually high probabilities, although we sampled only a small number of pathways. There are probably no rotationally specific channels in the transfer $\nu_4 \rightarrow \nu_2$. Their absence can be rationalized on the basis that the "special conditions" required for their presence are not satisfied. As Orr carefully points out, Coriolis mixing by itself is not sufficient for enhancement of the V-V transfer. Other rovibrational interactions are probably also required, in order to frustrate subtle quantum-mechanical interference effects in the matrix element of the potential between initial and final states. (The reader is referred to the original discussion for further detail [HAUB87].) Also required is a small energy separation between the initial and final rovibrational states. In the dyad levels of $^{13}CD_4$, sufficiently strong rovibrational interactions are present, but the condition of small energy separation is not met, since there is no crossing between ν_4 and ν_2, as can be seen in Fig. 2-5. Rotational levels that are directly coupled by Coriolis interaction (i.e., levels of the same J and C) are separated by a large energy gap of 90 to 140 cm^{-1}, even at high J. This energy gap is probably large enough that rotational energy transfer pathways in ν_4 are significantly faster than any V-V channels.

5.3 Changes of J in Methane-Methane Collisions

Our kinetic model of the state-to-state rotational energy transfer data indicates the occurrence of large angular momentum changes in single collisions. We found that if we constrain J-changing pathways to $|\Delta J| < 5$, then the calculated population evolutions for states of $|\Delta J| \geq 5$ do not satisfactorily agree with the observations. Actually, we can make a simple qualitative argument for direct transfer by $\Delta J = -5$ along the pathway

$11_{12}(F_2^7) \rightarrow 6_7(F_2^5)$.
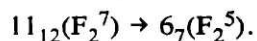
A comparison of decay curves for the two final levels $6_7(F_2^5)$ and $6_7(F_1^5)$ was shown in Fig. 4-8. These levels have decidedly different rates of uptake of population. If transfer to them occurred only by multi-step pathways, then there would have to be a sequence of highly probable steps leading to $6_7(F_2^5)$ *but not to* $6_7(F_1^5)$. A more likely explanation, the one that we endorse, is that transfer from the initial level directly to $6_7(F_2^5)$ is "allowed," while transfer to $6_7(F_1^5)$ may occur primarily through multiple-step pathways. The first step of such a pathway might in fact be to the "favored" level $6_7(F_2^5)$; the subsequent transfer to $6_7(F_1^5)$ would have $\Delta J = \Delta R = 0$, and a very small energy change, $\Delta E = -0.2$ cm^{-1}, so it might be quite fast.

It is possible that methane-methane collisions can induce transitions of even greater $|\Delta J|$. Our data for these pathways is somewhat limited, so we cannot be sure. The possibility of $\Delta J = -5$ transitions, which incur a rotational energy change greater than $k_B T$ (viz. -242 cm^{-1}), is affirmation of the considerable complexity of the interaction between molecules, as we discussed above. Such transitions are not obvious consequences of the octupole-octupole interaction, which in first order is limited to $\Delta J \leq 3$ [OKA73]. Nor can they be related directly to the dispersion interactions of range r^{-6} or r^{-7}, which are similarly limited. The collisions in which the molecule suffers so large a loss of angular momentum are probably very strong collisions in which the molecules pass at very short range. For these events, as Oka states, the usual first-order perturbation treatment of the interaction is probably not sufficient.

The only previous investigations of state-to-state rotational energy transfer in methane are crossed-molecular-beam studies of methane — rare-gas collisions [BUCK83]. These studies also revealed the occurrence of collisions of large ΔJ: in CH$_4$-Ar collisions at a collision energy of 93 meV, transitions of up to $\Delta J = 10$ were observed, amounting to energy changes of about 500 cm^{-1}. The high collision energies used in the measurements, however, lead to very strong collisions that are probably affected most by the repulsive wall of the potential. The collisions are of short duration, so we expect a wide range of possible outcomes for the angular momentum state of the molecule. The molecular beam experiments detect collisional excitation by time-of-flight analysis of the kinetic energies of the scattered particles. Thus, the measurements are limited to collision partners without rovibrational degrees of freedom that would complicate the analysis, and they will not be applicable to methane-methane collisions. In our experiments, the collisions occur at thermally accessible energies and still result in substantial changes of angular momentum. Of course, as we discussed in Chapter 3, one might expect that methane-methane collisions are more efficient in causing the larger changes of J than are methane-argon collisions, since smaller changes of the relative translational energy may take place. Thus, although both IRDR and molecular beam experiments indicate significant probabilities for transitions of large angular momentum, the transitions may occur for different reasons. In this context, it would be extremely valuable to measure state-to-state cross sections for methane-argon collisions by IRDR. These measurements might find a meaningful and instructive comparison with the molecular beam measurements.

The rate constants that we report in Fig. 4-13 show that there is a slow drop-off in rate constants for transitions of increasing $|\Delta J|$. We see that a change of $\Delta J = -5$ is only about a factor of four less likely than $\Delta J = -1$. This contrasts distinctly with deduced rate constants for polar

polyatomic molecules, as expected. Measurements in H_2CO [TEMPS87] demonstrate that state-to-state rate constants are roughly in the ratio $k(\Delta J=1):k(\Delta J=2):k(\Delta J=3) = 5:1:0.5$. Presumably, the higher-order multipolar interactions also present in H_2CO collisions induce transitions with rate constants that fall off slowly with ΔJ, as in methane. But the effects of the dipolar interactions (viz., dipole-dipole, dipole — n-pole, dipole — induced-dipole, etc.) outweigh the other effects by a great deal, so that the rate constants for large ΔJ can be deduced only in the most precise work.

One mechanism for rotational relaxation of methane in the ν_4 state that we should consider is dipolar interactions that arise from the oscillatory dipolar nature of the vibration. Molecules in the ν_4 state carry an oscillating dipole moment of ~0.1D, which is of course the reason why the ν_4 band is infrared allowed. The oscillating dipole moment can give rise to an induced moment in the collision partner molecule, and this might manifest itself as dipolar propensity rules in rotational energy transfer. This approach has been followed in treating certain problems in V-V transfer in polyatomic molecules [YARD80]. We can dismiss the argument here, though, since our observations show that transitions of $|\Delta J| = 0$ and 1 do not dominate over the larger transitions to the same extent as in collisions of polar molecules. This conclusion will be relevant also to the following discussions of collisional changes of R and C^n.

5.4 The Dependence on R and (R — J)

These experiments offered a detailed look at the role of vibrational angular momentum in rotational energy transfer. Our observations indicate that rotational relaxation in the ν_4 state of methane is selective with respect to the Coriolis sublevel of the state, which reflects the coupling between the rotational and vibrational angular momenta. We saw that most of the principal energy transfer pathways are such that ΔJ and ΔR are the same, or $\Delta(R-J) = 0$. Out of 39 pathways that we monitored with $\Delta(R-J) = -1$ and -2, only one was found to be a principal channel of transfer. We monitored 15 relaxation channels from the initial level, $11_{12}(F_2^7)$, to the levels of J = 12, for which R has the values R = 11, 12, 13. The only principal channel that we found of these 15 was to the state $12_{13}(F_2^8)$, a $\Delta(R-J) = 0$ process. *All* possible pathways to R = 11 and 12 of J = 12 were monitored, and all appear to be only secondary pathways. Thus, since most of the important energy transfer routes proceed via the quantum number change $\Delta(R-J) = 0$, there may be a "propensity rule" that favors channels of this type.

Let us consider, however, the one notable exception to this rule. It involves the final level $11_{11}(F_2^5)$, where we observed a rate of transfer as high as to principal channels with $\Delta J = 0$ and

1. This is one of two pathways we monitored of the type $11_{12}(F_2^7) \to 11_{11}$, a $\Delta(R-J) = -1$ transition. The two decay curves are displayed in Fig. 4-11. The two pathways are the following:

$$11_{12}(F_2^7) \to 11_{11}(F_2^5) \qquad\qquad \Delta E = -18.5 \text{ cm}^{-1} \qquad\qquad \text{(principal)}$$

$$11_{12}(F_2^7) \to 11_{11}(F_2^4) \qquad\qquad \Delta E = -20.7 \text{ cm}^{-1} \qquad\qquad \text{(secondary)}$$
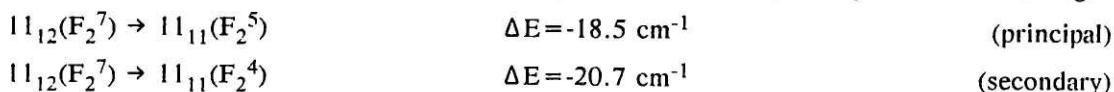
Note that both of these have $\Delta R = -1$, $\Delta J = 0$, $\Delta C = 0$ (i.e. $F_2 \to F_2$), and that they have very similar energy changes, both small. It is remarkable that two such pathways should have such different rates of transfer. To try to understand why the first pathway apparently violates the hypothesized propensity rule $\Delta(R-J) = 0$, we can make use of the insight provided by the spectroscopic characterization of the eigenstates involved. The three rovibrational eigenstates of concern here are contained in the same (J,C) block of the matrix of the rovibrational Hamiltonian. Although the two final levels have $R = 11$ and the initial level has $R = 12$, we must remember that R is mixed slightly by rovibrational interactions, as discussed in Chapter 2. The initially populated eigenstate must be written as a linear combination of states of $R = 10$, 11, and 12. Linear combinations like these for all eigenstates in the $^{13}CD_4$ dyad can be worked out systematically and accurately, since the eigenvalues (and, by deduction, the eigenfunctions) are known so well from the spectroscopic analysis. Unfortunately, the Champion-Pierre approach that we discussed in Chapter 2 does not make use of the R quantum number, so the linear combinations in R are not produced directly by the analysis. We must make a transformation between the two basis sets, which turns out to be a fairly straightforward procedure. Guy Millot has carried out the transformation between the basis actually used in the spectroscopic analysis and the more traditional "spherical basis" that includes the approximate quantum number R.

In the "spherical" basis, the wavefunctions for ν_4 states are labelled by $(J_R \ C^n)$ [HECHT60]. The rovibrational symmetry designation C is of course the same for either basis, but the index n is different. (This can lead to confusion to the unwary.) For given J_R values, we have $n = 0, 1, 2, \dots$ for levels of increasing energy. The contributions of these basis functions to the final eigenstates of the analysis are shown in Table 5-2. (Bear in mind that there are 14 total basis functions for the $J = 11$ F_2 block of the dyad matrix; 8 of them are associated with ν_4 and only these are shown here.) We see from the table that the levels $11_{12}(F_2^7)$ and $11_{11}(F_2^5)$ interact as a consequence of R-mixing terms in the Hamiltonian. (That is, the basis functions most closely associated with these eigenstates are seen to interact.) The interactions associated with the $11_{12}(F_2^7) - 11_{11}(F_2^4)$ pair are much smaller. Other levels of $J = 11$, notably $11_{11}(F_2^3)$, have varying degrees of kinship to $11_{12}(F_2^7)$. Rovibrational interactions occur in a multiple-state network, of course, not between isolated states. Some of the strong pairwise interactions, however, are clear from the detailed expansions.

Table 5-2. Eigenstate expansions in the R basis.

For the block $(J,C) = (11\ F_2)$ in ν_4. Shown are the expansion coefficients squared; for clarity, only the contributions ≥ 0.01 are included. The remaining contributions to the eigenstates are from ν_2. The underlined coefficients indicate the pattern of R mixing in the eigenstates relevant to the discussion.

Eigen function	Basis functions $(R\ C^n)$							
	$10F_2^0$	$10F_2^1$	$11F_2^0$	$11F_2^1$	$11F_2^2$	$12F_2^0$	$12F_2^1$	$12F_2^2$
F_2^1	0.96			0.01				
F_2^2		0.96		0.01		0.01		
F_2^3			0.88				0.03	
F_2^4	0.01	0.02		0.94				
F_2^5					<u>0.97</u>		<u>0.01</u>	
F_2^6		0.01		0.01		0.89		
F_2^7			0.04		<u>0.01</u>		<u>0.91</u>	
F_2^8								0.98

The pattern of R mixing that we see here could have implications for collisional energy transfer. The relaxation channel to the level $11_{11}(F_2^5)$ appears to violate the hypothesized propensity rule, $\Delta(R - J) = 0$, but we see now that the level contains a mixture of R values, as a consequence of interactions whose effects are seen in the expansion of the initially pumped state. We might propose that these effects cause a breakdown of the propensity rule for $\Delta(R - J)$. When the effects are small, as for the level $11_{11}(F_2^4)$, we do not observe a breakdown (the rate of transfer is small). Of course, we cannot ignore altogether the possibility that our propensity rule is simply formulated in too primitive a way. Additional experimental evidence for the rule would certainly be desirable. Indeed, the reader should be cautioned that the conclusions made here concerning selectivity with respect to the Coriolis sublevels are somewhat provisional, since they are derived from an incomplete survey of the energy transfer pathways.

The selective nature of collisional energy transfer between different vibrational angular momentum sublevels is a newly recognized feature of the collisional behavior of methane. We might expect this behavior to be important for other spherical-top molecules as well, although it may be modified by the details of the rotational energy level pattern. In the heavier rotors, for

example. there can be extensive overlap of levels of different J, depending on the relative sizes of the rotational constant B and the Coriolis splitting term $B\zeta$ (cf. Equations in section 2.2.2). Experiments now being conducted in our laboratory on the spherical top SiH_4 will enable us to test the generality of the behavior.

The different possible combinations of changes of J and R in collisions can be diagrammed vectorially, as we do in Fig. 5-1. Shown are three typical cases that illustrate the point. The vectorial description must be distinguished from the quantum-number description. since the expressions are not the same. Whereas $\Delta(R - J)$ has integer values, the vector notation is written $\Delta(J - R) = \Delta l$. The magnitude of the vector l is fixed (the quantum number is unity) but its orientation in the reference frame of R can change. We see from the diagram that the situation $\Delta(R - J) \neq 0$ corresponds to a rotation of the vector l, or a change of the component of l with respect to R. The propensity for $\Delta(R - J) = 0$ then amounts to a propensity to conserve the orientation of l in the molecular frame. This orientation is established by the vibrational motion of the molecule. which causes the outer atoms to undergo orbits about their equilibrium tetrahedral positions (cf. section 2.2.2). The rotation of the vector l requires a complicated alteration of the directions of the orbital motions of different atoms. The orbital motions occur at a much higher frequency (viz. the vibrational frequency) than does the rotational motion.

In a sense, the three Coriolis sublevels of ν_4 that are distinguished by values of $(R - J)$ can be considered to be *different vibrations*. This is admittedly a peculiar point of view, since the normal-mode analysis shows them actually to be members of a degenerate set. But the presence of Coriolis interaction forces us to alter our point of view, and when we introduce vibrational angular momentum, we give separate identities to the three members; this is best seen by reference to the reduced energy level diagram, Fig. 2-5. From this point of view, the propensity rule for $\Delta(R - J) = 0$ can be understood in terms of the ineffectiveness of the collision in changing the "vibrational state" of the molecule. Altering the high-frequency vibrational motion of a molecule by collision is normally expected to be more difficult than altering its rotational state. In methane, we may have a special case of this general principle in which the change of "vibrational state" involves only a small change in energy, comparable to a rotational energy change.
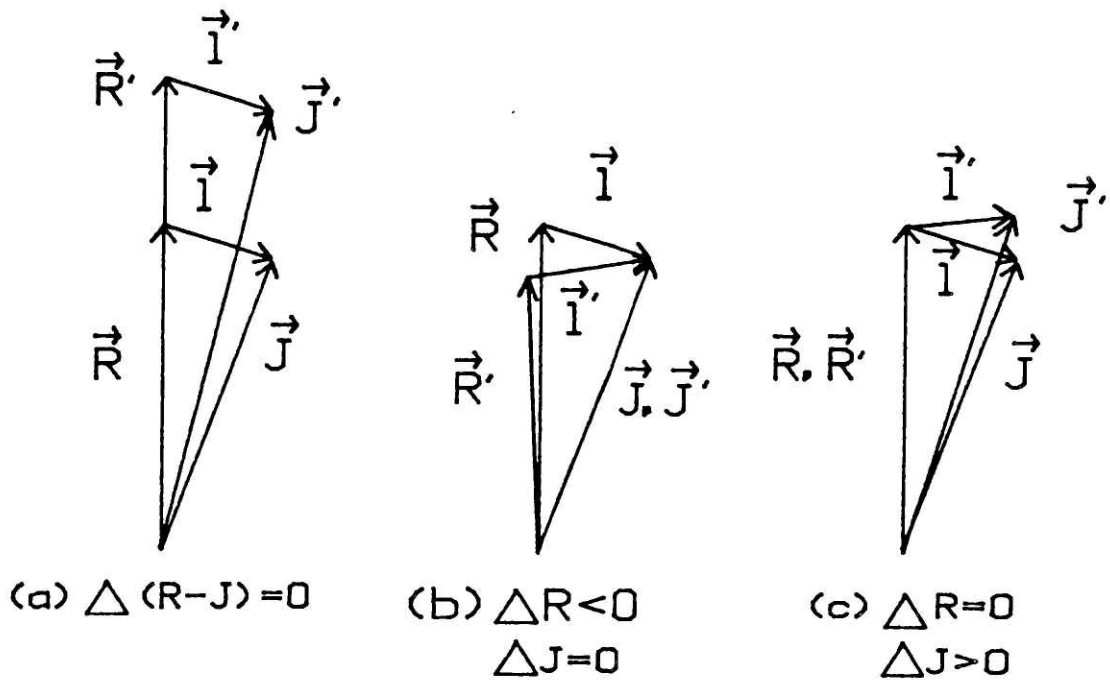
Figure 5-1: Vector Diagram of Angular Momentum Changes

The labels below the diagrams show the associated changes in the quantum numbers. Unprimed and primed vectors refer to the states before and after the collision, respectively.

Since vibrational angular momentum is a concept common to all molecules with degenerate vibrational states (symmetric-top and linear molecules), we might expect some of these considerations to affect their collisional properties as well. In symmetric tops of C_{3v} symmetry, for example, rotational levels (J,K) of a vibration of species E are split into two levels, denoted $+l$ and $-l$ by Herzberg [HERZ45]. The two levels correspond to alternative cases in which the vectors $\mathbf{k}$ and l are parallel or anti-parallel; the quantum number $l = 1$ when $v_E = 1$. Collision-induced transitions among these levels might exhibit a selectivity analogous to that seen in methane. (Some transitions, of course, are prohibited by nuclear spin selection rules.) It will be interesting to see if experimental observations bear this out.

In the case of linear molecules, there is some previous theoretical work along these lines. Clary [CLAR83] and Alexander [ALEX83] have calculated state-to-state rotational energy transfer cross sections for CO_2 in the ν_2 vibrational state, colliding with He atoms. The quantum-mechanical calculations were based on the vibrational close-coupling, infinite-order-sudden technique (VCCIOS). In the ν_2 vibrational state of CO_2, odd and even J levels are associated separately with the two states of coupling of the rotational angular momentum with the vibrational angular momentum, $l=1$. The calculations display a propensity toward collisional transitions ΔJ of the type odd $\leftrightarrow$ odd and even $\leftrightarrow$ even, implying a conservation of the state of coupling. We can interpret this as being analogous to transitions in methane in which the quantity $(R - J)$ is conserved. Recent experiments on CO_2 support some of the features of the calculation [FLYNN87]. It would therefore be most informative to extend the calculations to a treatment of methane-methane collisions. It remains to be seen, however, whether such calculations are feasible for the more complicated interaction potential.

5.5 The Dependence on C^n

The most surprising aspect of rotational energy transfer that we have observed is the degree of selectivity among the tetrahedral sublevels C^n in methane. These experiments provided the first detailed investigation of this phenomenon for any spherical-top molecule. The high-resolution nature of our experiment makes this possible. Molecular-beam scattering methods do not have the ability to distinguish the individual levels C^n within a given value of J. They measure only the total transfer to all levels with a given J. Our experiments seem to indicate that this shortcoming is of crucial importance, for the individual levels C^n are remarkably specific in their collisional properties. It may well be true that the extraction of reliable information on potential surfaces for $CH_4 - M$ interactions will be dependent on the accurate reproduction of C^n-selectivity in state-to-state energy transfer.

113

We cannot be certain at this point about the causes of the detailed selectivity. It will probably be necessary to monitor rates of population transfer to all levels in the system so that the pattern of principal pathways can be worked out in complete detail. But it is interesting to consider what characteristics of the rovibrational eigenstates might be responsible for the peculiar behavior. The tetrahedral sublevels of a given (J,R) state are somewhat analogous to the K states of a symmetric top, as we discussed in Chapter 2; the label K_R is sometimes used to reinforce this relationship [HART84]. (The projection quantum number can be referred to either the C_3 or the S_4 axes of the molecule.) Galbraith *et al.* [GALB78] have shown that when the angular momentum is large, the pattern of R mixing in the rotational eigenstates can be understood in terms of off-diagonal matrix elements of the Hamiltonian with simple selection rules on ΔK_R. Thus, the K_R description of the eigenstates underlies the discussion of R mixing that we have already considered in section 5.4. It may be possible to draw an analogy between the collisional behavior of methane and that of symmetric top molecules, similar to the analogies that exist in spectroscopic properties. We need to consider, then, the nature of the collisional energy transfer pathways among the K states of symmetric tops.

We have already stated in section 5.1 that self-collisions between polar symmetric tops lead to dipolar propensity rules for the changes of the rotational quantum numbers; $\Delta K = 0$ is the preferred pathway. Collisions of these molecules with the rare gases, however, bring out different behavior [OKA73]. The dipolar propensity rules are somewhat relaxed, and large changes of K occur. Oka found in $NH_3 - He$ collisions a remarkably well-obeyed propensity rule of $\Delta k = \pm 3n$, $n = 0, 1, 2$, for arbitrary ΔJ. This rule applies for k as a signed quantum number, $k = -J,\ldots,J$; we have $K = |k|$. (Note that for rotational levels in the ground vibrational state of NH_3 that have symmetry A, the rule $\Delta k = \pm 3n$ is mandated by nuclear spin considerations [HERZ45]. For E-symmetry levels, however, the spin-allowed transitions can have $\Delta k = 1, 2, 3,\ldots$. The propensity rule was deduced from the preference among these choices.) Our previous work on CDF_3 also suggested the role of this propensity rule [HARR84].

Oka explained the preference for $\Delta k = \pm 3n$ transitions on the basis of symmetry considerations for the interaction. The rule is related to the presence of the C_3 axis in the molecule. He generalized the argument to apply to any molecule with an n-fold rotational axis, for which we expect

$$\Delta k = jn \quad \text{(j integral).} \tag{5.2}$$

It is possible that the energy transfer pathways that we observe in methane may be rationalized on the basis of this rule. It is very difficult to implement this approach, however, since the

descriptions of the rovibrational eigenstates in the k_R basis are not known. Since k_R is not even an approximately good quantum number for the J values of $^{13}CD_4$ that we are concerned with, a given state (J_R C^n) contains many contributions from basis states of different k_R. The propensites for changes of the various k_R quantum numbers would have to be considered simultaneously. It is not yet clear whether this approach would be helpful or even meaningful. We may have to await a new theoretical description of rovibrational states in spherical tops before a compact, simple expression of a propensity rule such as Eq. 5.2 can be formulated.

5.6 Theoretical Approaches

Recently, there have been a few theoretical calculations of state-to-state energy transfer probabilities for collisions of methane with rare gases [BUCK85,BUCK83]. It would be most valuable to find whether these calculations yield transition probabilities that have a strong C^n dependence. Quantum mechanical close-coupling calculations in the coupled-states approximation have been performed by Secrest and colleagues in an effort to model the aforementioned molecular beam experiments on rotationally inelastic CH_4-Ar scattering. Encouraging agreement is found for $J_i \rightarrow J_f$ transition probabilities, but the authors do not report their results for the individual fine-structure sublevels of the final state J_f. It would seem desirable for future calculations to be reported as the more detailed cross sections, $(J_i, C_i^n) \rightarrow (J_f, C_f^m)$ so that the C^n dependence can be understood on a fundamental level. Of course, we do not know whether collisions with a spherical atom produce the same degree of specificity as do collisions with methane molecules. Also, we do not know how the specificity depends on the state of vibrational excitation (ν_4) chosen in our experiment. These questions remain to be explored in future experiments. But it seems unlikely that for slightly different potential surfaces there would be a complete *absence* of the selectivity that we have seen.

There are difficult obstacles encountered in applying the quantum mechanical calculations to the particular problem that we have studied. A large number of channels for rotational energy transfer are available at the rather high J values of our experiment, most likely making the calculation intractably large. In addition, the anisotropic potential surface for the methane-methane interaction is not known with great accuracy [BOHM84]. Recent differential scattering experiments have led to improvements in our knowledge of the isotropic part of the potential, but the measurements are not very sensitive to the degree of anisotropy present [BOUG85,REID85]. A number of theoretical investigations of energy transfer in methane have relied on classical trajectory simulations, primarily with the goal of modelling vibrational relaxation [DATE84,GRIN84]. But it

is doubtful that calculations at this level would be able to discriminate between the vibrational and rotational angular momenta in order to predict the dependence of the inelastic transition probability on $(R - J)$ [SCHAT83]. The more detailed dependence on C^n is out of the realm of possibilities for calculations that assume methane to be a rigid rotor. A recent treatment of V-T relaxation in methane-argon collisions, using the semi-classical coupled-states approximation, shows an interesting dependence of V-T rates on the initial rotational state of the molecule, but this approach is probably not applicable to R-R energy transfer since the rotational degree of freedom is introduced in an approximate way [PERR84]. We should emphasize again that any theoretical approach will have difficulty in extension to methane-methane collisions because of the more complicated potential surface than in the atom-molecule interaction.

5.7 The Future

The obvious extension of the work described in this thesis to collisions of methane with the rare gases would be attractive from a theoretical standpoint, in view of the considerable calculational difficulties associated with methane-methane collisions. A substantial improvement in the sensitivity of our technique would be required, so that measurements could be carried out in low partial pressures of methane and higher pressures of the buffer gas. It is clear from our results that the effects of self-collisions in a mixture of methane with a buffer gas would need to be minimized, since they lead to such selective energy transfer. Improvement of the sensitivity is made necessary for further study of the methane molecule by its weak absorption strength in the infrared.

To some extent we may expect that highly selective rotational energy transfer in methane is reflective of general behavior in all spherical top molecules. Of course, different molecules have varied patterns of rovibrational energy levels, depending on the rotor moment of inertia and the degrees of rovibrational interaction. Still, our observations for methane suggest that there is a rich variety of behavior to be discovered. A systematic study of spherical tops would allow us to deduce the precise form of propensity rules, should they have a general validity. (This seems to be the case for the propensity rules for symmetric top molecules.) Experiments in progress in our laboratory on the molecule silane (SiH_4) indicate that it has a similar degree of specificity as we observe in methane. This behavior may be manifested as rotationally specific channels of V-V transfer between the ν_4 and ν_2 modes; Coriolis interaction in the protonated molecule is a good deal larger than in the deuterated species. Preliminary results show that V-V transfer is quite fast in this molecule.

A number of spherical top molecules (SiH_4, SiF_4, CCl_4, OsO_4, SF_6, MoF_6, SeF_6, UF_6) can be photodissociated by Infrared Multiple-Photon Excitation (IRMPE) using high-intensity infrared lasers. This is known to occur either in concert with collisions during the laser pulse, or (in some cases) even in isolated molecules. (One recent review of the topic may be found in Ref. [FRAN86].) The work we have described here may have some bearing on IRMPE in collisional conditions: if rotational energy transfer pathways are highly state specific in these molecules, then it will affect the number of possible routes of excitation through the ascending ladder of vibrational levels. This should probably be considered in any detailed models of IRMPE in spherical tops.

Calculations of pressure-broadening parameters of infrared and Raman transitions in methane and other spherical tops have yielded good agreement with experimental observations [TEJW74,VARA74]. Unfortunately, however, the line-broadening coefficient is mainly a measure of the total relaxation rate out of a given level (or pair of levels); it is not very sensitive to the individual state-to-state rate constants. It now appears that the calculated transition rates, which are summed over final states to give $d\gamma/dN$, need to account for the restricted number of pathways through which most of the population transfer occurs from a given initial state. In the process of summing over final states, some of the inaccuracies of the calculation may be "averaged out," masking the inadequacies of the potential model used. Pressure-broadening studies are sometimes used to estimate the value of the octupole moment of methane, which determines the strength of the leading term in the multipolar expansion of the potential. This might be a dangerous procedure if the collision dynamics are not modelled realistically.

One interesting extension of the work presented here would be state-to-state energy transfer experiments in the pentad vibrational levels of methane. This system of rovibrational levels is an exemplary system for the study of rovibrational energy transfer because the spectroscopic details are known extremely well, and the interactions between levels are large, diverse, and highly variable for different rotational levels. One could excite molecules to specific rotational states of the ν_1 vibration by stimulated Raman pumping. Rovibrational energy transfer to the $\nu_2+\nu_4$ level can occur with small changes in energy (cf. Fig. 2-7), and could be monitored on a state-specific basis by transient absorption or gain spectroscopy. For detection by gain, the hotband transition $\nu_2+\nu_4 \rightarrow \nu_2$ would be a convenient choice since it is infrared allowed. The fine-structure rotational levels C^n of a given J value in $\nu_2+\nu_4$ have erratically varying amounts of ν_1 mixed in by Coriolis interaction. (This can be seen by reference to Table 2-2.) Thus, the V-V energy transfer rates can be measured to states very similar in energy but very different in vibrational character. This can be done as a function of the smoothly varying energy gap between vibrational levels by exciting

to different J levels of ν_1 (see Fig. 2-7). At J ~9 in ν_1, the energy gap is essentially zero since the vibrational levels cross. Here the vibrational labels ν_1 and $\nu_2+\nu_4$ are purely nominal for some rotational levels since the mixing is so large. The distinction between vibrational energy transfer and rotational energy transfer is then a purely semantic one. The interesting pattern of Coriolis mixing in this region of the pentad allows one to measure V-V rates under control of the extent of mixing (by careful selection of pumped and probed rotational levels). This technique would not be applicable to CH_4, however, since stimulated Raman pumping in this molecule would not be very selective. The Q branch of ν_1 is very congested, since the interaction with $\nu_2+\nu_4$ is small. The deuterated methanes, both $^{12}CD_4$ and $^{13}CD_4$, would be better choices. Their ν_1 Q branches are dispersed widely, allowing one to pump selected J states, presuming the excitation bandwidth is ~0.1 cm^{-1}.

Whatever may be the course of future research in spherical-top collisions, there is much to be learned that is of value for the understanding of energy transfer in all molecules. Daniel Sennert's prophetic statement, made three hundred twenty-seven years ago, makes "contact or mutual touching" seem an everlastingly enchanting subject.

References

[ABOU84] A. Aboumajd, Doctoral Thesis (Thèse doctorat d'état), Université de Dijon, 1984. (In French.)

[ALEX83] M.H. Alexander and D.C. Clary, *Chem. Phys. Lett.* **98**, 319 (1983).

[AVRA81] E. Avramides and T.F. Hunter. *Chem. Phys.* **57**, 441 (1981).

Related papers on V-V rates: T.F. Hunter and P.C. Turtle, in *Adv. Infrared and Raman Spec.*, Vol. 7, eds. R.J.H. Clark and R.E. Hester (Heyden, London, 1980), ch. 5; T.F. Hunter, *Chem. Phys. Lett.* **105**, 459 (1984); J. Laterrasse and M. Huetz-Aubert. *Chem. Phys. Lett.* **101**, 29 (1983); E. Avramides and T.F. Hunter, *Mol. Phys.* **48**, 1331 (1983); E. Avramides and T.F. Hunter, *Chem. Phys.* **74**, 25 (1983).

[BALL86] J. Ballard and W.B. Johnston, *J. Quant. Spec. Rad. Transf.* **36**, 365 (1986).

[BENSH81] A. Ben-Shaul, Y. Haas, K.L. Kompa, and R.D. Levine, *Lasers and Chemical Change* (Springer, Berlin, 1981), p. 150.

[BEVIN69] P.R. Bevington, *Data Reduction and Error Analysis for the Physical Sciences* (McGraw-Hill, New York, 1969).

[BLOOM67] M. Bloom, F. Bridges, and W.N. Hardy, *Can. J. Phys.* **45**, 3533 (1967).

[BOHM84] H.J. Böhm, R. Ahlrichs, P. Scharf, and H. Schiffer, *J. Chem. Phys.* **81**, 1389 (1984).

[BORY87] A. Borysow and L. Frommhold, *J. Mol. Spec.* **123**, 293 (1987).

[BOUG85] C.V. Boughton, R.E. Miller, and R.O. Watts, *Mol. Phys.* **56**, 363 (1985).

[BRUN82] T.A. Brunner and D. Pritchard, *Adv. Chem. Phys.* **50**, 589, 1982.

[BUCK83] U. Buck, A. Kohlhase, T. Phillips, and D. Secrest, *Chem. Phys. Lett.* **98**, 199 (1983).

[BUCK85] U. Buck, A. Kohlhase, D. Secrest, T. Phillips, G. Scoles, and F. Grein, *Mol. Phys.* **55**, 1233 and 1255 (1985).

[CHAMP77] J.P. Champion, *Can. J. Phys.* **55**, 1802 (1977). (In French.)

[CHAMP78] J.P. Champion, Doctoral Thesis (Thèse doctorat d'état), Université de Dijon, 1978. (In French.)

[CHAMP80] J.P. Champion and G. Pierre, *J. Mol. Spec.* **79**, 255 (1980).

[CHAN86] D.W. Chandler and R.L. Farrow. *J. Chem. Phys.* **85**, 810 (1986); R.L. Farrow, to be published.

[CLAR83] D.C. Clary, *J. Chem. Phys.* **78**, 4915 (1983); D.C. Clary, *J. Phys. Chem.* **91**, 1718 (1987).

[COW76] G.A. Cowan, D.G. Ott, A. Turkevich, L. Machta, G.J. Ferber, and N.R. Daly, *Science* **191**, 1048 (1976).

[DANA87] D.J. Danagher and J. Reid, *J. Chem. Phys.* **86**, 5449 (1987).

[DATE84] N. Date, W.L. Hase, and R.G. Gilbert, *J. Phys. Chem.* **88**, 5135 (1984).

[DEMT82] W. Demtröder. *Laser Spectroscopy*. No. 5 of Springer Series in Chemical Physics (Springer-Verlag, New York. 1982).

[DORN72] A.J. Dorney and J.K.G. Watson. *J. Mol. Spec.* **42**. 135 (1972).

[DUBS82] (a) M. Dubs, D. Harradine, E. Schweitzer, J.I. Steinfeld. and C. Patterson, *J. Chem. Phys.* **77**. 3824 (1982): (b) C. Reiser. J.I. Steinfeld. and H.W. Galbraith. *J. Chem. Phys.* **74**, 2189 (1981); (c) C.C. Jensen, T.G. Anderson, C. Reiser, J.I. Steinfeld. *J. Chem. Phys.* **71**, 3648 (1979).

[ESH82] P. Esherick, A.J. Grimley. and A. Owyoung. *Chem. Phys.* **73**, 271 (1982).

[FLYNN87] G.W. Flynn, priv. commun.

[FOX71] K. Fox. *Phys. Rev. Lett.* **27**, 233 (1971).

[FOX72] K. Fox, *Phys. Rev. A* **6**. 907 (1972).

[FOX84] K. Fox, *J. Chem. Phys.* **80**, 1367 (1984).

[FRAN86] J.S. "Joey" Francisco and J.I. Steinfeld. in *Advances in Multiphoton Processes and Spectroscopy*, Vol. 2. S.H. Lin, ed. (World Scientific, Singapore, 1986).

[FRAN11] J. Franck and R.W. Wood, *Philos. Mag.* **21**, 314 (1911).

[GALB78] H.W. Galbraith, C.W. Patterson, B.J. Krohn, and W.G. Harter, *J. Mol. Spec.* **73**, 475 (1978).

[GRAY79] D.L. Gray and A.G. Robiette, *Mol. Phys.* **37**, 1901 (1979).

[GRIN84] M.B. Grinchak, A.A. Levitsky, L.S. Polak, and S. Ya. Umanskii, *Chem. Phys.* **88**, 365 (1984).

[HARR84] D. Harradine, B. Foy, L. Laux, M. Dubs, and J.I. Steinfeld, *J. Chem. Phys.* **81**, 4267 (1984).

[HARRT84] D. Harradine, Ph.D. Thesis, Dept. of Chemistry, M.I.T., 1984.

[HART84] W.G. Harter and C.W. Patterson, *J. Chem. Phys.* **80**, 4241 (1984). A number of earlier papers are cited here.

[HAUB87] J.G. Haub and B.J. Orr, *J. Chem. Phys.* **86**, 3380 (1987). A number of earlier papers are cited here.

[HAUG84] H.K. Haugen, W.H. Pence, and S.R. Leone, *J. Chem. Phys.* **80**, 1839 (1984).

[HECHT60] K.T. Hecht, *J. Mol. Spec.* **5**. 355 (1960).

[HERZ45] G. Herzberg, *Molecular Spectra and Molecular Structure II. Infrared and Raman Spectra of Polyatomic Molecules* (Van Nostrand Reinhold Co., New York, 1945).

[HERZ66] G. Herzberg, *Molecular Spectra and Molecular Structure III. Electronic Spectra and Electronic Structure of Polyatomic Molecules* (Van Nostrand Reinhold Co., New York, 1966).

[HERZ59] K.F. Herzfeld and T.A. Litovitz, *Absorption and Dispersion of Ultrasonic Waves* (Academic Press, New York, 1959).

[HIRS54] J.O. Hirschfelder, C.F. Curtiss, and R.B. Bird, *Molecular Theory of Gases and Liquids* (Wiley, New York, 1954). (Corrected printing, 1964.)

[HOUG76] J.T. Hougen in *MTP International Review of Science*, Phys. Chem. Ser. 2, Vol. 3, ed. D.A. Ramsay (Butterworth, London, 1976), p.75.

[JAHN38] H.A. Jahn, *Proc. Roy. Soc. A*, **168**, 469 and 495 (1938).

[JOHN61] C.S. Johnson, Jr. and J.S. Waugh, *J. Chem. Phys.* **35**, 2020 (1961).

[KARB85] A. Karbach and P. Hess, *J. Chem. Phys.* **83**, 1075 (1985); A. Karbach and P. Hess, *J. Chem. Phys.* **84**, 2945 (1986).

[KIST74] P.G. Kistemaker, M.M. Hanna, and A.E. De Vries, *Physica* **78**, 457 (1974). Related papers: P.G. Kistemaker, M.M. Hanna, A. Tom, and A.E. De Vries, *Physica* **60**, 459 (1972); G.J. Prangsma, A.H. Alberga, and J.J.M. Beenakker, Physica **64**, 278 (1973).

[KREIN83] W.A. Kreiner and R. Opferkuch, *J. Mol. Struct.* **97**, 293 (1983).

[KREIN87] W.A. Kreiner, P. Müller, L. Jörissen, M. Oldani, and A. Bauder, *Can. J. Phys.* **65**, 32 (1987).

[KREU87] T.G. Kreutz, J.A. O'Neill, and G.W. Flynn, *J. Phys. Chem.* **91**, 5540 (1987).

[LAUX84] L. Laux, B. Foy, D. Harradine, and J.I. Steinfeld, *J. Chem. Phys.* **80**, 3499 (1984).

[LEE87] M.B. "Spike" Lee, Ph.D. Thesis, Dept. of Chemistry, M.I.T., 1987.

[LOETE83] M. Loëte, J.C. Hilico, A. Valentin, J. Chazelas, and L. Henry, *J. Mol. Spec.* **99**, 63 (1983).

[LOLCK81] J.-E. Lolck and A.G. Robiette, *J. Mol. Spec.* **88**, 14 (1981).

[LOLCK82] J.-E. Lolck, A.G. Robiette, L.R. Brown, and R.H. Hunt, *J. Mol. Spec.* **92**, 229 (1982).

[LOLCK85] J.-E. Lolck, G. Poussigue, E. Pascaud, and G. Guelachvili, *J. Mol. Spec.* **111**, 235 (1985).

[LOLCKR85] J.-E. Lolck and S. Brodersen, Poster at Ninth Colloquium on High Resolution Molecular Spectroscopy, Riccione, Italy, 1985.

[MCDOW85] R.S. McDowell, M.I. Buchwald, M.S. Sorem, A.G. Robiette, C.M. Deeley, and W.A. Kreiner, *J. Mol. Spec.* **112**, 363 (1985).

[MEIN86] N. Meinander, G.C. Tabisz, and M. Zoppi, *J. Chem. Phys.* **84**, 3005 (1986).

[MELAN85] G. Melandrone, F. Cappellani, and G. Restelli, *Applied Spectroscopy* **39**, 63 (1985).

[MILLOT86] G. Millot, B. Foy, J.I. Steinfeld, G. Pierre, A. Valentin, and L. Henry, Presented at IXth International Conference on High Resolution Infrared Spectroscopy, Liblice, Czechoslovakia, 1986.

[MILLOT87] G. Millot, B. Lavorel, R. Chaux, R. Saint-Loup, G. Pierre, H. Berger, J.I. Steinfeld, and B. Foy, *J. Mol. Spec.* **127**, xxx (1987).

[OKA68] T. Oka, *J. Chem. Phys.* **48**, 4919 (1968).

[OKA73] T. Oka, *Adv. At. Mol. Phys.* **9**, 127 (1973).

[ORR84] B.J. Orr, J.G. Haub, and R. Haines, *Chem. Phys. Lett.* **107**, 168 (1984).

[OWY78] A. Owyoung, C.W. Patterson, and R.S. McDowell, *Chem. Phys. Lett.* **59**, 156 (1978); Erratum **61**, 636 (1979).

[PAPOU82] D. Papousek and M.R. Aliev, *Molecular Vibrational-Rotational Spectra*, No. 17 of Studies in Physical and Theoretical Chemistry (Elsevier Scientific Publishing Co., Amsterdam, 1982).

[PARM78] C.S. Parmenter and K.Y. Tang, *Chem. Phys.* **27**, 127 (1978).

[PASC87] E. Pascaud, G. Poussigue, G. Guelachvili, and J.-E. Lolck, *J. Mol. Spec.* **121**, 20 (1987).

[PEREV84] (a) V.I. Perevalov, V.G. Tyuterev, and B.I. Zhilinskii, *Chem. Phys. Lett.* **104**, 455 (1984); (b) V.I. Perevalov, V.G. Tyuterev, and B.I. Zhilinskii, *J. Mol. Spec.* **103**, 147 (1984). Also: C. Pierre, M. Loete, and G. Pierre, *Can. J. Phys.*, in press (1987). (In French.)

[PERR82] M.Y. Perrin, *Chem. Phys. Lett.* **93**, 515 (1982).
Related papers on V-T rates: E.A. Gregory, M.R. Buckingham, D.Z. Clayton, F.J. Wolfenden, and C.J.S.M. Simpson, *Chem. Phys. Lett.* **104**, 393 (1984); M.H. De Vasconcelos, *Physica* **88A**, 395 (1977).

[PERR84] M.Y. Perrin and G. Jolicard, *Chem. Phys.* **91**, 341 (1984).

[PIERRE77] G. Pierre, J. Cadot, R.J. Corice, and K. Fox, *Can. J. Phys.* **55**, 473 (1977). (In French.)

[PIERRE80] C. Pierre, G. Pierre, J.P. Champion, J.C. Fontanella, and M. Delplanque, *J. Physique* **41**, 393 (1980). (In French.)

[PIERRE87] G. Pierre, G. Millot, A. Valentin, L. Henry, B. Foy, and J.I. Steinfeld, submitted to *Can. J. Phys.* (In French.)

[PLYLER60] E.K. Plyler, E.D. Tidwell, and L.R. Blaine, *J. Res. N.B.S.* **64A**, 201 (1960).

[PPCP82] G. Poussigue, E. Pascaud, J.P. Champion, and G. Pierre, *J. Mol. Spec.* **93**, 351 (1982).

[REID85] B.P. Reid, M.J. O'Loughlin, and R.K. Sparks, *J. Chem. Phys.* **83**, 5656 (1985).

[ROBI81] A.G. Robiette, *J. Mol. Spec.* **86**, 143 (1981).

[SCHAT83] G.C. Schatz in *Molecular Collision Dynamics*, Topics in Current Physics No. 33, J.M. Bowman, ed. (Springer, New York, 1983).

[SIEB74] D.R. Siebert, F.R. Grabiner, and G.W. Flynn, *J. Chem. Phys.* **60**, 1564 (1974).

[STEIN74] J.I. Steinfeld, *Molecules and Radiation* (M.I.T. Press, Cambridge, Mass., 1974).

[STEIN65] J.I. Steinfeld and W. Klemperer, *J. Chem. Phys.* **42**, 3475 (1965).

[TEJW74] G.D.T. Tejwani and K. Fox, *J. Chem. Phys.* **60**, 2021 (1974); G.D.T. Tejwani and P. Varanasi, *J. Chem. Phys.* **55**, 1075 (1971).

[TELL34] E. Teller, *Hand- und Jahrbuch der chemischen Physik* **9**, Part II, 43 (1934). (In German.)

[TEMPS87] F. Temps, S. Halle, P.H. Vaccaro, R.W. Field, and J.L. Kinsey, *Trans. Faraday Soc. II* **84**, xxx (1988); F. Temps, S. Halle, P.H. Vaccaro, R.W. Field, and J.L. Kinsey, *J. Chem. Phys.* **87**, 1895 (1987). See also: P.H. Vaccaro, Ph.D. Thesis, Department of Chemistry, Massachusetts Institute of Technology, 1986.

[THOM87] J.W. Thoman, Jr., Ph.D. Thesis, Department of Chemistry, M.I.T., 1987.

[TOSE86] B. Toselli, J.C. Ferrero, and E.H. Staricco, *J. Phys. Chem.* **90**, 4562 (1986).

[TOWN55] C.H. Townes and A.L. Schawlow, *Microwave Spectroscopy* (McGraw-Hill, New York, 1955; Dover, New York, 1975).

[TYUT84] V.G. Tyuterev, J.P. Champion, G. Pierre, and V.I. Perevalov, *J. Mol. Spec.* **105**, 113 (1984).

[VANZ87] C.M. Van Zoeren, A.B. Rock, S.H. Kable, G.B. Edwards, and A.E.W. Knight, submitted to *J. Chem. Phys.*

[VARA74] P. Varanasi, *J. Quant. Spec. Rad. Transf.* **14**, 995 (1974).

[VEEK85] K. Veeken, N. Dam, and J. Reuss, *Chem. Phys.* **100**, 171 (1985).

[VOLK84] S. Yu. Volkov, D.N. Kozlov, M.R. Malikov, and V.V. Smirnov, *Sov. Phys. JETP* **59**, 482 (1984).

[WATSON71] J.K.G. Watson, *J. Mol. Spec.* **40**, 536 (1971).

[WILS35] E. B. Wilson, Jr., *J. Chem. Phys.* **3**, 276 (1935).

[YARD80] J.T. Yardley, *Introduction to Molecular Energy Transfer* (Academic Press, New York, 1980).

[ZITT73] P.F. Zittel and C.B. Moore, *J. Chem. Phys.* **58**, 2004 (1973).

Appendix One
Hotband Spectrum of $^{13}CD_4$ from 960 to 980 cm^{-1}

Listed here is a portion of the calculated hotband spectrum (pentad ← dyad) in the central region from 960 to 980 cm^{-1}, consisting mainly of Q-branch lines. The intention of this appendix is to demonstrate the lack of ambiguity in the assignments of the hotband transitions, which is necessary for obtaining meaningful energy transfer results. Generally, the residual error in the calculated frequency of a line is much less than the separation between neigboring lines. A few large residuals, mainly at higher J values, attest to the fact that the analysis is at an incomplete stage, but work is in progress to refine it. Only the transitions for which the intensity $\geq$ 1.0 are listed here; this excludes most of the "forbidden" transitions.

Notes:

1. Transition notation: explained in the notes to Table 4-1. For the sake of visual clarity, subscripts are not used in the designation of the symmetry species (e.g., A_1 is denoted "A1").

2. ν(cal.): calculated frequency, in cm^{-1}.

3. Int.: calculated intensity, in arbitrary units.

4. O-C: observed frequency minus calculated frequency, in units of mK (10^{-3} cm^{-1}). The observed frequencies are from the FTIR spectrum taken by Valentin and Henry (cf. section 2.3.2).

5. ν_2 level?: an asterisk (*) indicates that the initial level of the transition is in the ν_2 state; these transitions are of the type $\nu_2 + \nu_4 \leftarrow \nu_2$. Unmarked transitions are, of course, of the type $2\nu_4 \leftarrow \nu_4$.

J''	n''	C''	n	ν(cal.)	Int.	O-C	ν_2 level?
P(7)	2	A2	4	960.0065	7.4	1.1	
Q(16)	5	F2	5	960.0075	1.3		
Q(16)	2	A2	2	960.0101	1.1		
P(7)	10	F1	20	960.1570	2.8	-0.1	*
P(6)	4	F2	8	960.3050	8.6	0.8	
Q(8)	4	F1	4	960.5645	1.5	1.1	
Q(8)	3	E	3	960.6740	1.0	0.6	
P(6)	1	A1	2	960.6750	3.4	-0.4	
P(6)	8	F2	16	960.8868	2.4	-0.4	*
P(6)	3	E	5	960.9827	5.7	1.0	
P(6)	2	F1	5	960.9927	4.1	-0.2	
P(6)	2	E	4	961.1245	2.7	-0.2	
P(6)	7	F1	14	961.1655	2.2	0.3	*
P(7)	7	F2	17	961.2409	2.3	-0.4	*
P(7)	5	E	13	961.4518	1.6	-0.6	*
P(6)	4	F1	7	961.4597	8.6	1.0	
Q(7) .	4	F1	2	961.4842	1.4	0.9	
Q(7)	3	F2	4	961.5062	1.9	1.3	
Q(15)	5	F1	6	961.5522	1.7		
Q(15)	4	F2	6	961.5589	1.7		
Q(7)	2	A1	1	961.6793	1.3	1.5	
P(6)	3	F2	7	961.7500	4.0	0.7	
P(6)	3	F1	6	961.7851	3.9	-0.1	
P(6)	1	A2	2	961.9345	3.3	-0.2	
P(6)	1	F1	4	962.1929	1.3	-0.5	
P(6)	2	F2	6	962.2624	1.4	-0.7	
Q(6)	3	F1	2	962.2770	1.8	1.2	
Q(6)	3	F2	2	962.3202	2.0	0.4	
P(6)	2	A1	3	962.3414	7.1	1.1	
Q(6)	1	A2	2	962.3908	1.7	-0.1	
Q(5)	3	F2	1	962.4702	2.0	0.4	
P(7)	7	F1	19	962.6519	2.2	-0.3	*
Q(15)	4	F1	4	962.7056	1.0	-1.6	
Q(5)	2	E	1	962.7415	1.6	0.5	
Q(14)	2	A1	2	962.8639	1.9	-31.2	
P(7)	6	F2	18	962.8698	2.6	0.6	*
Q(14)	4	F1	5	962.8809	2.2	-32.8	
Q(14)	3	E	4	962.8912	1.5	-33.5	
Q(14)	11	F2	14	962.9493	1.1	1.8	
Q(14)	11	F1	15	962.9648	1.1	1.9	
Q(4)	2	F1	1	963.0389	2.3	-0.3	
P(6)	5	F1	8	963.3032	9.0	1.4	
Q(3)	1	A1	1	963.3372	1.8	-1.0	
P(6)	6	E	11	963.3415	1.8	-0.2	*
P(6)	8	F1	16	963.4454	2.7	0.4	*
P(6)	5	F2	9	963.4942	9.0	1.4	
P(6)	3	A1	6	963.6326	2.4	0.2	*
Q(16)	5	F1	10	963.6416	1.0	-27.6	
Q(16)	6	F2	10	963.6899	1.0	-27.9	
Q(9)	2	A2	2	963.7781	1.5	0.4	
Q(3)	2	F1	1	963.8216	2.3	-0.9	

J''	n''	C''	n	ν(cal.)	Int.	O-C	ν_2 level?
Q(2)	1	F1	1	963.8876	1.8	-1.3	
Q(13)	4	F1	5	963.9405	2.8	45.3	
Q(4)	1	E	1	963.9727	1.8	-0.3	
Q(13)	4	F2	6	963.9762	2.8		
Q(1)	1	F2	1	963.9875	1.2	-1.7	
Q(10)	4	F2	6	963.9902	1.0	-4.4	
Q(2)	1	E	1	964.0539	1.2	-0.8	
P(5)	2	A2	3	964.1418	6.9	1.1	
Q(3)	1	F2	1	964.1573	2.5	-0.8	
Q(4)	2	F2	1	964.1896	2.9	-0.2	
Q(5)	2	F1	1	964.2378	3.1	0.1	
P(5)	2	F1	5	964.3950	3.7	0.2	
Q(15)	2	A1	4	964.4172	1.1		
Q(15)	6	F1	10	964.4803	1.3	9.2	
Q(4)	1	A2	1	964.4970	2.6	-0.4	
Q(10)	4	F1	6	964.5006	1.3	-4.0	
Q(6)	1	A1	1	964.5350	2.9	0.5	
P(5)	2	F2	4	964.5737	3.7	4.2	
Q(5)	2	F2	2	964.5743	3.3	3.6	
Q(9)	4	F2	6	964.6076	1.6	0.3	
Q(8)	4	F2	4	964.6813	1.6	0.1	
Q(12)	3	E	4	964.7339	2.2	-15.9	
Q(12)	4	F2	4	964.7620	3.3	-16.0	
P(5)	4	F2	6	964.7636	8.2	0.9	
Q(12)	1	A2	2	964.8206	2.8	-17.1	
Q(6)	2	F1	3	964.8440	3.2	0.5	
P(5)	3	A2	5	964.8530	2.1	-1.3	*
Q(9)	3	E	3	964.9189	1.2	5.2	
Q(6)	2	E	2	964.9618	2.5	0.1	
Q(14)	5	F1	9	964.9678	1.5	30.6	
Q(14)	4	F2	4	964.9823	1.4	-1.0	
Q(14)	3	F1	4	964.9834	1.4	-2.1	
Q(7)	3	F1	3	965.0327	3.8	0.5	
Q(14)	5	F2	9	965.0415	1.5	22.9	
P(5)	6	F1	12	965.1203	1.9	0.3	*
Q(13)	10	F1	13	965.1632	1.5	0.9	
Q(7)	2	F2	3	965.2099	4.1	0.1	
Q(13)	3	A1	5	965.2361	1.3	0.4	
Q(11)	4	F1	5	965.2459	3.7	-9.4	
Q(13)	3	E	6	965.2560	1.2		
Q(13)	5	F2	9	965.2966	1.7		
Q(11)	2	A1	3	965.3108	1.9	-6.2	
Q(8)	2	E	2	965.3169	2.7	-4.0	
Q(11)	3	F2	5	965.3226	3.8	-9.7	
P(5)	3	F1	6	965.3532	8.2	1.2	
Q(12)	4	F1	8	965.3891	1.8		
Q(8)	3	F2	3	965.3911	4.1	-0.8	
Q(13)	3	A2	3	965.3982	1.3		
P(6)	6	F1	15	965.4120	2.6	0.5	*
Q(10)	2	A1	1	965.4427	3.3		
P(5)	6	F2	11	965.4451	1.9	0.0	*

J″	n″	C″	n	ν(cal.)	Int.	O-C	ν₂ level?
Q(9)	3	F1	3	965.4930	4.1	-2.0	
Q(10)	2	E	3	965.5233	1.1		
Q(8)	1	A2	2	965.5272	3.6	0.6	
Q(10)	3	F1	4	965.5339	4.1		
Q(12)	5	F2	8	965.5684	1.6		
P(5)	4	E	9	965.5865	1.5	0.6	*
Q(9)	3	F2	4	965.5997	4.0	-2.4	
Q(10)	2	E	4	965.6180	1.7	-3.7	
Q(8)	3	F1	5	965.7147	1.6	0.8	
Q(11)	5	F1	8	965.7193	1.4	-3.8	
P(5)	1	F2	3	965.9466	1.1	-3.3	
Q(10)	4	F1	7	966.1013	1.1	-0.4	
P(5)	2	E	4	966.1805	2.4	0.5	
P(5)	3	F2	5	966.2353	3.6	0.4	
P(6)	4	E	10	966.2790	1.6	1.1	*
P(5)	1	A1	2	966.4018	7.2	1.7	
P(6)	6	F2	17	966.4397	2.5	1.4	*
Q(7)	4	F1	4	966.5557	1.1	-0.9	
P(6)	2	A2	5	966.6533	2.4	1.6	*
P(5)	7	F2	12	966.7700	2.2	0.5	*
Q(13)	11	F2	28	966.8966	1.0	-0.2	*
Q(13)	11	F1	27	966.9338	1.0	1.8	*
P(5)	7	F1	13	966.9353	2.7	0.3	*
P(5)	4	F1	7	966.9558	8.6	1.6	
P(5)	3	E	5	967.0780	5.8	1.7	
Q(13)	2	A2	1	967.1493	1.5	-1.0	
Q(13)	3	F2	4	967.1495	1.8	-1.2	
Q(13)	2	E	3	967.1498	1.2	-1.5	
Q(12)	10	F2	12	967.2294	2.0	4.8	
Q(12)	9	F1	13	967.3363	2.0	0.5	
P(4)	1	A2	1	967.8149	2.6	0.5	
Q(7)	2	A1	2	967.8579	1.5	-0.9	
P(4)	2	F2	4	968.0952	3.0	0.0	
P(4)	1	E	2	968.1885	2.0	0.0	
P(4)	3	F2	5	968.5127	7.2	1.3	
Q(12)	10	F1	26	968.9263	1.3	1.5	*
Q(12)	4	A1	9	968.9852	1.1	-0.8	*
P(4)	2	E	3	969.0672	4.7	1.3	
Q(12)	3	F1	4	969.1849	2.2	0.7	
Q(11)	3	A2	3	969.1853	2.1	0.4	
Q(12)	3	F2	3	969.1880	2.2	-2.4	
Q(11)	8	F2	12	969.2982	2.6	0.0	
Q(11)	6	E	8	969.3596	1.7	-0.2	
P(5)	2	A1	4	969.4774	2.1	1.3	*
P(4)	5	F2	10	969.8503	1.5	5.8	*
P(5)	5	F1	14	970.0188	2.2	2.4	*
P(4)	3	F1	5	970.0783	7.7	1.7	
P(5)	5	F2	13	970.2559	2.6	2.3	*
P(4)	5	F1	9	970.3183	1.9	-6.7	*
P(4)	4	E	6	970.3620	1.5	0.5	*
P(4)	6	F2	11	970.4226	1.6	1.0	*

J″	n″ C″		n	ν(cal.)	Int.	O-C	ν₂ level?
Q(13)	9	F1	14	970.4518	1.2		
R(1)	1	F1	1	970.6616	1.2	-1.6	
P(4)	2	A1	4	970.6790	1.8	1.2	*
P(4)	4	F2	6	970.7275	7.7	1.8	
P(4)	2	F1	4	970.7427	3.0	0.9	
Q(11)	9	F2	24	970.7809	1.7	0.1	*
Q(11)	10	F1	23	970.8707	1.7	0.0	*
P(4)	2	A2	3	970.9347	1.9	1.6	*
Q(13)	10	F2	15	971.0138	1.4	9.3	
Q(11)	1	A1	2	971.0543	2.2	-0.6	
Q(11)	3	F1	3	971.0651	2.6	-0.8	
Q(11)	2	E	2	971.0721	1.7	-0.9	
Q(10)	8	F2	10	971.1511	3.2	-0.2	
P(3)	1	F2	2	971.2318	2.1	0.5	
Q(10)	8	F1	11	971.2576	3.3	-0.4	
Q(12)	6	E	9	972.4067	1.0		
P(3)	2	F1	3	972.4559	1.9	3.5	
P(3)	3	F1	4	972.4583	5.2	1.1	
Q(10)	3	A2	8	972.4736	1.7	0.1	*
Q(10)	9	F2	21	972.6041	2.1	-0.3	*
Q(12)	9	F2	13	972.6390	1.7	6.0	
Q(10)	6	E	15	972.6701	1.4	-1.0	*
Q(10)	2	F1	3	972.7220	2.9	0.2	
Q(10)	3	F2	3	972.7587	2.9	-0.5	
Q(9)	5	E	6	972.9472	2.5	-0.3	
Q(9)	7	F1	9	972.9845	3.8	-0.4	
Q(9)	2	A1	4	973.0686	3.3	-0.2	
Q(12)	3	A2	6	973.1205	1.8	5.5	
P(2)	1	A1	1	973.4904	3.4	0.3	
P(3)	2	E	3	973.5374	4.0	1.6	
R(2)	2	F2	1	973.6171	1.8	-1.2	
P(3)	5	F1	7	973.8829	1.4	6.3	*
Q(16)	7	F1	15	973.8950	1.3		
P(4)	4	F1	10	973.9072	2.2	4.5	*
R(2)	2	F1	1	973.9134	1.9	-1.7	
P(4)	3	E	7	974.0352	1.6	2.7	*
Q(9)	2	E	2	974.0678	1.9	0.6	
P(3)	2	F2	3	974.0720	6.0	1.5	
Q(9)	2	F2	3	974.1103	2.9	0.2	
Q(9)	8	F2	20	974.1580	2.5	-0.2	*
Q(9)	1	A2	1	974.2228	2.5	-0.5	
Q(16)	7	F2	14	974.2462	1.3		
Q(16)	3	A2	6	974.2684	1.1		
Q(11)	9	F1	12	974.3021	1.8	4.9	
R(2)	1	A1	1	974.3097	1.7	-2.7	
Q(9)	8	F1	19	974.3497	2.4	-0.7	*
Q(15)	5	F2	12	974.5511	1.5	3.6	
Q(14)	3	F2	5	974.5823	1.1	1.1	
P(3)	1	A2	2	974.6029	5.2	2.3	
Q(11)	7	F2	13	974.6040	2.3	1.2	
Q(8)	7	F2	8	974.6110	4.4	-0.7	

J"	n" C"		n	ν(cal.)	Int.	O-C	ν₂ level?
Q(15)	5	E	9	974.6526	1.2	6.4	
Q(8)	6	F1	9	974.6598	4.5	-0.8	
Q(15)	7	F1	13	974.7712	1.5	4.2	
Q(7)	1	A1	1	974.8161	1.1	-5.3	
Q(15)	6	F2	14	974.8276	1.8	12.9	
P(2)	2	A1	2	974.8416	1.1	-1.1	*
Q(8)	2	F1	3	974.8740	2.2	1.3	
P(3)	4	F2	6	974.9311	1.7	2.0	*
Q(7)	2	F1	2	974.9608	1.0	1.4	
P(3)	3	E	5	974.9827	1.0	1.8	*
Q(8)	2	F2	2	975.0705	2.3	0.6	
Q(14)	2	A2	5	975.2996	1.7	10.5	
Q(14)	6	F1	13	975.3683	2.5	-0.4	
P(3)	1	A1	1	975.4667	1.8	1.3	
Q(14)	6	F2	12	975.4773	2.1	7.3	
Q(14)	4	E	9	975.6308	1.4	5.3	
Q(8)	5	E	12	975.6316	1.9	4.5	*
P(3)	4	F1	8	975.6346	1.7	1.5	*
Q(13)	4	A2	5	975.7534	1.4	3.9	
Q(8)	7	F1	18	975.7659	2.8	-0.5	*
Q(16)	8	F2	15	975.8202	1.3	16.2	
Q(16)	8	F1	16	975.8227	1.3	13.6	
Q(13)	2	F2	5	975.8852	1.4	1.0	
Q(13)	3	F1	4	975.9318	1.3	0.1	
Q(13)	2	A1	4	975.9987	2.7	14.5	
Q(8)	3	A1	6	976.0484	2.3	-0.8	*
Q(7)	5	F2	8	976.1330	5.0	2.6	
Q(10)	7	F1	12	976.1343	2.3	1.2	
Q(7)	2	A2	2	976.1367	4.3	-1.2	
Q(7)	4	E	5	976.1568	3.3	-0.5	
Q(13)	6	F2	13	976.1690	2.9	7.1	
Q(15)	7	F2	15	976.1770	1.8	15.0	
Q(15)	8	F1	15	976.2053	1.9	18.9	
Q(15)	3	A1	6	976.2100	1.6	14.2	
Q(12)	11	F1	27	976.2409	1.2	0.5	*
Q(10)	5	E	8	976.2452	1.8	1.0	
Q(13)	5	F1	11	976.3202	2.9	6.3	
Q(15)	2	A2	4	976.3473	1.5	3.3	
Q(10)	3	A1	4	976.4302	2.9	1.0	
R(3)	1	A2	1	976.4925	1.8	-9.8	
Q(14)	5	E	10	976.5316	1.7		
Q(14)	7	F1	14	976.5870	2.6		
Q(14)	7	F2	13	976.6435	2.5		
Q(12)	11	F2	26	976.7565	1.2	-2.5	*
R(3)	2	F2	1	976.7731	2.2	-0.5	
Q(12)	4	E	8	976.8520	2.5	6.0	
Q(12)	5	F1	11	976.9036	3.7	6.0	
Q(13)	6	F1	12	976.9505	3.2	4.8	
Q(13)	7	F2	14	976.9556	3.4	-0.3	
Q(7)	6	F2	16	976.9616	3.1	3.8	*
Q(13)	9	F2	17	976.9817	1.2	-1.8	

J"	n"	C"	n	ν(cal)	Int.	O-C	ν₂ level?
R(3)	2	E	1	976.9896	1.6	-0.4	
Q(13)	4	E	8	977.0115	2.2	6.9	
Q(12)	2	E	3	977.0246	1.1	1.2	
Q(12)	2	F1	5	977.0723	1.6	0.7	
P(1)	1	F1	1	977.2403	1.4	1.1	
Q(12)	1	A1	2	977.2451	1.5	-3.7	
Q(7)	7	F1	15	977.3243	3.0	-0.6	*
Q(12)	2	A2	5	977.3592	3.6	8.0	
Q(12)	6	F1	12	977.3636	4.1	3.7	
Q(12)	6	F2	11	977.3706	4.3	6.0	
P(2)	2	F1	2	977.4076	3.2	1.8	
Q(11)	7	E	16	977.4237	1.0	-4.9	*
Q(12)	8	F2	14	977.4425	1.7	-0.3	
Q(6)	5	F2	6	977.4699	5.6	-0.1	
Q(11)	4	F2	10	977.4837	4.7	4.6	
Q(6)	5	F1	7	977.5150	5.2	-0.3	
R(3)	3	F1	1	977.5754	2.6	-0.1	
Q(12)	2	A1	4	977.6911	3.4	8.0	
Q(11)	4	E	7	977.7556	3.5	3.5	
Q(14)	5	F2	11	977.7590	1.1	0.1	
Q(9)	7	F2	11	977.7749	2.5	0.4	
Q(11)	5	F2	11	977.7790	5.3	4.1	
Q(14)	5	F1	11	977.7799	1.1	-4.6	
Q(11)	10	F2	26	977.8480	1.5	-0.7	*
P(3)	3	F2	7	977.8834	1.9	3.0	*
Q(10)	7	F1	13	977.8950	1.2	-1.7	
Q(11)	2	F2	4	977.9085	1.5	1.2	
Q(6)	2	A2	6	977.9233	2.7	-0.3	*
Q(13)	3	A2	4	978.0059	1.5	-2.8	
Q(13)	5	F2	11	978.0071	1.8	-4.0	
Q(13)	3	E	7	978.0148	1.2	-11.7	
Q(9)	6	F1	10	978.0174	4.0	-0.1	
Q(11)	6	F1	11	978.0329	5.0	0.1	
Q(10)	2	A2	4	978.1015	4.7	2.9	
Q(10)	5	F1	10	978.1755	6.2	2.3	
Q(11)	2	F1	4	978.1977	1.9	-0.4	
P(2)	2	F2	3	978.2208	3.9	1.7	
Q(12)	4	F1	10	978.3696	2.6	-1.4	
Q(6)	6	F2	13	978.3733	3.1	-0.8	*
Q(12)	5	F2	9	978.3802	2.7	1.6	
Q(10)	3	E	7	978.3811	4.0	0.7	
Q(10)	5	F2	9	978.4044	5.7	0.2	
Q(10)	1	A2	2	978.4738	1.4	-5.8	
Q(11)	4	A2	8	978.4997	1.3	-2.2	*
Q(9)	1	A1	3	978.5633	6.0	1.1	
Q(5)	3	E	4	978.5952	3.9	0.0	
Q(6)	4	E	9	978.6097	2.1	-0.5	*
Q(10)	2	F2	4	978.6300	1.3		
Q(5)	4	F1	5	978.6684	5.5	-0.1	
Q(7)	10	F1	16	978.6784	1.2	-10.1	*
Q(9)	4	F1	8	978.7042	7.0	0.7	

130

J''	n''	C''	n	ν(cal.)	Int.	O-C	ν_2 level?
Q(10)	9	F1	23	978.7149	1.6	1.1	*
Q(11)	5	F1	9	978.7522	1.9	-0.4	
Q(11)	2	A1	4	978.8042	2.9	2.9	
Q(11)	3	E	6	978.8071	2.4	0.1	
Q(11)	5	F1	10	978.8334	1.7	-2.6	
Q(9)	5	F2	10	978.8401	6.5	0.0	
Q(11)	5	E	9	978.9295	2.0	-2.9	
Q(5)	1	A1	2	978.9894	4.6	-0.3	
Q(14)	3	A2	6	979.0490	1.1	5.5	
Q(14)	2	F2	6	979.0630	1.1	9.3	
Q(8)	4	F1	8	979.0698	7.7	2.5	
Q(10)	13	F2	24	979.0718	1.0	0.5	*
Q(5)	5	F2	12	979.1711	3.1	-0.4	*
Q(12)	8	F1	15	979.1722	1.9	-1.5	
Q(8)	3	E	6	979.1860	4.8	-7.0	
Q(10)	4	F2	8	979.1962	4.6	-0.6	
Q(10)	10	F2	22	979.2492	1.8	4.1	*
Q(14)	9	F2	17	979.2509	1.3	-9.1	
Q(10)	4	F1	9	979.2544	4.1	-1.1	
Q(8)	3	A2	7	979.2747	1.1	-3.6	*
Q(7)	3	F2	6	979.3553	1.9	-0.9	
Q(8)	6	F2	9	979.3757	3.5	-0.5	
Q(8)	4	E	7	979.4183	3.3	0.2	
Q(7)	3	F2	7	979.4621	6.2	-0.4	
Q(9)	3	A1	8	979.4661	1.9	-4.4	*
Q(13)	8	F2	16	979.4714	1.1	-9.7	
Q(4)	4	F2	4	979.4972	5.6	-1.6	
R(4)	4	F2	2	979.4978	2.4	-2.2	
Q(13)	8	F1	16	979.5432	1.8	-7.3	
Q(9)	4	F2	9	979.6074	5.3	-0.1	
Q(9)	3	E	5	979.6605	3.7	-0.2	
Q(6)	1	A2	3	979.6880	6.9	0.0	
Q(10)	6	F1	12	979.6910	1.1	-3.0	
Q(7)	1	E	3	979.6993	2.6	-1.0	
Q(9)	2	A2	3	979.7350	5.2	-2.2	
Q(12)	7	F1	14	979.7489	1.6	1.0	
Q(9)	4	A2	7	979.7671	1.4	-1.4	*
Q(13)	1	A1	2	979.7722	1.1	1.3	
Q(11)	3	A1	5	979.7723	2.3	1.1	
Q(5)	5	F1	11	979.7899	3.0	-0.7	*
Q(3)	1	A2	1	979.8104	4.5	0.6	
R(4)	3	F1	1	979.8690	2.5	0.2	
Q(8)	2	F2	4	979.8775	2.3	-0.5	
Q(13)	2	F1	6	979.8996	1.0	0.9	
Q(9)	7	F2	12	979.9203	1.8	-2.7	
Q(10)	7	F2	11	979.9576	2.3	-3.1	
Q(10)	11	F2	23	979.9776	1.1	4.4	*
Q(2)	1	A2	3	979.9810	1.7	1.0	*
Q(8)	4	F2	7	979.9946	6.4	-1.2	
Q(8)	8	F2	17	980.0197	1.0	-3.5	*
Q(11)	8	F1	14	980.0214	2.2	4.7	

J''	n''	C''	n	ν(cal.)	Int.	O-C	ν_2 level?
Q(4)	3	F1	5	980.0262	5.4	-0.1	
Q(7)	2	F1	4	980.0324	3.8	-0.9	
Q(4)	3	E	7	980.0515	1.8	-0.8	*
Q(8)	3	F1	7	980.0599	6.4	-2.3	
Q(7)	2	E	4	980.0648	5.1	-0.6	
Q(9)	6	E	13	980.0773	1.3	1.9	*
Q(3)	1	A1	2	980.0793	5.0	-0.1	
Q(8)	2	A2	4	980.0988	3.9	-0.4	
Q(13)	1	E	4	980.1024	1.0	6.4	
Q(9)	6	F2	11	980.1088	1.5	0.0	
Q(6)	2	F2	3	980.1275	4.6	-0.9	
Q(6)	3	F2	5	980.1555	7.9	-3.8	
Q(7)	4	F1	6	980.1956	5.8	3.6	
Q(12)	3	A1	5	980.2411	2.2	-7.0	
Q(10)	4	A2	9	980.2725	1.3	4.3	*
Q(5)	3	F2	5	980.3305	7.6	0.0	
Q(9)	10	F2	22	980.3392	1.4	0.8	*
Q(8)	2	F1	5	980.3836	2.3	0.7	
Q(8)	4	A2	8	980.3907	1.0	-6.4	*
Q(10)	7	F2	12	980.4556	1.6	7.3	
Q(5)	1	A2	1	980.4590	3.9	-0.7	
Q(4)	4	F1	10	980.4638	2.6	-0.9	*
Q(9)	9	F1	21	980.5061	1.6	-2.0	*
Q(7)	4	F1	7	980.5344	1.6	0.4	
Q(4)	2	F1	4	980.5450	6.7	0.1	
Q(7)	2	A1	3	980.5543	5.7	-0.2	
Q(1)	1	E	1	980.5621	2.2	0.5	
Q(6)	3	F1	5	980.5891	7.4	-0.1	
Q(7)	6	F1	8	980.6047	5.3	-6.5	
R(4)	2	E	1	980.6611	1.9	0.2	
Q(3)	2	F2	4	980.6787	4.9	0.2	
P(2)	3	F2	5	980.6818	1.1	-2.9	*
Q(2)	2	F2	2	980.6916	4.3	0.3	
Q(5)	2	E	3	980.7037	4.9	-1.0	
Q(12)	1	F1	6	980.7061	1.3	-3.4	
Q(8)	8	F1	19	980.7163	2.6	4.7	*
Q(9)	2	F2	6	980.7596	1.1	0.4	
R(4)	3	F2	1	980.8129	2.8	0.4	
Q(3)	3	F2	8	980.8517	2.0	-0.7	*
Q(8)	6	F2	10	980.8913	1.5	-2.4	
Q(12)	2	F2	5	980.9173	1.5	-0.1	
Q(9)	3	A2	4	980.9578	3.9	-2.7	
Q(7)	1	A1	2	980.9947	2.8	-0.7	

Appendix Two
"Rotational Energy Transfer Cross Sections in Methane ($^{13}CD_4$)
from Infrared Double Resonance Measurements"

ROTATIONAL ENERGY TRANSFER CROSS SECTIONS IN METHANE ($^{13}CD_4$) FROM INFRARED DOUBLE RESONANCE MEASUREMENTS

B. FOY, L. LAUX [1], S. KABLE [2] and J.I. STEINFELD

Department of Chemistry, Massachusetts Institute of Technology, Cambridge, MA 02139, USA

Rotational relaxation times have been measured for methane ($^{13}CD_4$) in collisions with itself, He, Ne, Ar, Kr, Xe, and CH_2F_2, using the method of infrared double resonance. Collision efficiencies range from one-half to greater than gas-kinetic, and the measured relaxation times are longer in the vibrational ground state than in the $v_4 = 1$ excited state.

1. Introduction

We have been carrying out infrared–infrared double resonance (IRDR) experiments on methane ($^{13}CD_4$) using a high-resolution tunable diode laser probe [1]. These measurements enable us to obtain state-specific rotational energy transfer (RET) rates for this spherical-top molecule. In this Letter, we report the total RET rates for this molecule with a variety of collision partners; data for both the ground and lowest excited vibrational state ($v_4 = 1$) of $^{13}CD_4$ are presented.

2. Experimental

The IRDR apparatus has been described in detail elsewhere [2]. The mass-21 isotope of methane, chosen in order to obtain good coincidences with CO_2 laser pumping lines, was furnished by Los Alamos National Laboratory. The other gases used as collision partners were purchased from Matheson Gas Products and had stated purities of at least 99.995%. Pressures were measured by a capacitance manometer attached directly to the cell. Experiments were carried out at ambient temperature (295–298 K), except for one set of runs

[1] Present address: Lockheed Palo Alto Research Laboratory, Palo Alto, CA 94304, USA.
[2] Present address: Griffith University, Brisbane, Queensland, Australia.

in which the methane was statically cooled to 150 K by flowing cold N_2 gas through the outer jacket of the cell.
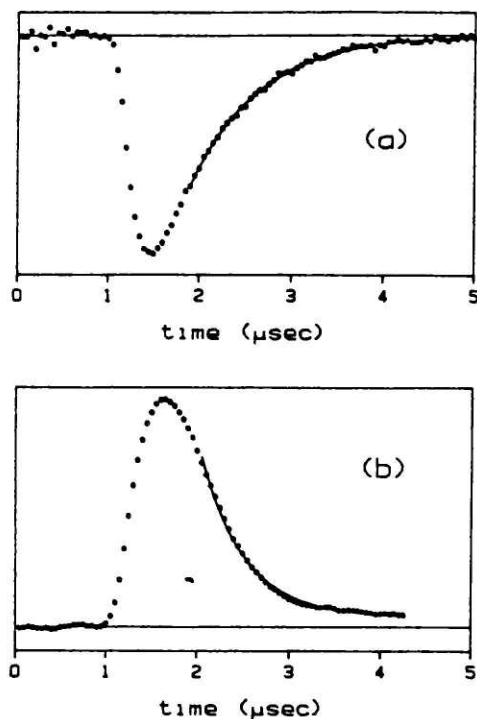
3. Results

The pump frequency used in these experiments was the CO_2 10P(22) laser line at 942.3812 cm^{-1}, which coincides with the P$^+$(12) $F_2^2 - F_1^2$ ($v_4 \leftarrow 0$) transition in $^{13}CD_4$, i.e. F_1^2 of $J = 12$ in the ground vibrational state to F_2^2 of $J = 11$ in the $v_4 = 1$ state. Rotational relaxation in the lower of these levels was monitored on the Q^0(12) line, ($F_2^2, J = 12, v_4 = 1$) ← ($F_1^2, J = 12, v = 0$) at 980.721 cm^{-1}. To monitor relaxation of $J = 11$ ($v_4 = 1$), an excited-state absorption line at 974.607 cm^{-1} was used, tentatively assigned as Q(11) of $2v_4(l = 2) \leftarrow v_4(l = 1)$. A representative example of each of these signals is shown in fig. 1.

Relaxation times were obtained by fitting single exponential decays to the portion of the signal occurring after the termination of the CO_2 laser pump pulse. Measurements were made over a range of pressures between 50 and 500 mTorr. The results are given in table 1 as standard relaxation times $(p\tau)^{-1}$ in units of s^{-1} Torr^{-1} and s^{-1} bar^{-1} (1 bar = 1/1.01325 atm ≈ 750 Torr), and as RET rates in units of cm^3 molecule^{-1} s^{-1}. These data are further reported as effective "relaxation" cross sections, $\sigma_{rot} = k_{rot}/\bar{v}$, with $\bar{v} = (8kT/\pi\mu_{AM})^{1/2}$. While the rates (or relaxation

times) are the quantities actually determined in the experiment, the cross section is useful as a physical measure of the efficiency of the process. Also shown as a basis for comparison are kinetic collision cross sections for each pair, given by $\sigma_{kinetic} = \frac{1}{4}\pi(\sigma_A + \sigma_M)^2 \Omega^{*2,2}(kT/\epsilon_{AM})$ with σ_A and σ_M being the Lennard-Jones hard-sphere diameters of the collision partner and methane, respectively, and $\Omega^{*2,2}$ the collision integral correction [3] determined by ϵ_{AM}, the attractive part of the pair potential.

4. Discussion

The salient features of the data presented in table 1 are:

(i) σ_{rot} increases monotonically with the "size" of the collision partner as measured by collision reduced

Fig. 1. Decay curves of the IRDR signal. The smooth curves are the fitted exponentials. (a) Probe laser on an excited-state absorption. 69 mTorr of $^{13}CD_4$ at 298 K. (b) Probe laser on a ground-state absorption. 155 mTorr of $^{13}CD_4$ at 298 K. The curves are opposite in sign because the pump laser induces a decrease in transmission of the probe beam in (a), and an increase in transmission in (b).

Table 1
Rotational relaxation rates in ground and vibrationally excited levels of $^{13}CD_4$ ($T = 298$ K unless otherwise specified)

Collision partner	$10^{-6} (p\tau)^{-1}$ (s^{-1} Torr^{-1})	$10^{-9} (p\tau)^{-1}$ (s^{-1} bar^{-1})	$10^{10} k_{rot}$ (cm^3 molecule^{-1} s^{-1})	σ_{rot} (Å^2)	$\sigma_{kinetic}$ (Å^2)
vibrational ground state					
$^{13}CD_4$	10.5 ± 0.2	7.88	3.26	41.9 ± 0.8	49.7
He	4.6 ± 0.1	3.5	1.4	10.2 ± 0.2	21.5
Ne	4.7 ± 0.7	3.5	1.5	19.0 ± 2.7	31.6
Ar	5.5 ± 0.3	4.1	1.7	25.0 ± 1.4	44.7
Kr	6.1 ± 0.6	4.6	1.9	31.0 ± 3.0	50.9
Xe	6.4 ± 0.4	4.8	2.0	34.0 ± 2.0	59.0
CH_2F_2	6.5 ± 0.3	4.9	2.0	31.0 ± 1.4	63.1
vibrational excited state					
$^{13}CD_4$	16.6 ± 0.3	12.5	5.17	66.5 ± 1.2	
$^{13}CD_4$ ($T = 150$ K)	25.4 ± 1.4	19.1	3.95	72.0 ± 4	
He	6.5 ± 0.3	4.8	2.0	14.7 ± 0.7	
Ne	7.2 ± 0.6	5.4	2.2	28.0 ± 2.5	
Ar	8.3 ± 0.7	6.2	2.6	38.0 ± 3	
Kr	15.7 ± 0.7	11.8	4.9	79.4 ± 3.4	
Xe	16.2 ± 0.7	12.1	5.0	85.0 ± 3.6	
CH_2F_2	9.9 ± 0.2	7.4	3.1	47.5 ± 0.9	

465

mass μ_{AM} or collision cross section $\sigma_{kinetic}$.

(ii) Self-relaxation proceeds about twice as fast for methane–methane collisions as would be predicted by the preceding correlation; however, a non-identical polar molecule such as CH_2F_2 shows no marked increase in σ_{rot} over the values for monatomic collision partners.

(iii) The relaxation rates are 50–100% *faster* in the $v_4 = 1$ excited state than in the vibrational ground state.

(iv) The temperature dependence of σ_{rot} is weak.

In comparing these results with each other and with measurements of rotational relaxation in methane by other techniques, e.g. ultrasonic absorption [4] ‡, one must be careful to distinguish the averaging over rotational states carried out in each of these different experiments. The double resonance signal $S(t)$ measures the change produced by the pump laser in the population difference between lower and upper levels connected by the probe laser frequency. In the case of relaxation out of $J = 11$ of $v_4 = 1$, this is an excited-state absorption line, so that the upper-level ($v_4 = 2$) population $N_u = 0$ at all times. The time dependence of this signal is then

$$dS(t)/dt = dN_\varrho/dt = N\, dP(J = 11; t)/dt, \qquad (1)$$

where N is the total number density of methane molecules and $P(J,t)$ is the fractional population of level J. We may substitute into eq. (1) the standard rotational master equation [5] ‡‡ to give:

$$dS(t)/dt = N\rho \sum_{J'}[k(J' \to J)P(J') - k(J \to J')P(J)], \qquad (2)$$

where ρ is the number density of collision partners.

In the excited-state probe experiment, only the $J = 11$ level of $v_4 = 1$ is initially populated, and population in any other single rotational level remains small because collisions produce a wide range of final J' states [1]. We may therefore neglect $P(J')$ in eq. (2) for short times, and so obtain:

---

‡ Kistemaker et al. [4] used $^{12}CD_4$, but that should affect rotationally inelastic collision rates only minimally as compared with $^{13}CD_4$.

‡‡ We use the statistical-weight factor $(2J + 1)^2$ in eq. (6) which is appropriate for spherical-top molecules, rather than the factor $2J + 1$ for diatomic molecules discussed in ref. [5].

$$dS(t)/dt \approx dN(J)/dt = -N_0(J)\rho \sum_{J'} k(J \to J'), \qquad (3)$$

which predicts a single exponential decay for $S(t)$ with a relaxation time constant which is simply a sum over final states,

$$\tau = \left(\rho \sum_{J'} k(J \to J')\right)^{-1}. \qquad (4)$$

This is a sum of unaveraged rates which can be compared most directly to the results of inelastic scattering calculations.

In the case of relaxation back into the depleted $J = 12$ level of the vibrational ground state, the other J' levels are all populated, and $P(J)$ is initially $\approx 50\%$ of its thermal equilibrium value when the pump transition is saturated. This leads to a quite different expression for the time dependence of this three-level signal,

$$dS(t)/dt = dN_\varrho/dt - dN_u/dt$$

$$= N\rho \sum_{J'}[k(J' \to J)P(J') - k(J \to J')P(J)]$$

$$- N\rho\, dP(J = 12, v_4 = 1)/dt. \qquad (5)$$

In eq. (5), not only are the k averaged over the equilibrium populations of $J' \neq 12$ levels, but a significant population remains in $J = 12$ and contributes to the overall relaxation time. If the energy transfer rates followed a statistical exponential-gap scaling relationship [5], then reduction of $P(J)$ in eq. (5) to one-half its thermal equilibrium value would lengthen the rotational relaxation time of the depleted level to just twice that found for the vibrationally excited level [eq. (4)]. To be sure, recent work by Pritchard [6] and de Pristo [7] has shown that an angular-momentum-based scaling law is more appropriate for RET than an exponential-gap law; furthermore, our own work on this [1] and other [2] molecules has demonstrated that not all final K or symmetry states are equally accessible in inelastic collisions. Nevertheless, the functional behavior of the various scaling laws is similar [8], and the observed behavior is consistent with the interpretation given above.

We have also retained the $N_u(t)$ term in eq. (5), since this corresponds to $J = 12$ of $v_4 = 1$, which is one of the levels directly populated in the excited-state relaxation process. Population remains in this level after rotational equilibration, since $k_{VT} \ll k_{rot}$, and

466

appears as the long-time "tail" of the signal in fig. 1b.

The more highly averaged relaxation time obtained from analysis of ground-state absorption signals is more nearly comparable with the bulk rotational relaxation time,

$$\tau_{rot}^{-1} = -(E_{rot} - E_{transl})^{-1} \, dE_{rot}/dE. \tag{6}$$

These quantities are still not equivalent, however, because τ_{rot} is averaged over all initial and final states. Nonetheless, it is useful to compare the data in table 1 with that obtained from the bulk measurements. The "rotational collision numbers" Z_{rot}, found by dividing $\sigma_{kinetic}$ by σ_{rot}, are in the range 1.7–2.2 for all the rare-gas collision partners. This is in fortuitous agreement with the value found by Kistemaker et al. [4] for $^{12}CD_4$–He, $Z_{rot} = 2.6 \pm 0.7$. They also found $Z_{rot} = 10$ for CD_4 self-collisions, corresponding to a much smaller effective cross section than we measure. This is easily understood, however, since the principal relaxation channel in methane self-collision will be near-resonant rotation–rotation transfer with the collision partner, and this does not contribute to the ultrasonic measurement. What is more surprising is the trend for the other rare-gas atoms. The ultrasonic results show Z_{rot} increasing with collision reduced mass, up to $Z_{rot} = 14$ for CD_4–Xe, in accordance with the predictions of simple rough-sphere model calculations [9]. Our values, on the other hand, remain nearly constant. The discrepancy may be due to the rotational fine-structure of the inelastic collision cross sections, which are averaged differently in the two sets of measurements. We are carrying out measurements of these detailed state-to-state rate coefficients, using a short-pulse TEA CO_2 laser as the pump source. The results of these experiments will be directly compara-

ble to semiclassical calculations of inelastic scattering cross sections, which are now beginning to appear [10], and will permit us to establish the precise form of the RET scaling law for this molecule.

Acknowledgement

References

[1] L. Laux, B. Foy, D. Harradine and J.I. Steinfeld, J. Chem. Phys. 80 (1984) 3499.

[2] D. Harradine, B. Foy, L. Laux, M. Dubs and J.I. Steinfeld, J. Chem. Phys. 81 (1984) 4267.

[3] J.O. Hirschfelder, C.F. Curtiss and R.B. Bird, Molecular theory of gases and liquids (Wiley, New York, 1954).

[4] P.G. Kistemaker, M.M. Hanna and A.E. de Vries, Physica 78 (1974) 457.

[5] A. Ben-Shaul, Y. Haas, K.L. Kompa and R.D. Levine, Lasers and chemical change (Springer, Berlin, 1981) pp. 150–152.

[6] T.A. Brunner, N. Smith, A.W. Karp and D.E. Pritchard, J. Chem. Phys. 74 (1981) 3524.

[7] A.E. de Pristo, S.D. Augustin, R. Ramaswamy and H. Rabitz, J. Chem. Phys. 70 (1979) 5442.

[8] J.I. Steinfeld and P. Ruttenberg, JILA Information Center Report No. 23, Boulder, CO (December 1983).

[9] B.J. Widom, J. Chem. Phys. 32 (1960) 913;
N.F. Sather and J.S. Dahler, J. Chem. Phys. 35 (1961) 2029. 37 (1962) 1947;
C. O'Neal Jr. and R.S. Brokaw, Phys. Fluids 6 (1963) 1675.

[10] M.Y. Perrin and G. Jolicard, Chem. Phys. 91 (1984) 341.

467

Appendix Three
Grounding and Shielding of the Diode Laser

A serious problem that we encountered when doing double resonance measurements with the CO_2 TEA laser was rf interference in the diode laser circuitry. We discovered that the standard diode laser apparatus produced by Laser Analytics is enormously sensitive to rf pickup from sources such as pulsed-discharge lasers. This problem has been encountered by a wide variety of researchers in the field, and the steps we took to circumvent it may be of interest to others.

Interference by rf pickup causes the diode laser output frequency to undergo oscillatory perturbations. The oscillations are large and long lasting. In our experiment, we observed deviations that were several times greater than the Doppler width of $^{13}CD_4$ (~90 MHz); the equilibration period was 50 μsec or longer. The effect of this perturbation is very similar to that of scattered light from an intense pump laser, when it is allowed to enter the diode laser cold head. Interference by rf can occur either through ground connections to an offending source or purely radiatively. Radiative pickup, of course, can be diminished only by shielding. Although the current controller (LCM) and temperature controller (CTS) are packaged in reasonably well-shielded containers, the control cable connecting these to the laser head is inadequately protected. This is a serious shortcoming, because the precision tuning current passing through the diode circulates through a 22 ft. loop, of which 15 ft. is formed by this unshielded cable.

In attempting to shorten the 7½ ft. control cable in order to reduce the size of the current loop, we discovered that the multi-pin military connectors at either end require special tools to assemble, which were not available to us. Therefore, we simply cut each of the 11 wires in the cable and spliced the ends together to form a new 2½ ft. cable. We fitted shielding (copper braid) around this cable, attaching the shield at both ends. Shielding was likewise placed on the cable connecting the LCM to the CTS and grounded at both ends. In this way, a continuous Faraday cage surrounds the LCM, CTS, cold head, and interconnecting cables. The cold head is grounded by contact with the optical table. These steps reduced the rf-induced modulation of the laser frequency to an acceptable level. We still found, though, that any BNC cables plugged into receptacles on the LCM caused frequency modulation to occur. Hence, we made sure that all BNC connectors were free during data collection. We do not fully understand why this is necessary.

When all these steps were taken, the residual frequency modulation was apparently less than the 90 MHz Doppler width. It is clear, though, that there exists a plethora of grounding and

shielding problems in the diode laser apparatus that need to be rectified. The grounding scheme of the controlling electronics, in particular, is a complex network of separate sub-circuit grounds that is not described in the LCM manual. It is not apparent to the user of the equipment which of the grounds should or should not be connected to earth ground. Also, it is most perplexing that while the Temperature Sensor leads use coaxial cable, the Laser Current leads, which are equally sensitive, are unshielded wires. We can only hope that these problems, as well as the vibration-induced frequency jitter discussed in Chapter 3, will be attended to carefully by the manufacturer. It is certain that this would lead to considerable improvements in the performance of the diode laser.

Appendix Four
Related Publications

1. "State-to-State Rotational Energy Transfer in Methane ($^{13}CD_4$) from Infrared Double Resonance Experiments with a Tunable Diode Laser." B. Foy, J. Hetzler, G. Millot, and J.I. Steinfeld, submitted to *J. Chem. Phys.*

2. "Etude du Spectre d'Absorption du Méthane $^{13}CD_4$ dans la Région de 1000 cm^{-1}. Analyse de la Diade ν_2/ν_4," G. Pierre, G. Millot, A. Valentin, L. Henry, B. Foy, and J.I. Steinfeld, submitted to *Can. J. Phys.* (In French.)

3. "High-Resolution Stimulated Raman Spectroscopy of Methane $^{13}CD_4$ in the Pentad Region," G. Millot, B. Lavorel, R. Chaux, R. Saint-Loup, G. Pierre, H. Berger, J.I. Steinfeld, and B. Foy, *J. Mol. Spec.* **127**, xxx (1988).

4. "Measurement of the Vibrational Dependence of the Coriolis Splitting Parameter in CDF_3 by Infrared Double-Resonance Spectroscopy," Zhao Yao, B.R. Foy, J.R. Hetzler, and J.I. Steinfeld, *Spectrochim. Acta* **42A**, 1337 (1986).

5. "Rotational Energy Transfer Cross Sections in Methane ($^{13}CD_4$) from Infrared Double Resonance Measurements," B. Foy, L. Laux, S. Kable, and J.I. Steinfeld, *Chem. Phys. Lett.* **118**, 464 (1985). (This is included in this thesis as Appendix 2.)

6. "Infrared Double Resonance of Fluoroform-d with a Tunable Diode Laser," D. Harradine, B. Foy, L. Laux, M. Dubs, and J.I. Steinfeld, *J. Chem. Phys.* **81**, 4267 (1984).

7. "Measurement of State-to-State Rotational Energy Transfer in Methane by Infrared Double Resonance," L. Laux, B. Foy, D. Harradine, and J.I. Steinfeld, *J. Chem. Phys.* **80**, 3499 (1984).